

Diploma Thesis

**CFD modeling and Simulation
of
the Airflow around a
Wind Turbine**

Richard Gruber

Institute of Hydraulic Fluidmachinery
Graz University of Technology
Chair: O. Univ.-Prof. Dipl.-Ing. Dr. techn. Helmut Jaberg



Assessor: O. Univ.-Prof. Dipl.-Ing. Dr. techn. Helmut Jaberg
Supervisors: Ass. Prof. Dipl.-Ing. Dr. techn. Helmut Benigni, TU Graz
Dipl.-Ing. Sami Jaber, AMSC Windtec
Dipl.-Ing. Dr. techn. Andreas Tratnig, AMSC Windtec

Graz, January 10, 2011

Deutsche Fassung:
Beschluss der Curricula-Kommission für Bachelor-, Master- und Diplomstudien vom 10.11.2008
Genehmigung des Senates am 1.12.2008

EIDESSTÄTTLICHE ERKLÄRUNG

Ich erkläre an Eides statt, dass ich die vorliegende Arbeit selbstständig verfasst, andere als die angegebenen Quellen/Hilfsmittel nicht benutzt, und die den benutzten Quellen wörtlich und inhaltlich entnommenen Stellen als solche kenntlich gemacht habe.

Graz, am

.....
(Unterschrift)

Englische Fassung:

STATUTORY DECLARATION

I declare that I have authored this thesis independently, that I have not used other than the declared sources / resources, and that I have explicitly marked all material which has been quoted either literally or by content from the used sources.

.....
date

.....
(signature)

Preface

This diploma thesis was written at the Institute of Hydraulic Fluidmachinery, and it is the final project for receiving the "Diplomingenieur" degree in mechanical engineering at the Graz University of Technology. This diploma thesis was provided by the company AMSC Windtec GmbH in Klagenfurt, Austria.

Danksagung

Mein besonderer Dank gilt dem gesamten Team am Institut für Hydraulische Strömungsmaschinen, die mir mit ihrem Wissen und zahlreichen Tipps und Tricks immer zur Seite standen. Insbesondere möchte ich mich bei meinem Betreuer Herrn Benigni Helmut und dessen Kollegen Herrn Schiffer Jürgen bedanken.

Auch möchte ich mich bei der Firma AMSC Windtec für die Durchführung und für die Betreuung dieser Arbeit bedanken.

Bedanken möchte ich mich auch bei all meinen Studienfreunden für zahlreiche Diskussionen, die für das Gelingen dieser Arbeit hilfreich waren. Natürlich gilt dieser Dank auch meinem Arbeitskollegen und Freund, Herrn Mosshammer Markus, der mich bei zahlreichen Rauchpausen rauchfrei begleitete.

All meinen Freunden und Bekannten gebührt großer Respekt für ihre Geduld in Hinblick auf meine spärliche Anwesenheit.

Allen mentalen Unterstützern und Unterstützerinnen, die mich während meines Studiums begleiteten, ein herzliches Dankeschön.

Eine große Umarmung für meine Freundin Verena, die mich immer wieder in die große Welt zurückholte und immer ein offenes Ohr für technische Probleme hatte, auch wenn sie diese nicht verstand.

Und zu guter Letzt bedanke ich mich mit einer extrem großen Umarmung bei meinen Eltern, meinen Geschwistern, meiner Familie, einerseits für die finanzielle Unterstützung, die mir das Studium erst ermöglichte, andererseits für die schönen Stunden, die einen im Kreis der Familie zur Ruhe kommen lassen.

Abstract

This diploma thesis describes a CFD simulation of a wind turbine. The used wind energy converter is the *WT2000* of the company AMSC Windtec. One part of the work was to find a CFD setup in order to get reasonable results, the second part was to interpret and evaluate the results. The steps were, starting with a 3D-CAD geometry file, to develop a model in order to achieve adequate results. Different settings were used to minimize the solver run time and to achieve good convergence. Furthermore, a mesh size study and the interpretation of the influence on the results was realized. Based on the 3D model of the blade, a cross section of the blade was used to get a 2D airfoil. This airfoil was evaluated with regard to the lift, drag, pressure and skin friction coefficient against measurements and other CFD simulations.

Last but not least, a simulation model of the whole wind turbine consisting of 3 blades, a spinner, the nacelle and the tower was developed. The settings were assumed from the 1/3 model.

Kurzfassung

Diese Diplomarbeit beschreibt eine CFD-Simulation einer Windturbine. Der verwendete Windenergiekonverter ist der Typ *WT2000* der Firma AMSC Windtec. Ein Teil dieser Arbeit bestand darin, die entsprechenden CFD Einstellungen zu finden um vernünftige Ergebnisse zu erhalten, der zweite Teil bestand darin, die Ergebnisse zu evaluieren und zu interpretieren. Die Aufgabe war es, ausgehend von einer 3D-CAD Geometrie ein Modell aufzubauen, um passende Ergebnisse zu bekommen. Verschiedene Einstellungen wurden verwendet, um die CFD Solver Laufzeit zu minimieren und ein gutes Konvergenzverhalten zu erzielen. Auch wurde eine Netzstudie durchgeführt, deren Einfluss auf die Ergebnisse interpretiert wurde. Basierend auf einem 3D-Schaufelmodell, wurde ein Schnitt erzeugt um das 2D Profil zu bekommen. Dieses Profil wurde hinsichtlich des Auftriebs-, Widerstands-, Druck- und Wandreibungskoeffizienten evaluiert, und diese Profilkoeffizienten wurden mit Messergebnissen und anderen CFD-Simulationen verglichen.

Zu guter Letzt wurde ein Simulationsmodell der gesamten Windturbine, bestehend aus 3 Flügeln, Rotor, Gondel und Turm, entwickelt. Die Einstellungen dieses Modells wurden vom 1/3-Modell übernommen.

Nomenclature

α	angle of attack	deg
β	local twist angle plus pitch angle	deg
δ	boundary layer thickness	mm
Δy	mesh spacing between wall and first node	mm
ϵ	lift to drag ratio, glide ratio	
η	mechanical efficiency of the wind turbine	
$\eta_{\text{airfoil}(\lambda, \epsilon)}$	losses of the airfoil depends on λ and ϵ	
$\eta_{\text{spin}(\lambda)}$	spin efficiency depends on λ	
$\eta_{\text{tip}(\lambda, B)}$	tip efficiency depends on λ and B	
η_u	circumferential efficiency	
λ	tip speed ratio	
ν	kinematic viscosity	m^2/s
ω	angular velocity	rad/s
ϕ	local flow angle	deg
ρ	density	kg/m^3
τ_w	wall shear	N/m^2
c_d	drag coefficient	
c_f	skin friction coefficient	
c_l	lift coefficient	
$c_{P, \text{Betz}}$	maximal power coefficient (Betz)	
$c_{P, \text{real}}$	real power coefficient	
c_p	pressure coefficient	
F_U	circumferential Force	N
p_∞	pressure at incident flow	Pa
P_{max}	maximum of mechanical power (Betz)	kW
P_{real}	real mechanical power	kW
$T_{x\text{-axis}}$	torque around x-axis of the rotor blade	J
v_1	wind velocity at entrance far away of rotor	m/s
v_r	rated wind velocity	m/s
v_z	wind velocity	m/s
z	height above ground	m
z_{Hub}	hub height	m
a	axial induction factor	
a_w	wind shear	
B	number of blades	
c	absolute velocity (axial velocity)	m/s
c_m	meridional component of absolute velocity (axial velocity)	m/s
c_u	circumferential component of absolute velocity (axial velocity)	m/s
g	gravitational acceleration	m/s^2

H (energy) head m
L lift force N
l_c airfoil chord length m
p pressure Pa
R radius of the Blade m
Re Reynolds number
t partition
u circumferential velocity m/s
w relative velocity = $(u^2+v^2)^{\frac{1}{2}}$ m/s
Y specific shaft work m^2/s^2
y^+ dimensionless wall distance

Contents

1	Introduction	1
2	Modeling of the Geometry	2
2.1	ProE Wildfire	4
2.1.1	Spinner	4
2.1.2	Blade	5
2.2	TurboGrid	6
2.2.1	Point Preparation with Excel	7
2.2.2	Generation of Hub, Shroud and Blade in TurboGrid	8
2.3	ICEM CFD	9
2.3.1	Blade and Spinner	11
2.3.2	Inlet, Outer and Outlet Dimensions	18
3	Preprocessing	19
3.1	Inlet Boundary Condition	21
3.2	Testing certain Solver and Pre-Settings	22
4	Postprocessing	27
4.1	Mechanical Power, Power Coefficient and mechanical Efficiency	27
4.1.1	Equations	27
4.1.2	Results	28
4.1.3	Discussion	32
4.1.3.1	Tip Losses	33
4.1.3.2	Airfoil Losses	36
4.1.3.3	Spin Losses	36
4.2	Mesh size	37
4.2.1	Surrounding Mesh Size Study	37
4.2.1.1	Inlet	38
4.2.1.2	Outer	39
4.2.1.3	Outlet	41
4.2.2	Rotor Mesh Size Study	42
4.3	Airfoil	54
4.3.1	Aerodynamics	54
4.3.1.1	Simplified Blade Design Process	56
4.3.2	WT93 – Blade Description	60
4.3.2.1	Detailed View of Airfoil on 33.275 [m]	62
4.3.3	Interpretation of the Results	68
4.3.3.1	Reduced axial Velocity Method (Rav Method)	68

4.3.3.2	Comparison of the Results for the Airfoil at 33.275 [m] . . .	71
4.3.3.3	Airfoil Losses	83
4.4	Flow Physics	85
5	Total Wind Turbine Model	91
5.1	Grid Construction	91
5.2	Results	94
5.3	Outlook	96
6	Outlook	97
	List of Figures	102
	List of Tables	103
	Appendix	106

1 Introduction

The aim of the present diploma thesis is to simulate the airflow around a wind turbine. Through this work the company will be able to collect enough know-how for a suitable CFD setup. A 3-D steady and turbulent flow calculation was necessary to study the characteristics of flow. The targets of this diploma thesis are:

- Blade modeling using airfoil data and Ansys CFX
- Modeling nacelle, rotor and air region around the turbine
- Solving the model under certain wind scenarios and achieving convergence
- Performing a mesh size study on accuracy and performance
- Evaluating the results with regard to lift, drag, cross flow and separation
- Evaluating the results with regard to cooler and anemometer position

In order to satisfy the customer, based on the CAD geometry of the whole horizontal wind turbine a technique to build up the CFD simulation in ANSYS CFX has been found and the targets have been reached.

The description of the exact workflow was an explicit requirement of the company Windtec.

2 Modeling of the Geometry

The modeled wind turbine of the company AMSC Windtec is the type WT2000df with the rotor blade WT93, TCIII. The power curve is displayed in figure 2.1 and the technical data sheet is listed in table 2.1.

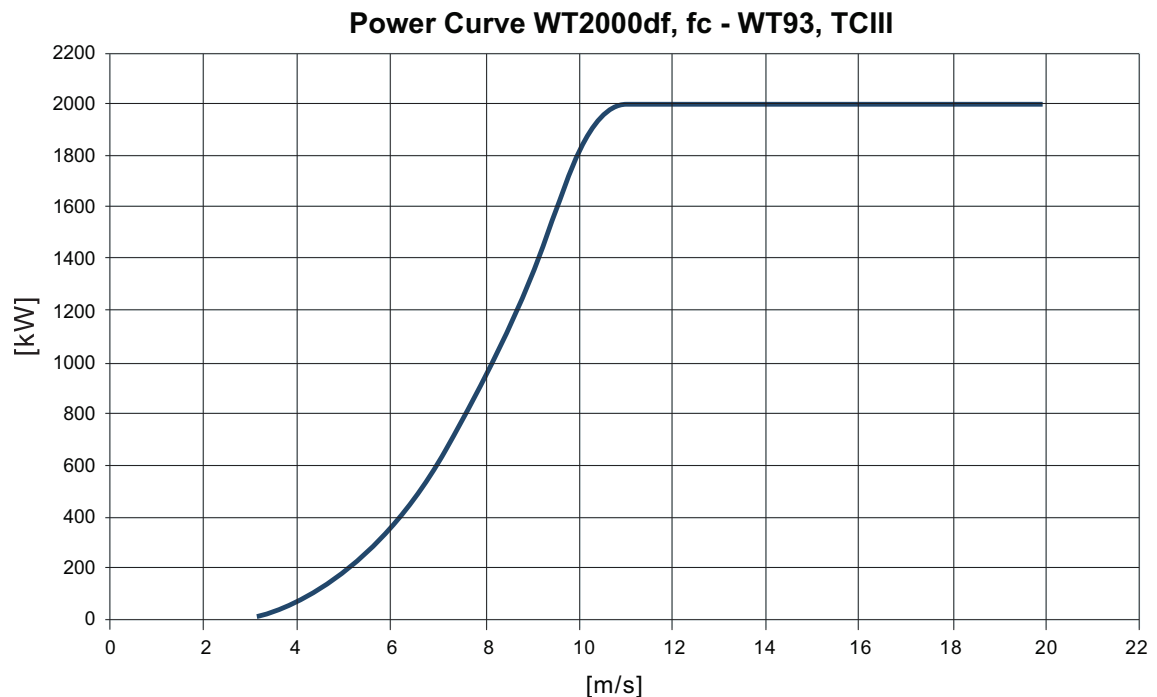


Figure 2.1: Power curve [1]

Based on the geometry file of the whole wind turbine, which was provided to the institute in a geometry interchange format step 214 file, the initial workstep was to excerpt the geometrical information of the geometry. The first idea was, to built the grid in TurboGrid. This special program of ANSYS CFX is a often used program to built structured grids for blades of hydraulic machines such as pumps and turbines. It is a very simple program for turbo machinery designers to create hexahedral meshes. One advantage of this program is the possibility to rotate the blade around a defined axis, i.e. to vary the pitch angle, and the feasibility of the nearly automatic creation of a structured grid.

Table 2.1: Technical data sheet [1]

Technical Data WT2000

	TC III		
	WT2000df		WT2000fc
General	50Hz	60Hz	50 60Hz
Transmission ratio:	114.65	133.5	101.9
Shaft angle in the gearbox:	4.5°		
Hub height:	80m 100m		
Hub type material:	rigid cast iron		
Mainframe type:	cast iron		
Type of tower construction:	conical tubular steel		
Rotor diameter:	93m		
Blade type:	Windtec WT93		
Lightning conductor:	integrated		
Operating data			
Cut-in wind speed:	3.5 m/s		
Rated wind speed:	11.0 m/s		
Cut-out wind speed:	20.0 m/s		
Generator and power electronics			
Generator type:	double fed induction generator		permanent magnet synchronous generator
Rated driving power:	2225 kW		
Rated generator speed:	1800 rpm	2096 rpm	1600 rpm
Poles:	4	6	4
Cooling:	Water jacket		
Converter type:	IGBT, 4 quadrants		IGBT, 4 quadrants - full scale
Power factor:	0.95 ind to 0.95 cap		
Drive train specification			
Type of gearing:	Planetary/parallel shaft gear		
Gear lubrication:	forced lubrication		
Connection gear/generator:	flexible coupling		
Braking system			
Operational brake:	full span blade pitching		
Type of construction:	gear/servomotor		
Mechanical brake:	disc brake		
Yaw system			
Type of yaw bearing:	slide bearing		
Drive unit:	gear motor		
Number of drive units:	4		
Brake:	friction in the slide bearing plus motor brake		

2.1 ProE Wildfire

To continue work, it was necessary to import the file into ProE Wildfire. For a simulation of the airflow around a three-bladed wind turbine without the tower a 1/3-model with periodical interfaces is sufficient. This led to a simplified model with a one hundred and twenty degree segment of the spinner and one blade. For further investigation with Ansys CFX TurboGrid the spinner points and the airfoil points in Cartesian coordinates of the simplified model were needed. One problem was, to export the created points with their space coordinates into a txt-file. The solution was, to save a copy of the file in iges format (with points referenced on a define coordinate system) in ProE Wildfire, then to rename the iges-file as pts-file in Windows Explorer, then to open a new file in ProE Wildfire and to import points with a defined coordinate system (the pts-file). Now, the file was in a correct format which could be saved as txt-file.

2.1.1 Spinner

A simplified model of the spinner (=hub) became necessary, so the geometry was created without the seat of the blade. First, the spinner was intersected by a plane through the rotational axis of the spinner, which led to an intersection curve. On this curve the distribution of points was defined. Now, the Cartesian coordinates belonged to a coordinate system with the x axis on the rotational axis. Figures 2.3 and 2.2 displays how this works. The procedure to export the points for later processing in Excel is explained above.

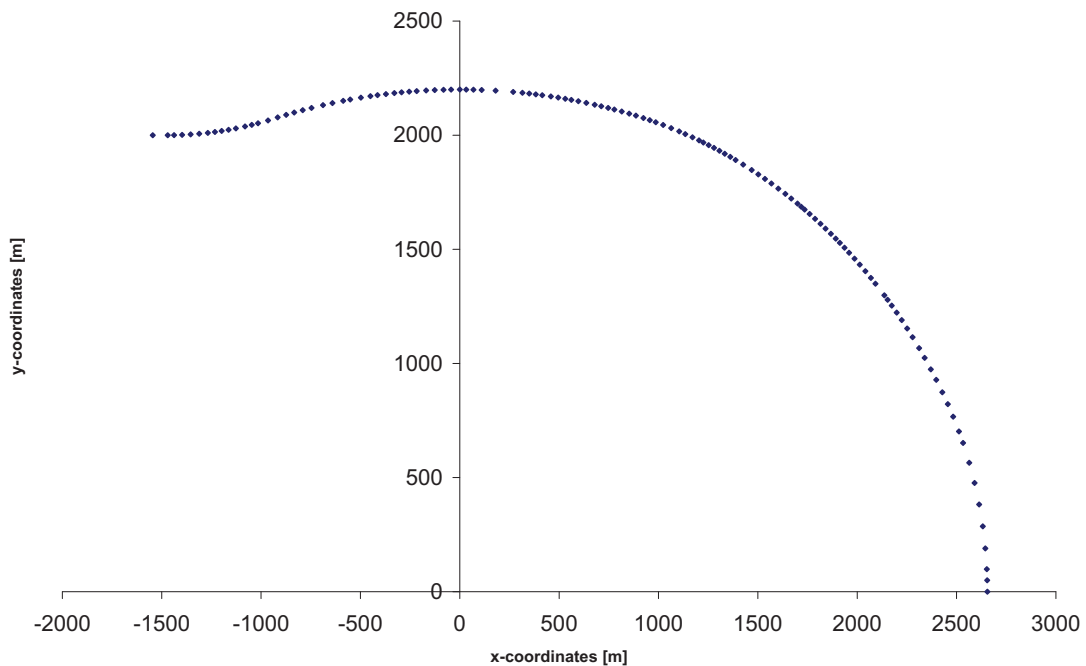


Figure 2.2: The result in Excel for spinner

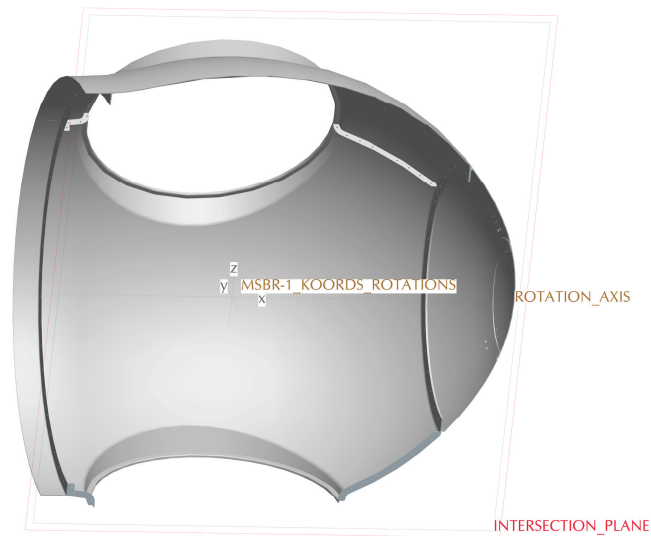


Figure 2.3: Procedure of intersection in ProE WILDFIRE

2.1.2 Blade

To get the airfoils of the WT93 blade, the same technique of creating points on an intersection line was used, see in figure 2.4. The problem was to find out how many points are necessary for an adequate airfoil, and how many airfoils are necessary for an adequate blade. As of the fact that every single point was created by "hand" and then distributed on the curve, a number of approximately one hundred points were created for one profile.

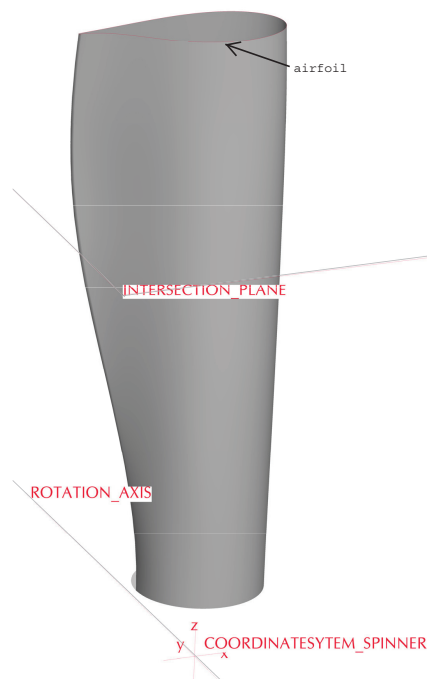


Figure 2.4: Procedure of intersection in ProE WILDFIRE for the blade, the result is displayed in figure 2.7

2.2 TurboGrid

Especially for this model, TurboGrid was very hard to handle in order to generate a reasonable grid around the blade. Also, the huge ratio of hub (spinner) radius to blade radius (shroud), 2.2 meters to 46.5 meters, was very problematic. As it was not possible to import the whole airfoils. By applying the system trial and error, the solution to divide the blade into two parts in order to import the point coordinates in TurboGrid, proved to be the only meaningful way. Another big problem was the distortion of the generated J-grid displayed in figure 2.5.

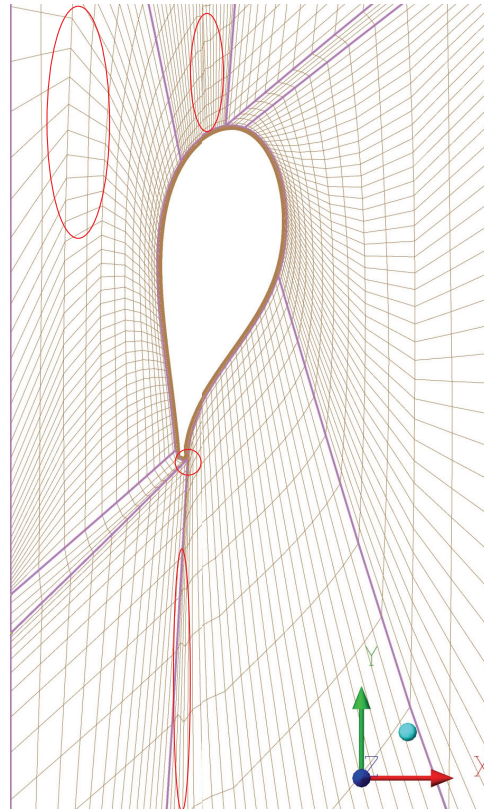


Figure 2.5: The distortion of the J-grid around the airfoil

In order to avoid the distortion of the grid, many points on the layers were based by hand to get better results. Trying to find a solution, the method of rotating the single airfoils in Excel was applied, however with no better result. Additionally, the division of the whole model into 6 parts, to avoid the distortion and the collapse of the grid, was realized, with a slightly better result, however this was not satisfying as in ANSYS CFX Pre every division must be connected with an interface. A variation of the mesh types C, J and H-mesh also did not solve the problem. A few meshes were produced with a pitch angle of -0.8, 0, -2, -4, -6, -8 and -10 degrees, but the rotation with a positive pitch angle led to a collapse of the grid.

A grid type J was built with an O-grid for the concentration in the near wall regions, and 88 elements in spanwise direction. The used O-grid settings were, 5 elements with a size of 0.1 (proportional to width) of the element next to wall. The mesh sizes are listed in table 2.2.

The reason for the above-mentioned problems were the different twist angles between wind turbine blades and turbo machine blades. Generally, turbo machine turbines have guide vanes

Table 2.2: Mesh sizes of the produced -2 degrees model in TurboGrid

	Number of nodes	Number of elements	Number of hexahedras
0-3m	15 444	12 912	12 912
3-6m	15 444	12 912	12 912
6-16m	54 180	48 880	48 880
16-26m	64 764	58 960	58 960
26-36m	75 348	69 040	69 040
36-45m	90 720	83 360	83 360
total	315 900	286 064	286 064

which turn the flow. As a result, the approaching flow direction is different in comparison to turbines without guide vanes and turbines with guide vanes. In TurboGrid it was not possible to define the inflow, the outflow and the periodic boundary condition surfaces. They were provided automatically. The boundary conditions of the wind turbine blade are displayed in figure 2.6. It shows the situation of a wind turbine airfoil with the circumferential component of the velocity being the reason of the rotation of nearly 90 degrees, in contrast to an axial turbine.

The only solution to avoid all the problems mentioned was, to build the grid for blade and spinner in ICEM CFD.

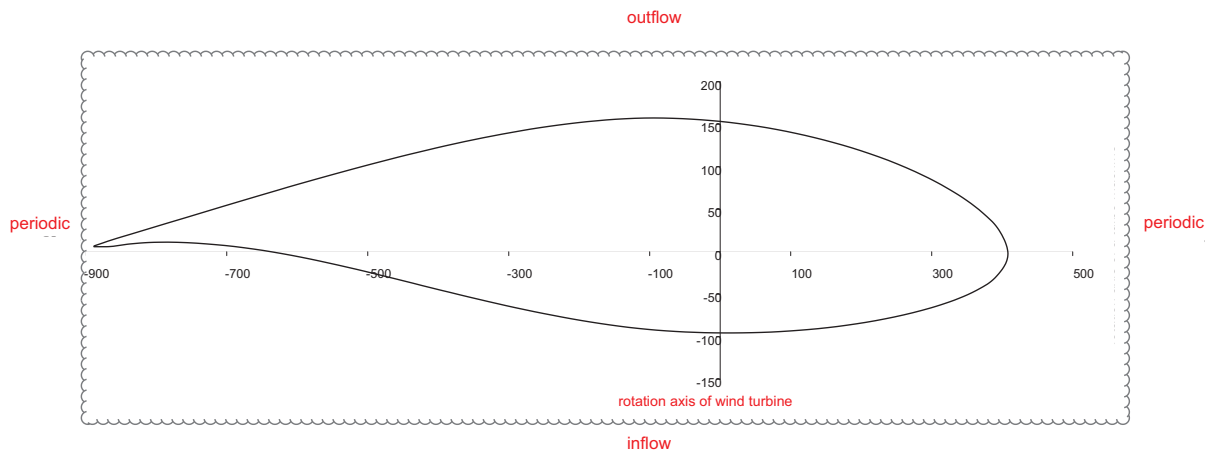


Figure 2.6: The wind turbine boundary condition

2.2.1 Point Preparation with Excel

For the import of the airfoil points into TurboGrid the requirement was to sort all points of each airfoil from one point clockwise or counter clockwise see in figure 2.7. As all points were exported from ProE Wildfire unsorted, it was quite time-consuming to sort them. The reproduction of the blade was created by twenty airfoils, for first investigations.

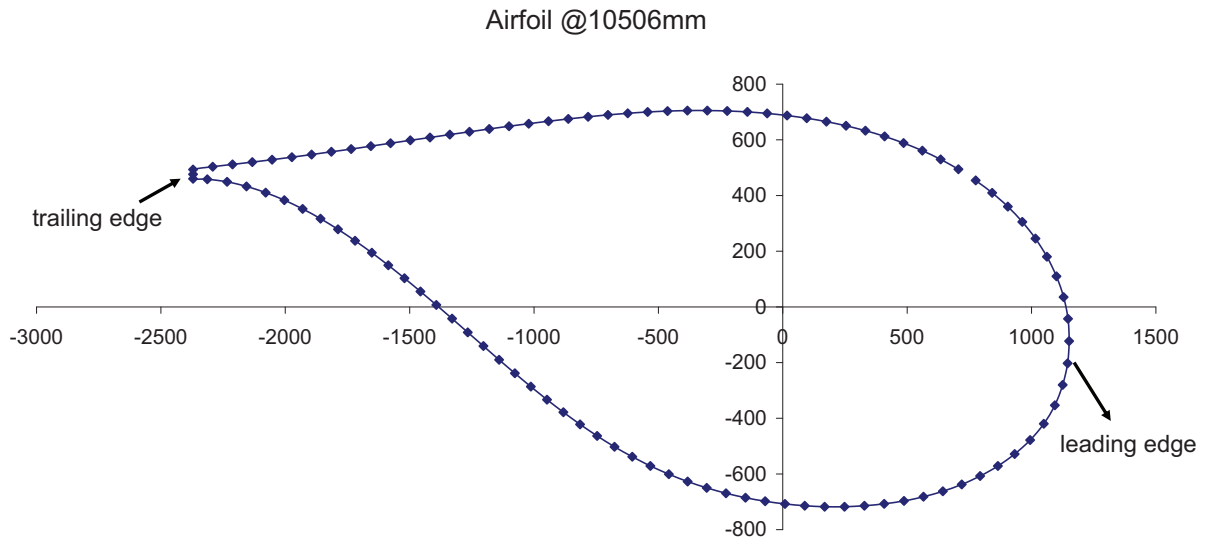


Figure 2.7: Sorted airfoil

2.2.2 Generation of Hub, Shroud and Blade in TurboGrid

In TurboGrid it is possible to import the geometry of a model in space coordinates. *The profile points must be listed line by line, in free-format ASCII style in a closed-loop surrounding the blade. A minimum of two profiles are required in the blade file: one which lies close to the hub surface and one which lies close to the shroud surface. The profile is not required to lie exactly on the surface. If it lies between the hub and shroud surfaces, it must be within 8 percent of the span from the surface. If a profile lies outside of the passage, its distance from the surface has no maximum limit.*

The profiles must be listed in the file in order from hub to shroud. Individual profile datasets are separated by a line beginning with the hash key character. Any text following the hash key character is used as the name associated with the subsequent profile. [2]

The requirements applicable to the import of the hub curve were similar to the requirements applicable to the blade import. *The hub and shroud curve must run upstream to downstream and must extend upstream of the blade leading edge and downstream of the blade trailing edge. The points must be listed in the file line by line, in free format ASCII style, in order from upstream to downstream. [2]*

In the global settings one has to set, the amount of bladesets, in this case three, the rotation axis X and the base unit m. The spinner, called hub by the program was created by means of the imported points, which were connected piece-wise linear, and the surface was created through the rotation of the curve.

Curve type settings have the following options for defining the type of hub or shroud curve.

- *Bspline, the default, means that a smooth curve is interpolated using the points listed in the hub/shroud file. This method may be necessary if the hub or shroud curve is defined with a small number of points. [2]*
- *Piece-wise linear means that the points listed in the hub or shroud file are connected to one another with straight lines. [2]*

The blade was imported with the above mentioned requirements. The points were connected piece-wise linear and the surface in spanwise direction was created bsplined. Then a one hundred and twenty degree model was created.

2.3 ICEM CFD

In ICEM CFD the whole grid of the CFD model was created. For the correct flow simulation not only the modeled rotor, consisting of the hub and the blade, was needed, but also the surrounding area of the wind turbine. For a three-bladed wind turbine the periodicity of the spinner with blade was used. This leads to a one hundred and twenty degree segment of the model. In several papers for the numerical simulation of a wind turbine the size of the surrounding area is given by:

- ten rotor radii upstream and downstream and ten rotor radii in the radial direction [4]
- four rotor radii upstream and sixteen rotor radii downstream and twelve radii in the radial direction [5]

In order to be able to start with the generation of the grid the dimensions displayed in figure 2.8 were chosen. For the grid size study the dimensions of the surrounding area were modified, which will be explained later.

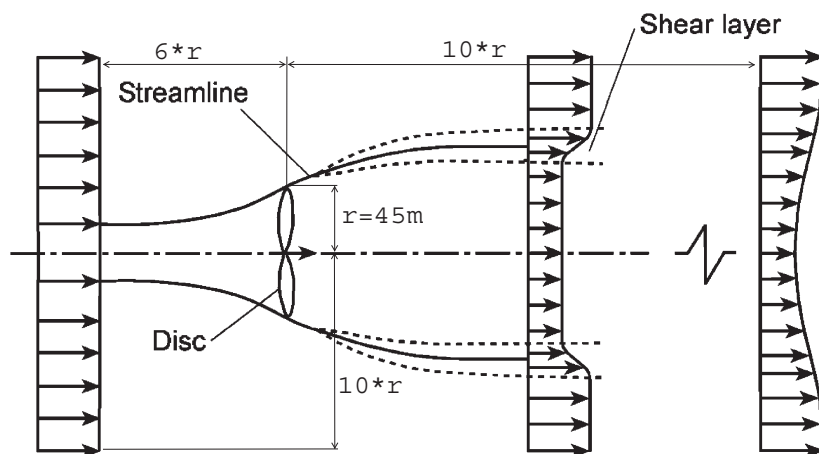


Figure 2.8: The dimensions of the surrounding area and the wind turbine wake (based on paper [6])

The requirement of modeling the surrounding area led to the idea of a block-structured grid of the whole model. This means, that the surrounding area was split into three parts:

- The **inlet** block
- The **outer** block
- The **outlet** block

These blocks wrap the model of the rotor, and the inner dimensions of the three blocks are matched with the outer dimensions of the rotor.

The mesh of the whole model is a structured one, consisting of quads and hexahedrons.

The advantages of a structured grid are the minor demand in working memory and better convergence characteristics.

The advantages of a non structured grid are the nearly automatic building of the grid and the relatively simple mesh generation of complex geometries.

In the present case of modeling a wind turbine with a huge surrounding area, a compromise solution had to be chosen. To represent the real conditions, every model has a "quality minor than reality", as the resolution of the grid which represents the "area of flow" is limited by computer costs and resources. A possible weighting was to decide about the importance of single domains as listed in table 2.3

	flow	results	grid resolution
inlet	wind	interaction	coarse
rotor	wind, rotation, coriolis force	turbulence, tip vortex, wake	fine
outlet	wind, rotation, coriolis force	interactions, turbulence, wake	fine to coarse
outer	wind, rotation, coriolis force	interactions, tip vortex	fine to coarse

Table 2.3: Importance, reaction and mesh weighting

The mesh is constructed for a specific purpose: to solve a given problem. Therefore, the true quality or optimality problem is related to the solution that can be computed with the mesh as a support. In this respect, it makes sense to claim that the mesh quality is good if the resulting solution quality is good. As a consequence and following the same approach, optimality is obtained if the mesh size is minimal, resulting in a minimal cost when computing the problem solution.....

A nice mesh is one which leads to the best possible numerical accuracy, i.e., to a minimal bound for the approximation error.[7]

As a result, grid size was saved in the outlet, inlet and outer domain, and in the rotor domain the resolution of the grid was fine. With regard to a reasonable resolution of the boundary layer, depending on the Reynolds Number which varies in spanwise direction, different grid resolutions were produced. The mesh size of the rotor domain with the number of elements is shown in table 2.4. The boundary layer resolution of the blade is coarse for grid 1, 2, 3 and 4 displayed in table 2.7 and 2.8, the resolution of the first cells starting with the hub in spanwise direction is coarse too, and the finer resolution of the tip is not given. For first investigations the grids 1, 2, 3 and 4 were used, for example, to get the power curves over different pitch angles. For deeper investigations grids 5, 6, and 7 were used, which contain a well-resolved boundary layer and a finer resolution of the first cells from hub to shroud.

In order to reach reasonable results, more detailed meshes were needed and this was realized in subsection 4.2.2.

The mesh quality criteria checked were **quality**, **min angle** and **orientation**.

Table 2.4: Table of sizes of the different meshes (rotor domain)

mesh	mesh size	nodes	quads	hexahedras
	number of nodes			
1	54 000	54 336	10 912	48 786
2	310 000	312 488	37 202	293 712
3	1 100 000	1 138 050	88 414	1 093 574
4	2 700 000	2 688 480	158 032	2 609 104
5	3 400 000	3 371 140	247 921	3 246 635
6	5 500 000	5 535 776	246 457	5 410 456
7	6 900 000	6 933 536	258 937	6 801 976

2.3.1 Blade and Spinner

The points of the spinner and the single airfoils were imported from ProE Wildfire as an iges format file. The creation of the hub surface was no problem, but, the blade surface was difficult to create. First, the single points of each airfoil were connected by a line. Then, each airfoil, from airfoil to airfoil and from hub to shroud, was connected by a line, starting from the points which border trailing edge, suction side, leading edge, and pressure side, in order to create the surfaces of the leading edge, the trailing edge, the suction side and the pressure side. The points around the airfoil were connected, by means of a spline and in spanwise direction by means of piece-wise linear.

The next step was, to create the inflow, the outflow, the shroud and the periodic contour together with their surfaces. The outer contour points for different grid sizes are listed in table 2.5 and, for explanation purposes, the points are displayed in figure 2.11. By creating the shroud at radii of nearly forty-five meters, the realization of the tip vortex was not provided. As a consequence, the radii were enlarged to fifty-five meters. See in table 2.5 for grids 5, 6 and 7. The method is applied in [3] in chapter CFX Best Practices Guide for Turbomachinery.

Table 2.5: Table of different meshes with their contour points

mesh	mesh size	[x/y/z] point 1	[x/y/z] point 2	[x/y/z] point 3	[x/y/z] point 4	[x/y/z] point 5	[x/y/z] point 6
	~ number of nodes	m	m	m	m	m	m
1	54 000	2.564/0/0.565	-1.545/0/2	4.5/0/45.448	-4.5/0/45.448	-	-
2	310 000	2.564/0/0.565	-1.545/0/2	4.5/0/45.448	-4.5/0/45.448	-	-
3	1 100 000	2.564/0/0.565	-1.545/0/2	4.5/0/45.448	-4.5/0/45.448	-	-
4	2 700 000	2.564/0/0.565	-1.545/0/2	4.5/0/45.448	-4.5/0/45.448	-	-
5	3 400 000	2.564/0/0.565	-1.545/0/2	4.5/0/45.448	-4.5/0/45.448	5.18/0/55.448	-4.931/0/55.448
6	5 500 000	2.564/0/0.565	-1.545/0/2	4.5/0/45.448	-4.5/0/45.448	5.18/0/55.448	-4.931/0/55.448
7	6 900 000	2.564/0/0.565	-1.545/0/2	4.5/0/45.448	-4.5/0/45.448	5.18/0/55.448	-4.931/0/55.448

The geometry of the model was now prepared to build the block structure for the generation of the C-grid mesh. Around the blade the block was split into an O-grid block, see in figure 2.9. In spanwise direction the block was split into five to seven blocks, to consider the transition of the different airfoils shown in figure 2.10.

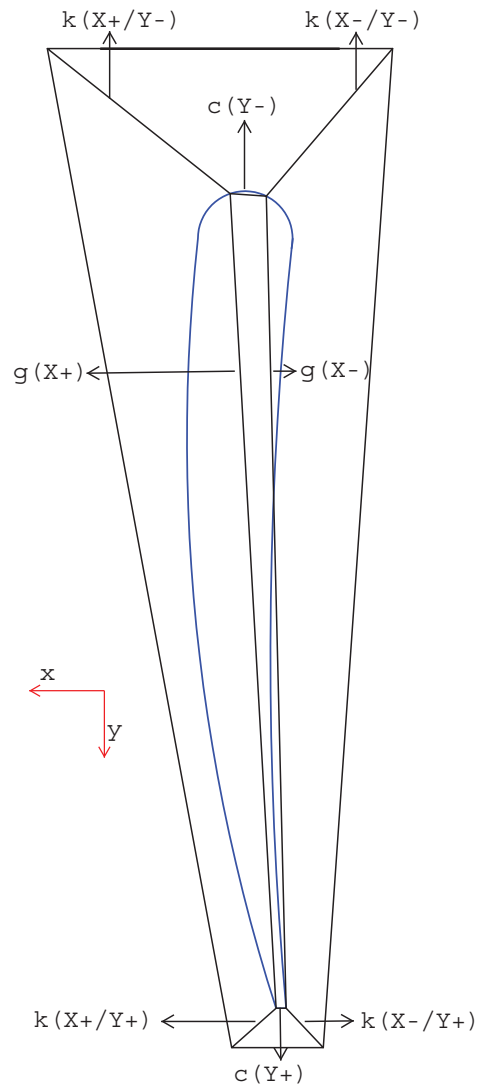


Figure 2.9: A larger scale sketch of the O-grid structure around the airfoil and edge declaration

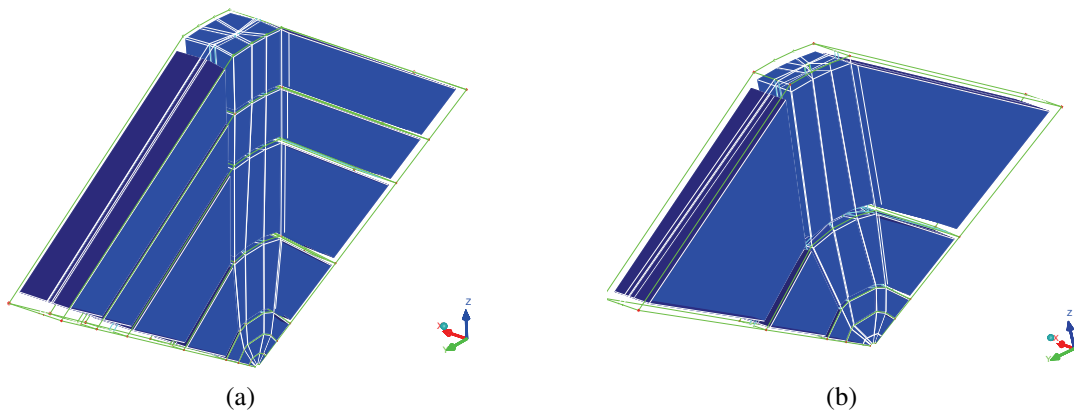


Figure 2.10: 3D-view of the block structure in spanwise direction (a) with realization (b) without realization of the tip vortex in the rotational domain

The transition of the different airfoils start from a circle at the root with a diameter of approximately two meters, and leads to an oval profile at a distance of approximately two meters from the root with a chord length of two meters, and to an airfoil at a distance of approximately eight meters from the root with a chord length of 3.5 meters. The division of the block in spanwise direction is displayed in figure 2.11.

The method of rotating the blade to vary the pitch angle was realized by rotating the blade geometry and then correcting the single edges and vertices of the blocks around the airfoil. For the present diploma thesis, many meshes with different grid sizes and with different pitch angles were generated, see in table 2.6.

Table 2.6: Table of the grid matrix (rotor domain)

		1	2	3	4	5	6	7
		54 000	310 000	1 100 000	2 700 000	3 400 000	5 500 000	6 900 000
nodes	-	54 336	312 488	1 138 050	2 688 480	3 371 140	5 535 776	6 933 536
quads	-	10 912	37 202	88 414	158 032	247 921	246 457	258 937
hexas	-	48 786	293 712	1 093 574	2 609 104	3 246 635	5 410 456	6 801 976
pitch angle	4.5	x	x	x	x			
pitch angle	3.51	x	x	x	x			
pitch angle	3	x	x	x	x			
pitch angle	1.5	x	x	x	x			
pitch angle	0.9	x	x	x	x			
pitch angle	0	x	x	x	x			
pitch angle	-0.8	x	x	x	x	x	x	x
pitch angle	-1.5	x	x	x	x			
pitch angle	-3	x	x	x				
pitch angle	-4.5	x	x	x				
pitch angle	-6	x	x	x				
pitch angle	-7.5	x	x	x				

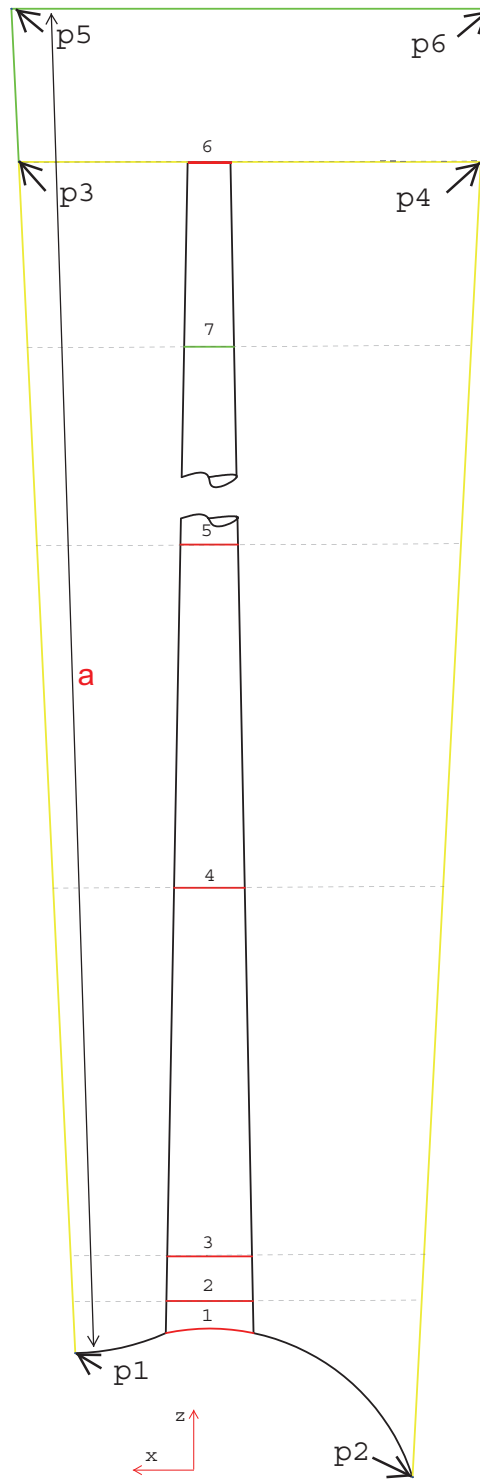


Figure 2.11: Sketch of the block structure with outer contour points and with dash lines which show the divisions of the block and edge declaration

For an explanation of the declaration of the single edges figures 2.9 , 2.11 and 2.12 are presented, in tables 2.7 and 2.8 the edge information is listed for different meshes.

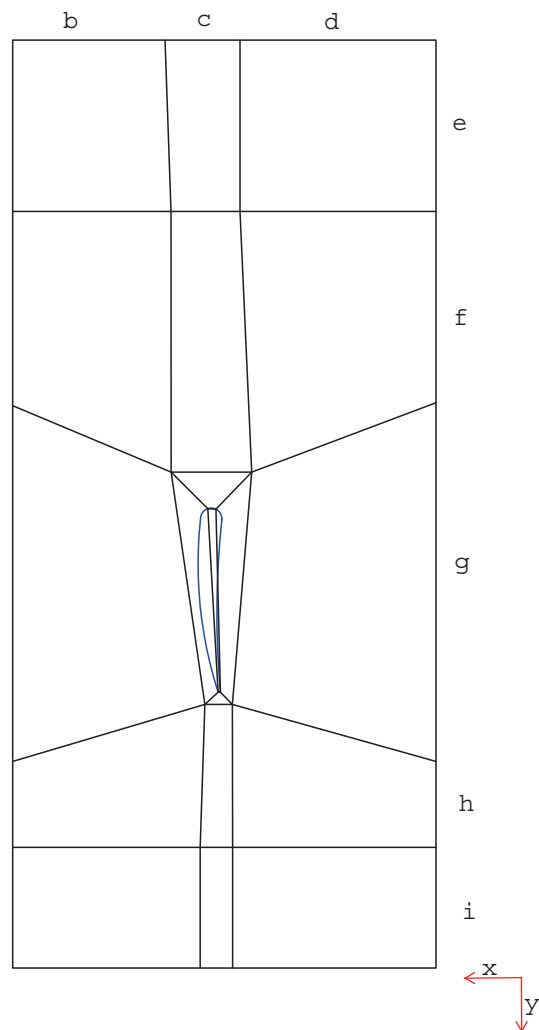


Figure 2.12: Sketch of the O-grid block structure around the airfoil with edge declaration

Table 2.7: Edge information for mesh 1 and mesh 2 with -0.8° pitch angle

	54 000				310 000			
	nodes on edge	edge length	mesh law	element size	nodes on edge	edge length	mesh law	element size
	[#]	[mm]		[mm]	[#]	[mm]		[mm]
a	52	43548	linear	837.46	92	43548	linear	473.35
b	10	4000	linear	400.00	17	4000	linear	235.29
c	3	1000	linear	333.33	8	1000	linear	125.00
d	6	4000	linear	666.67	10	4000	linear	400.00
e	6	42019	linear	7003.17	10	42019	linear	4201.90
f	16	3646	linear	227.88	30	3646	linear	121.53
g	18	3375	linear	187.50	33	3375	linear	102.27
h	16	4115	linear	257.19	30	4115	linear	137.17
i	6	42019	linear	7003.17	10	42019	linear	4201.90
around airfoil 6								
k (X-/Y-)	4	134	linear	33.50	5	134	linear	26.80
k (X+/Y-)	4	177	linear	44.25	5	177	linear	35.40
k (X+/Y+)	4	30	linear	7.50	5	30	linear	6.00
k (X-/Y+)	4	50	linear	12.50	5	50	linear	10.00
c (Y-)	3	16	linear	5.33	8	16	linear	2.00
g (X+)	18	827	linear	45.94	33	827	linear	25.06
c (Y+)	3	4.5	linear	1.50	4	4.5	linear	1.13
g (X-)	18	816	linear	45.33	33	816	linear	24.73
around airfoil 5								
k (X-/Y-)	4	187	linear	46.75	5	187	linear	37.40
k (X+/Y-)	4	284	linear	71.00	5	284	linear	56.80
k (X+/Y+)	4	322	linear	80.50	5	322	linear	64.40
k (X-/Y+)	4	449	linear	112.25	5	449	linear	89.80
c (Y-)	3	95	linear	31.67	8	95	linear	11.88
g (X+)	18	2267	linear	125.94	33	2267	linear	68.70
c (Y+)	3	14	linear	4.67	4	14	linear	3.50
g (X-)	18	2291	linear	127.28	33	2291	linear	69.42
around airfoil 4								
k (X-/Y-)	4	595	linear	148.75	5	595	linear	119.00
k (X+/Y-)	4	730	linear	182.50	5	730	linear	146.00
k (X+/Y+)	4	339	linear	84.75	5	339	linear	67.80
k (X-/Y+)	4	356.3	linear	89.08	5	356.3	linear	71.26
c (Y-)	3	396	linear	132.00	8	396	linear	49.50
g (X+)	18	3537	linear	196.50	33	3537	linear	107.18
c (Y+)	3	71.4	linear	23.80	4	71.4	linear	17.85
g (X-)	18	3555	linear	197.50	33	3555	linear	107.73
around airfoil 3								
k (X-/Y-)	4	755	linear	188.75	5	755	linear	151.00
k (X+/Y-)	4	525	linear	131.25	5	525	linear	105.00
k (X+/Y+)	4	392	linear	98.00	5	392	linear	78.40
k (X-/Y+)	4	557	linear	139.25	5	557	linear	111.40
c (Y-)	3	628	linear	209.33	8	628	linear	78.50
g (X+)	18	2865	linear	159.17	33	2865	linear	86.82
c (Y+)	3	312	linear	104.00	4	312	linear	78.00
g (X-)	18	2871	linear	159.50	33	2871	linear	87.00
around airfoil 2								
k (X-/Y-)	4	723	linear	180.75	5	723	linear	144.60
k (X+/Y-)	4	804	linear	201.00	5	804	linear	160.80
k (X+/Y+)	4	426	linear	106.50	5	426	linear	85.20
k (X-/Y+)	4	589	linear	147.25	5	589	linear	117.80
c (Y-)	3	701	linear	233.67	8	701	linear	87.63
g (X+)	18	2450	linear	136.11	33	2450	linear	74.24
c (Y+)	3	770	linear	256.67	4	770	linear	192.50
g (X-)	18	2229	linear	123.83	33	2229	linear	67.55
around airfoil 1								
k (X-/Y-)	4	467	linear	116.75	5	467	linear	93.40
k (X+/Y-)	4	390	linear	97.50	5	390	linear	78.00
k (X+/Y+)	4	245	linear	61.25	5	245	linear	49.00
k (X-/Y+)	4	384	linear	96.00	5	384	linear	76.80
c (Y-)	3	1015	linear	338.33	8	1015	linear	126.88
g (X+)	18	2010	linear	111.67	33	2010	linear	60.91
c (Y+)	3	1057	linear	352.33	4	1057	linear	264.25
g (X-)	18	1969	linear	109.39	33	1969	linear	59.67

Table 2.8: Edge information for mesh 3 and mesh 4 with -0.8° pitch angle

	1 100 000				2 700 000			
	nodes on edge [#]	edge length [mm]	mesh law	element size [mm]	nodes on edge [#]	edge length [mm]	mesh law	element size [mm]
a	138	43548	linear	315.57	104	43548	linear	418.73
b	26	4000	linear	153.85	20	4000	linear	200.00
c	12	1000	linear	83.33	16	1000	linear	62.50
d	15	4000	linear	266.67	20	4000	linear	200.00
e	15	42019	linear	2801.27	20	42019	linear	2100.95
f	45	3646	linear	81.02	60	3646	linear	60.77
g	50	3375	linear	67.50	66	3375	linear	51.14
h	45	4115	linear	91.44	60	4115	linear	68.58
i	15	42019	linear	2801.27	20	42019	linear	2100.95
around airfoil 6								
k (X-/Y-)	8	134	linear	16.75	10	134	linear	13.40
k (X+/Y-)	8	177	linear	22.13	10	177	linear	17.70
k (X+/Y+)	8	30	linear	3.75	10	30	linear	3.00
k (X-/Y+)	8	50	linear	6.25	10	50	linear	5.00
c (Y-)	8	16	linear	2.00	16	16	linear	1.00
g (X+)	50	827	linear	16.54	66	827	linear	12.53
c (Y+)	6	4.5	linear	0.75	8	4.5	linear	0.56
g (X-)	50	816	linear	16.32	66	816	linear	12.36
around airfoil 5								
k (X-/Y-)	8	187	linear	23.38	10	187	linear	18.70
k (X+/Y-)	8	284	linear	35.50	10	284	linear	28.40
k (X+/Y+)	8	322	linear	40.25	10	322	linear	32.20
k (X-/Y+)	8	449	linear	56.13	10	449	linear	44.90
c (Y-)	8	95	linear	11.88	16	95	linear	5.94
g (X+)	50	2267	linear	45.34	66	2267	linear	34.35
c (Y+)	6	14	linear	2.33	8	14	linear	1.75
g (X-)	50	2291	linear	45.82	66	2291	linear	34.71
around airfoil 4								
k (X-/Y-)	8	595	linear	74.38	10	595	linear	59.50
k (X+/Y-)	8	730	linear	91.25	10	730	linear	73.00
k (X+/Y+)	8	339	linear	42.38	10	339	linear	33.90
k (X-/Y+)	8	356.3	linear	44.54	10	356.3	linear	35.63
c (Y-)	8	396	linear	49.50	16	396	linear	24.75
g (X+)	50	3537	linear	70.74	66	3537	linear	53.59
c (Y+)	6	71.4	linear	11.90	8	71.4	linear	8.93
g (X-)	50	3555	linear	71.10	66	3555	linear	53.86
around airfoil 3								
k (X-/Y-)	8	755	linear	94.38	10	755	linear	75.50
k (X+/Y-)	8	525	linear	65.63	10	525	linear	52.50
k (X+/Y+)	8	392	linear	49.00	10	392	linear	39.20
k (X-/Y+)	8	557	linear	69.63	10	557	linear	55.70
c (Y-)	8	628	linear	78.50	16	628	linear	39.25
g (X+)	50	2865	linear	57.30	66	2865	linear	43.41
c (Y+)	6	312	linear	52.00	8	312	linear	39.00
g (X-)	50	2871	linear	57.42	66	2871	linear	43.50
around airfoil 2								
k (X-/Y-)	8	723	linear	90.38	10	723	linear	72.30
k (X+/Y-)	8	804	linear	100.50	10	804	linear	80.40
k (X+/Y+)	8	426	linear	53.25	10	426	linear	42.60
k (X-/Y+)	8	589	linear	73.63	10	589	linear	58.90
c (Y-)	8	701	linear	87.63	16	701	linear	43.81
g (X+)	50	2450	linear	49.00	66	2450	linear	37.12
c (Y+)	6	770	linear	128.33	8	770	linear	96.25
g (X-)	50	2229	linear	44.58	66	2229	linear	33.77
around airfoil 1								
k (X-/Y-)	8	467	linear	58.38	10	467	linear	46.70
k (X+/Y-)	8	390	linear	48.75	10	390	linear	39.00
k (X+/Y+)	8	245	linear	30.63	10	245	linear	24.50
k (X-/Y+)	8	384	linear	48.00	10	384	linear	38.40
c (Y-)	8	1015	linear	126.88	16	1015	linear	63.44
g (X+)	50	2010	linear	40.20	66	2010	linear	30.45
c (Y+)	6	1057	linear	176.17	8	1057	linear	132.13
g (X-)	50	1969	linear	39.38	66	1969	linear	29.83

2.3.2 Inlet, Outer and Outlet Dimensions

The inlet, outlet and outer dimensions are summarized in table 2.9, all referring to 120 degree cylinders.

Table 2.9: Geometrical inlet, outlet and outer dimensions

	inlet	outlet	outer
	[L x R _a]	[L x R _a]	[R _a]
1	6 · R x 10 · R	10 · R x 10 · R	10 · R

The mesh sizes created are listed in table 2.10. A detail of the surrounding area mesh is represented in figure 2.13.

Table 2.10: The size of the mesh used for the surrounding area

mesh	nodes	quads	hexas
inlet	979 047	60 512	948 480
outlet	851 445	58 240	822 016
outer	315 000	30 406	299 574

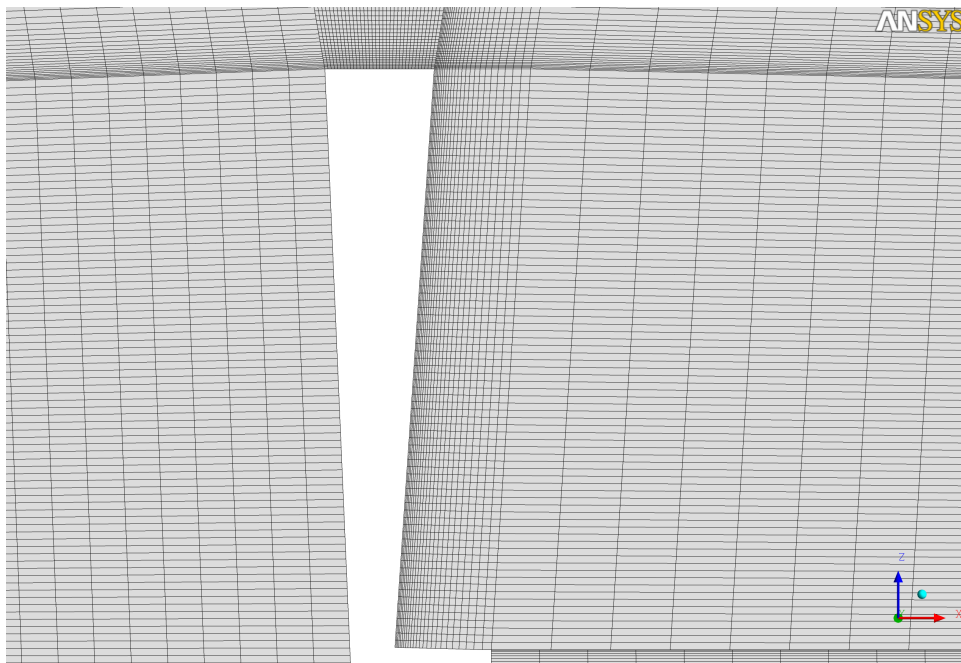


Figure 2.13: Detail of the surrounding mesh

3 Preprocessing

The program package used was Ansys CFX 11.0. CFX-Pre is the program apt for preprocessing. The first step was to load the meshes built in ICEM CFD. Every mesh was referenced on a global coordinate system, in order to prevent mesh overlapping and to avoid mistakes. Each single mesh was checked, to whether installation situation was correct.

All surfaces created in ICEM CFD needed an assignment of the boundary conditions, and between the single domains the surfaces were assigned by means of domain interfaces. The domains are displayed in figure 3.1, and the related boundary conditions are listed in table 3.1.

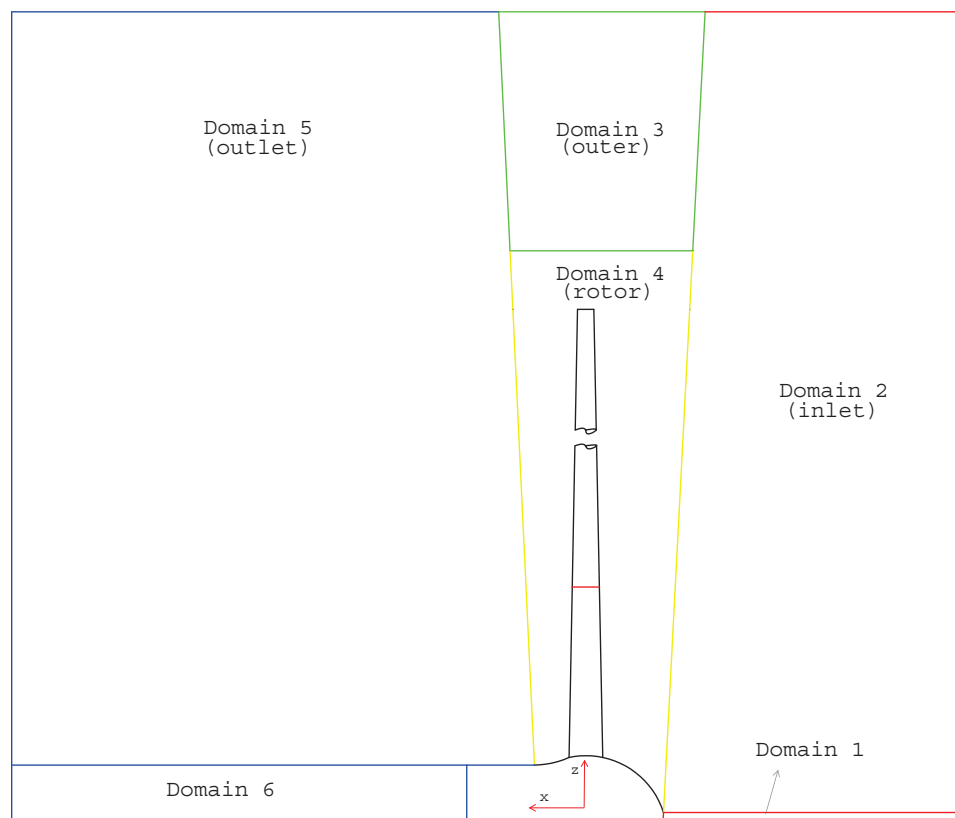


Figure 3.1: Sketch of the domains with denotation

The only rotated domain with the circumferential velocity of the particular operating point was domain 4, all other domains were stationary. For flows in a rotating domain the additional sources of momentum are added to account for the effects of the Coriolis force and the centrifugal force.

The selected turbulence model was the **Shear Stress Transport** model. The paper "A comparative numerical study of four turbulence models for the prediction of HAWT flow" ([8]) compares four different models: the Spalart-Allmaras, the k-epsilon, the k-epsilon renormal-

Table 3.1: Domain matrix of boundary conditions and interfaces

Domain	1	2	3	4	5	6
1	p,n.w,v in	n				
2	n	p,f.w,v in	n	fr		
3		n	p,f.w	fr	n	
4		fr	fr	p,n.w,n.w	fr	
5			n	fr	p,f.w,p out,n.w	n
6					n	p,n.w,p out

p= rotational **periodicity**
n.w= no slip **wall**
f.w= free slip **wall**
v in= **inlet** normal speed
fr= frozen rotor (**frame change**)
n= none (**frame change**)
p out= **outlet** static pressure

ization group and the k-omega SST. From the conducted study, it is confirmed that it is possible to analyze a HAWT rotor flow field with the RANS equations and that there is good agreement between the computations and the experimental data when the k-omega SST model is used. [8] The simulated operating points are listed in table 3.2. The selected advection scheme was high resolution. Different pre-files were generated to find the correct setting for the time scale control.

In order to get a better feeling for the convergence behavior, a monitor point was created which shows the power over the time steps.

Table 3.2: Operating points, (*averaged value)

op	wind speed	rotational speed	pitch angle
	[m/s]	[rpm]	[deg]
1	4.00	8.11	0.9
2	6.00	10.74	0
3	9.75	15.70	-0.8
4	12.25	15.70	3.51*

3.1 Inlet Boundary Condition

The wind is used by wind turbines is not of a constant size. The flow of the wind over the rough earth leads to an earth boundary layer, as the flow is slowed down by the ground. The boundary layer thickness, depends on the roughness and varies between ten and hundreds of meters. Figure 3.2 (a) shows a sketch of the earth boundary layer. This means that wind turbines always operate in the earth boundary layer. Equation for the wind velocity is an empirical one:

$$v_z = v_r \cdot \left(\frac{z}{z_{\text{Hub}}} \right)^a \quad (3.1)$$

The results of this equation are displayed in figure 3.2 (b).

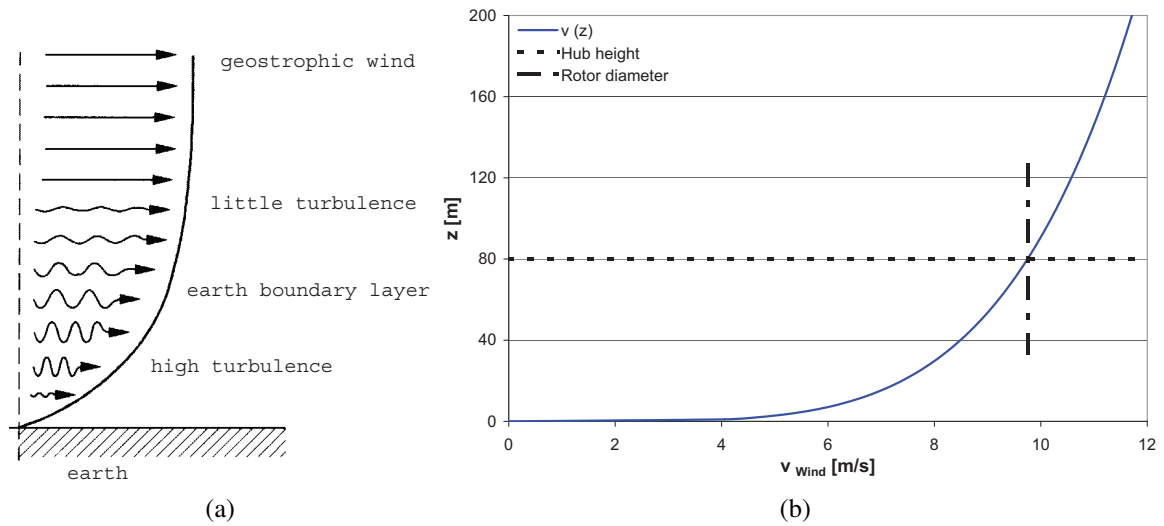


Figure 3.2: (a) Sketch of the earth boundary layer (based on [12]), (b) chart of the results of equation 3.1 with $a = 0.2$, $v_r = 9.75$ [m/s] and $z_{\text{Hub}} = 80$ [m]; additionally a sketch of the rotor is presented

As a result of the above behavior of the wind velocity, the boundary condition **v in** was not constant.

Last but not least, at the end of the work on my diploma thesis, a short discussion with work-mates led to the result that the wind boundary layer as boundary condition is not correct for the simulated model. As a 1/3 model had been simulated, the result i.e. the power output was multiplied by 3. However as displayed in figure 3.2, the inlet wind velocity in 40 meters height is lower than in 120 meters height. The hub height is in 80 meters which is the coordinate of the rotation axis, and the blade tip coordinates are in heights of 40 meters and 120 meters.

For a correct simulation with the wind boundary layer a simulation of the full circle model with 3 blades is the only correct solution.

3.2 Testing certain Solver and Pre-Settings

A solution to improve the convergence behavior can be, to use double precision instead of single precision in order to avoid rounding errors. Different settings are possible, which more or less lead to a better or a worse convergence behavior, for example the time scale. In order to interpret the convergence behavior, the installation of a monitor point, which presenting a physical variable, which important to the simulation, is recommended. In this case, the mechanical power was plotted.

The use of the alternate rotation model can significantly reduce numerical errors when the absolute frame flow is essentially a constant flow parallel to the axis of rotation. In the case of a wind turbine, the approach flow is nearly constant in the absolute frame but highly rotating in the relative frame. *At very large radii, small errors in the advection model of the relative frame flow become large errors in the computed flow in the absolute frame. When the alternate rotation model is used in this situation, the numerical error can be greatly reduced, because the absolute frame velocity is close to constant.*[9]

The residuum is an integral measure of the difference for the flow variables between two time steps. A simulation is converged if the residuals are constant and the residual target aimed at is reached (i.e. $1 \cdot 10^{-4}$). In the Navier-Stokes procedures like the RANS equations little oscillations are always remaining.[10]

The time scales used by the CFX Solver are as follows [9]:

- Auto Timescale
- Physical Timescale
- Local Timescale Factor

Auto Timescale control uses an internally calculated physical timescale based on the model settings. It is a conservative timescale, which leads to a long computational time to converge in this simulation. However a constant power is reached. The residuals and the power curve are displayed in figure 3.3.

Another method is to calculate the physical timescale on one's own. In this case, it was calculated by means of the formula:

$$t = \frac{1}{\omega \cdot B} \quad (3.2)$$

As shown in figure 3.4, the simulation requires a long period of time to reach low residuals, and the power curve over the timesteps is not constant.

The Local Timescale Factor option allows different time scales to be used in different regions of the model. The value you enter is a multiplier of a local element-based time scale. Smaller time scales are applied to regions of the flow where the local time scale is very short (such as fast flow), and larger time scales to those regions where the time scale is locally large (such

as slow flow). This option is very useful when there are widely varying velocity scales in the simulation [9], like in this simulation case, where the absolute velocity in the stationary domains has a value of around 10 m/s in comparison to the relative velocity in the rotating domain with a value ranging from around 10 m/s at the spinner to a value of 75 m/s. The convergence criteria are reached after 150 time steps, and the power curve gets much faster constant, see figure 3.5.

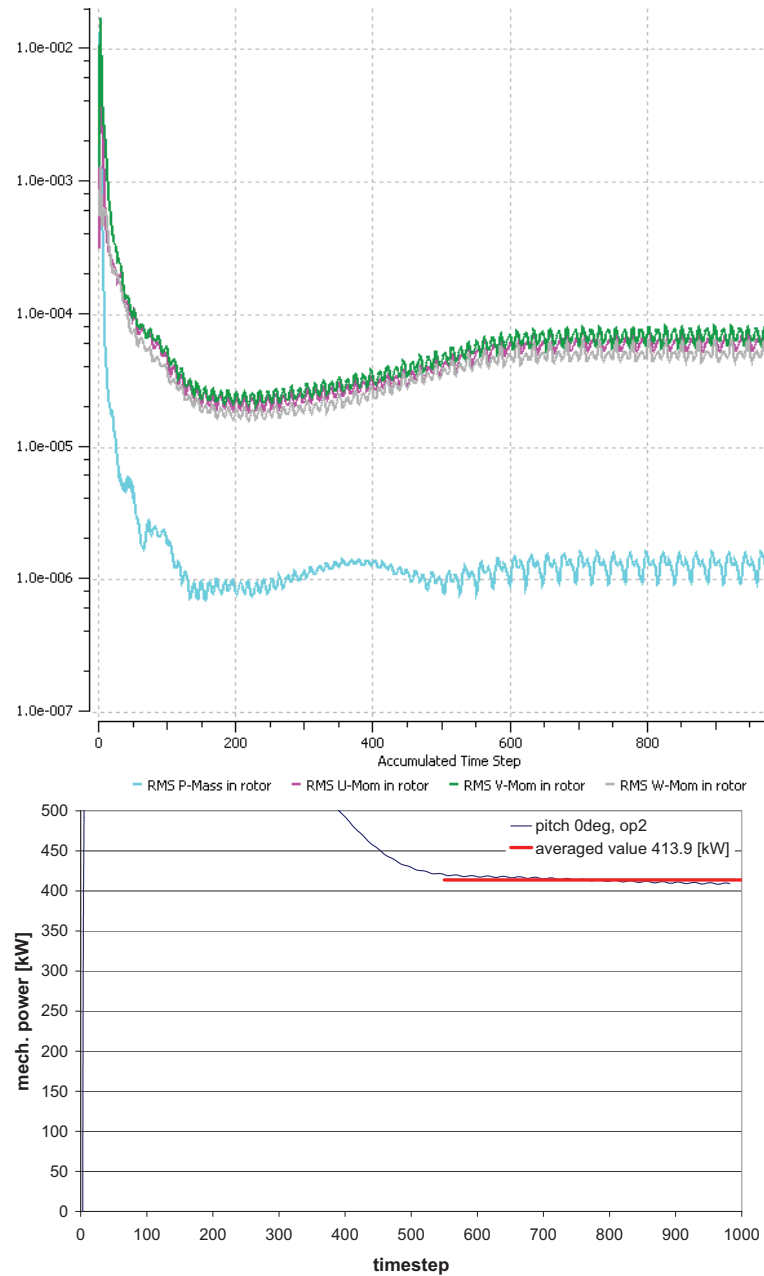


Figure 3.3: The residuals and the power curve for Auto Timescale at operating point 2

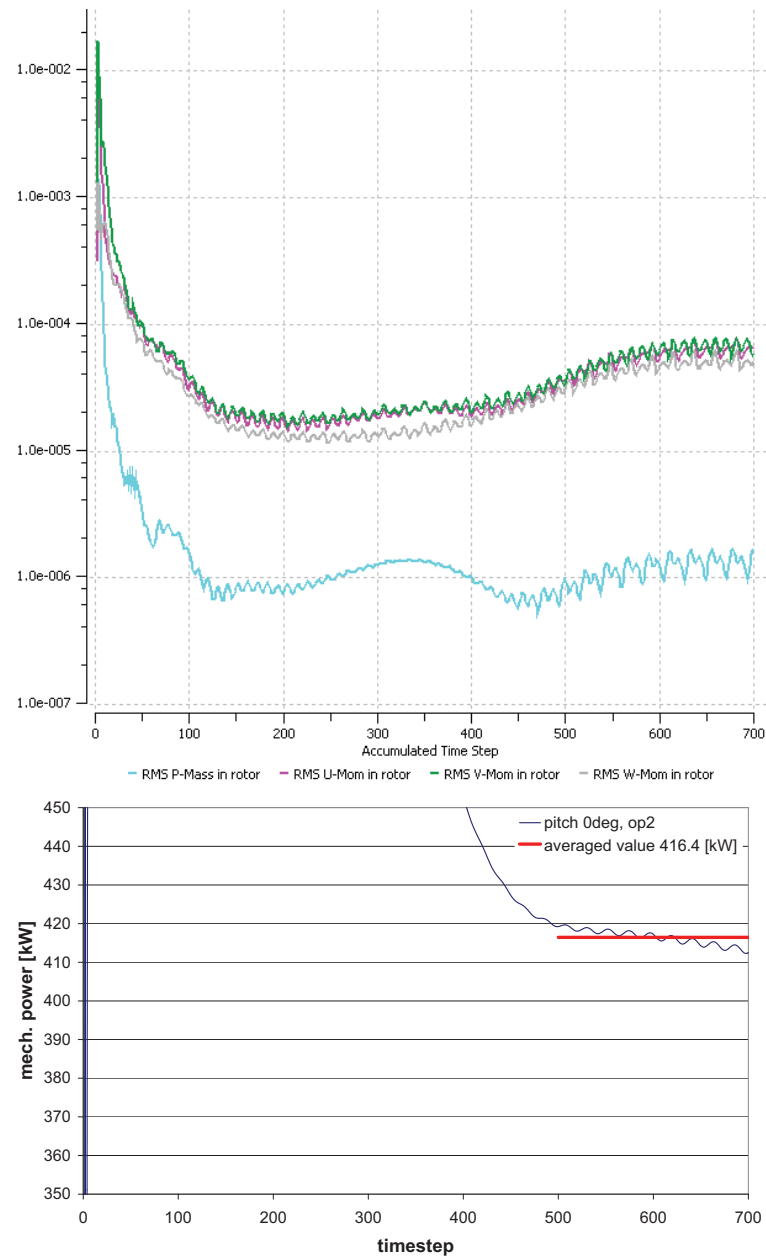


Figure 3.4: The residuals and the power curve for Physical Timescale 0.1s at operating point 2

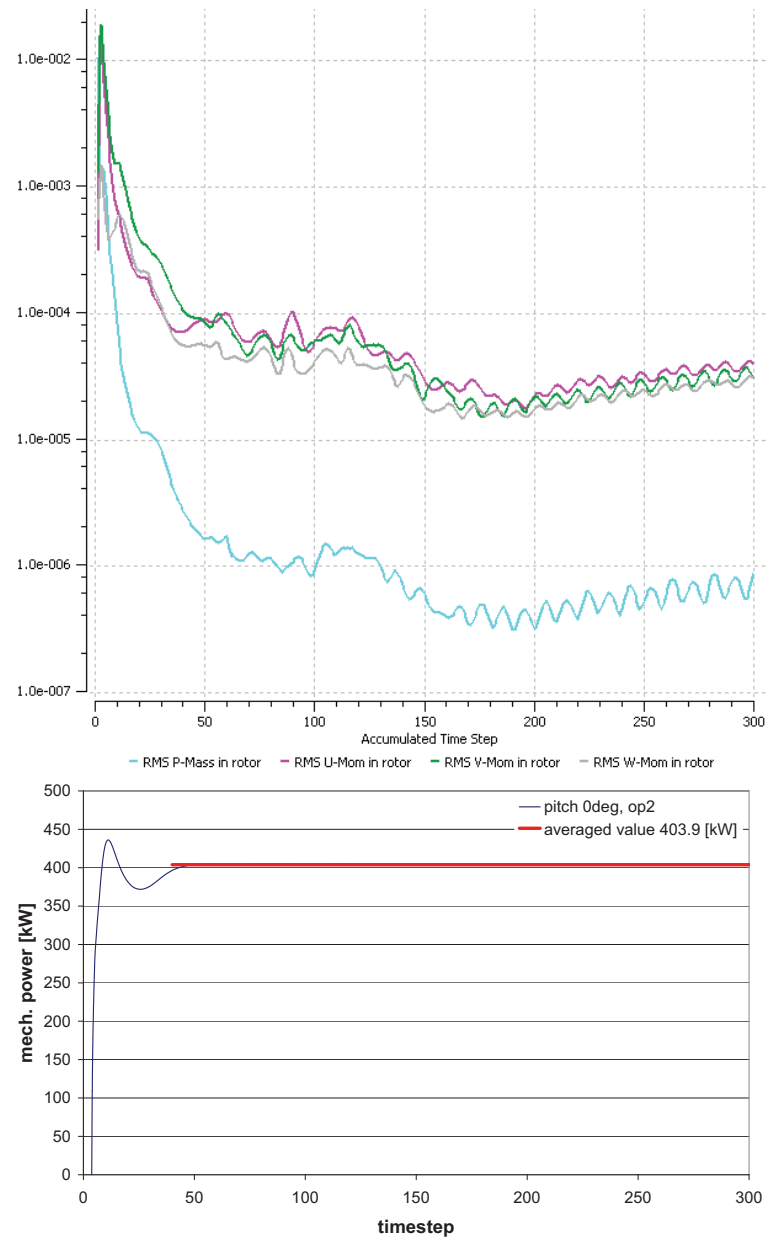


Figure 3.5: The residuals and the power curve for Local Timescale Factor 10 at operating point 2

In order to be able to interpret the convergence behavior of the power curve with Local Timescale Factor 10, figure 3.6 is presented. It displays the average value of 403.93 kW with a maximum deviation of 0.23 percent, calculated from timesteps 50 to 300.

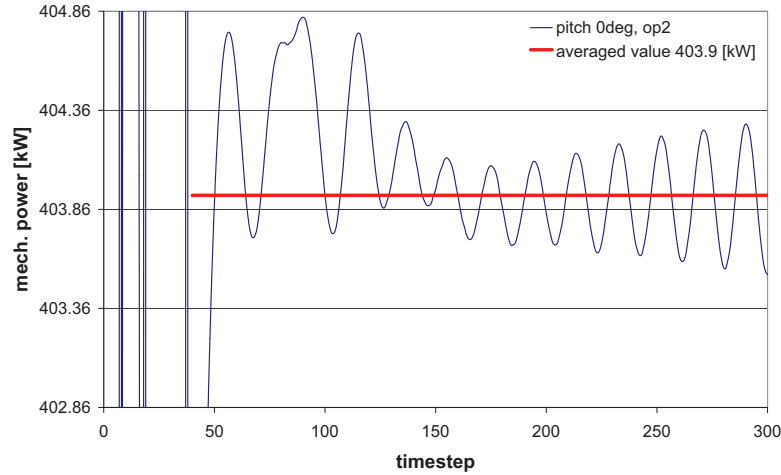


Figure 3.6: A larger scaled view at the power curve chart with Local Timescale Factor 10 at operating point 2

Table 3.3: Comparison, of the different settings, with and without the tip vortex visualization and different inlet boundary conditions

	op3 LTF 10, High Res, -0.8deg						Bladed
	$v = f(z)$				$v = \text{const.}$		
grid size rotor [nodes]	~ 1 700 000		~ 1 100 000		~ 3 400 000		
tip vortex	yes	yes	yes	no	yes	yes	
alternate rotation model	yes	no	yes	yes	yes	yes	
single or double precision	single	single	double	single	single	single	
power [kW]	1761.46	1820.35	1761.31	1847.01	1943.00	1630.00	1838.00

As presented in table 3.3 the settings applied were, the alternate rotation model, single precision, as the use of double precision does not improve the convergence but costs a lot of additional computer memory, and a Local Timescale Factor of 10. With the Local Timescale Factor applied, an adequate exact solution of the power with good residuals was reached.

The summarized settings apply to all simulations realized within the scope of this work:

- alternate rotation model
- single precision
- local timescale factor 10

4 Postprocessing

In this chapter, the results concerning the following details are evaluated:

- mechanical power, power coefficient and mechanical efficiency
- mesh size
- aerodynamic coefficients
- flow physics

One problem was that for the validation no experimental measurements were available. The only data transmitted was the solution of the power calculated by means of the program Bladed. The software Bladed is shortly described in section 4.1. The used meshes are already explained in section 2.3.

4.1 Mechanical Power, Power Coefficient and mechanical Efficiency

Based on the fact that the comparison of the power calculated by the ANSYS software with the power data of the Windtec internal software is not optimal, the results should be evaluated critically.

The Windtec's wind turbine design software is Bladed, that allows users to carry out performance and loading calculations for the design and certification of wind turbines, both on-and offshore. The aerodynamic model uses the blade element momentum theory and the actuator disc theory developed by Rankine, Greenhill and Froude. The 3D effects, i.e. the tip vortex losses, are added by empirical equations.

Blade element theory (BET) is a mathematical process originally designed by William Froude (1878), David W. Taylor (1893) and Stefan Drzewiecki to determine the behavior of propellers. It involves breaking a blade down into several small parts, then determining the forces on each of these small blade elements. These forces are then integrated along the entire blade and over one rotor revolution in order to obtain the forces and moments produced by the entire propeller or rotor. One of the key difficulties lies in modeling the induced velocity on the rotor disk. Because of this the Blade element theory is often combined with the Momentum Theory to provide additional relationships necessary to describe the induced velocity on the rotor disk. [11]

4.1.1 Equations

The maximum achievable power coefficient $c_{P,Betz}$ of 0.59 is idealized. This means that an ideal wind turbine can profit 60 percent from the power of the wind. The idealized velocity in the

rotor plane is $\frac{2}{3} \cdot v_1$, and far away from the rotor the velocity is $\frac{1}{3} \cdot v_1$. The only losses included are the losses caused by the axial velocity at the outlet. But, the real power coefficient is influenced by airfoil efficiency, tip efficiency and spin efficiency, see equation 4.3.

The equation for the maximal power in the wind is:

$$P_{\max} = \frac{1}{2} \cdot \rho \cdot A \cdot v_1^3 \cdot c_{P,\text{Betz}} \quad (4.1)$$

Equation of the power coefficient $c_{P,\text{real}}$:

$$c_{P,\text{real}} = \frac{P_{\text{real}}}{P_{\max}} \cdot c_{P,\text{Betz}} \quad (4.2)$$

A description of the real power coefficient is:

$$c_{P,\text{real}} = \eta_{\text{spin}(\lambda)} \cdot \eta_{\text{tip}(\lambda,z)} \cdot \eta_{\text{airfoil}(\lambda,\epsilon)} \quad (4.3)$$

And equation of η :

$$\eta = \frac{P_{\text{real}}}{P_{\max}} \quad (4.4)$$

Equation of the power calculated in ANSYS CFX:

$$P_{\text{real}} = T_{x\text{-axis}} \cdot \omega \cdot B \quad (4.5)$$

4.1.2 Results

The power achieved was the solution of the steady state simulation.

For the simulations of the power curves, the rotor grids 1, 2, 3, 4 as of table 2.6 in combination with the meshes of inlet, outlet and outer as of table 2.10 were used.

It has to be mentioned that the rotor grids 1, 2, 3, 4 are generated without consideration of the resolution of the tip vortex, and that they were calculated with the boundary condition $\mathbf{v} \text{ in } = \mathbf{f}_{(z)}$. But, for comparison purpose one power curve of operating point 3 was recalculated with the boundary condition $\mathbf{v} \text{ in } = \text{constant}$. And, for operating point 3 with pitch angle -0.8, the solution of the simulation of rotor grid 5 (table 2.6) is displayed in figures 4.3, 4.4 and 4.5 with regard to the tip vortex.

The power curves over the pitch angle for the different operating points (listed in table 3.2) were shown in figures 4.1, 4.2, 4.3 and 4.6. The data in figure 4.4 are calculated with equation (4.2) and show the power coefficient, those in figure 4.5 with equation (4.4) and display the efficiency.

In order to improve the simulations, new meshes were generated, the results of which, are evaluated in the following chapters.

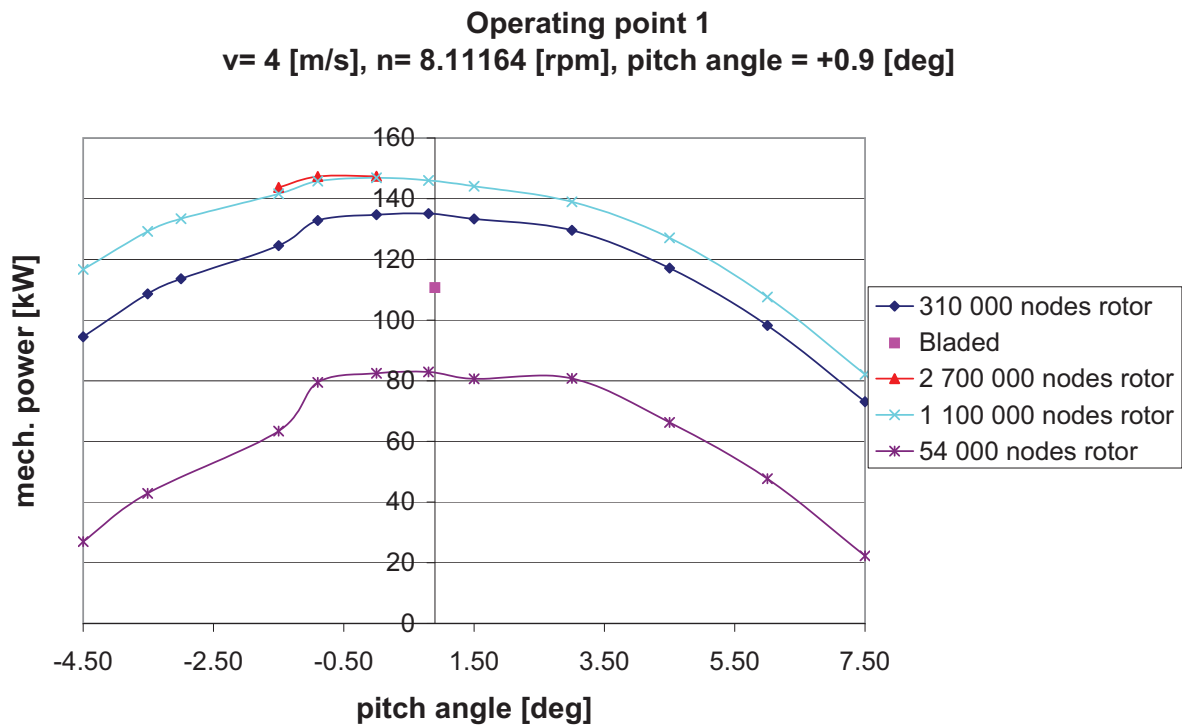


Figure 4.1: The calculated power over the pitch angle with different mesh sizes of the rotor domain for operating point 1

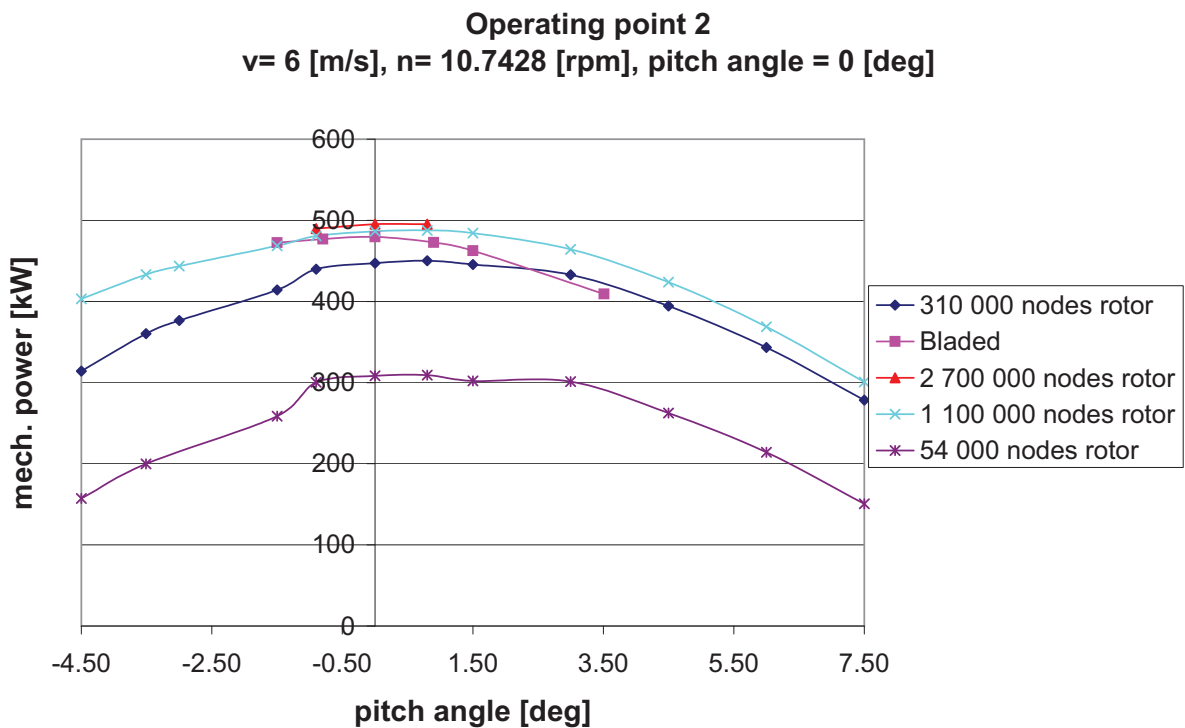


Figure 4.2: The calculated power over the pitch angle with different mesh sizes of the rotor domain for operating point 2

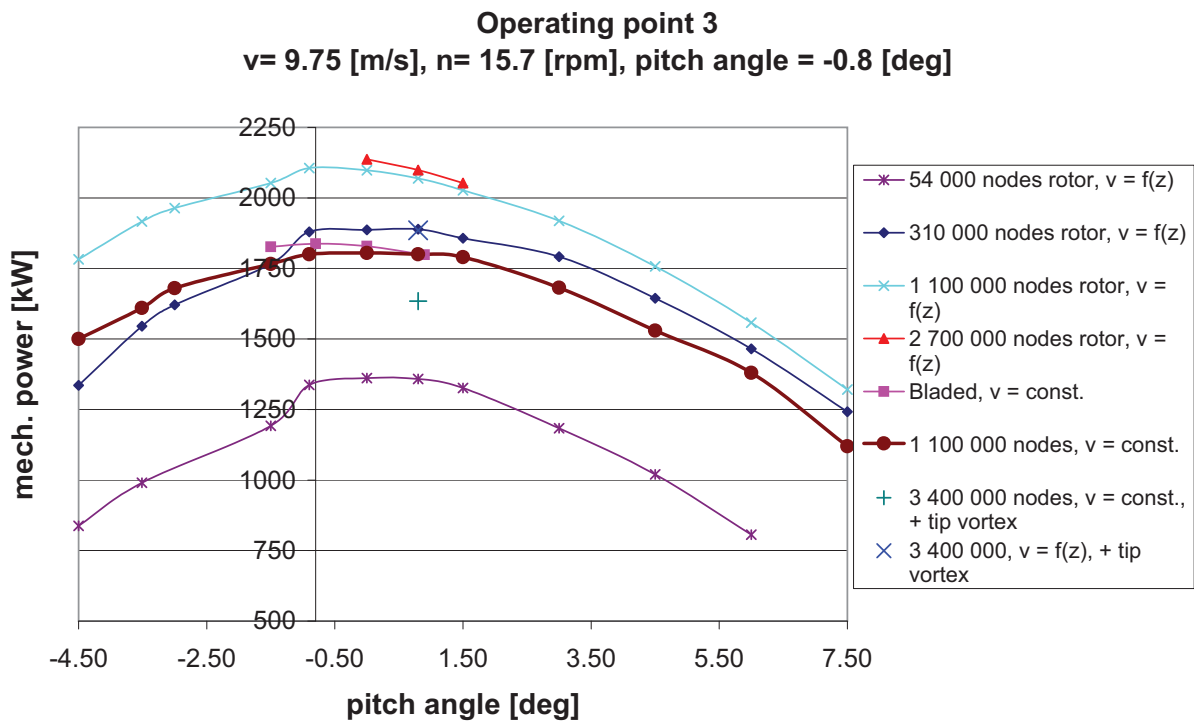


Figure 4.3: The calculated power over the pitch angle with different mesh sizes of the rotor domain for operating point 3, results for different boundary conditions and additionally the results for the tip vortex realization

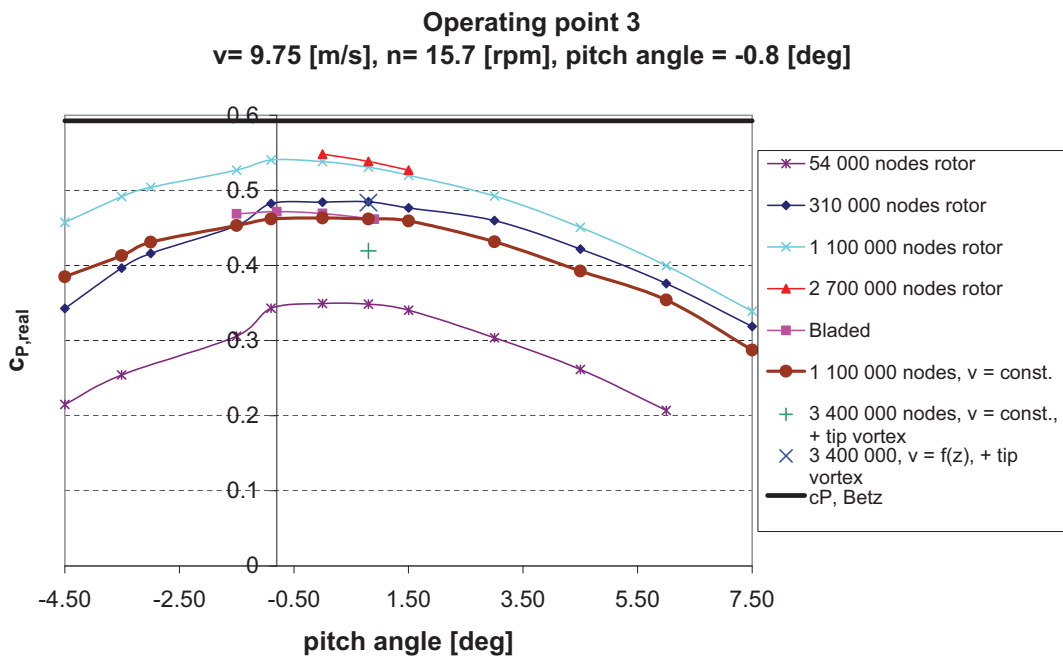


Figure 4.4: The power coefficient over the pitch angle with different mesh sizes of the rotor domain for operating point 3, results for different boundary conditions and additionally the results for the tip vortex realization

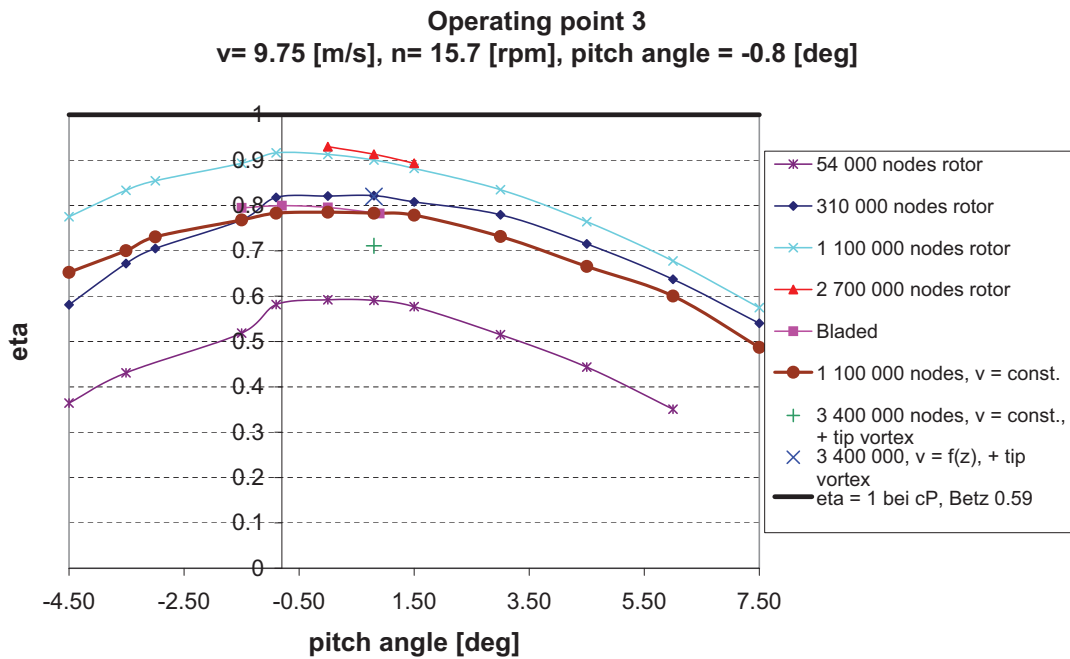


Figure 4.5: The mechanical efficiency over the pitch angle with different mesh sizes of the rotor domain for operating point 3, results for different boundary conditions and additionally the results for the tip vortex realization

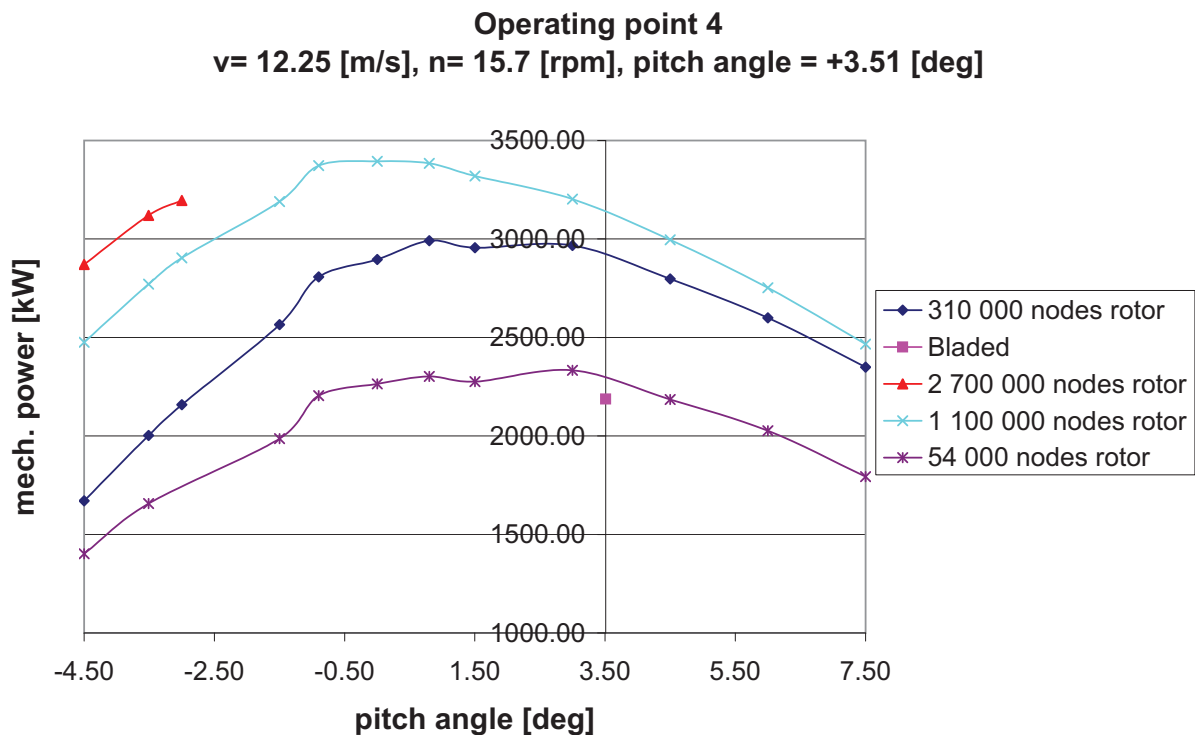


Figure 4.6: The calculated power over the pitch angle with different mesh sizes of the rotor domain for operating point 4

4.1.3 Discussion

For operating point 3 with pitch angle +0.9 degree, a relative error of 9.12 percent, between the power of (3 400 000 nodes rotor, $v = \text{const.}$, + tip vortex) 1634.51 kW and the power of Bladed with 1798.60 kW, is founded. The paper "3D CFD Quantification of the Performance of a Multimegawatt Wind Turbine" shows that the comparison between computed and measured mechanical power output is quite good. The simulated turbine is SWT- 2.3-93 with a blade length of 45m, a tip chord of 0.8m and a root chord 3.5m, the airfoils used are NACA63.xxx and FFAxxx. A really good agreement is indicated, see table 4.1. The boundary conditions are quite similar and the blades have similar geometrical dimensions, as in this work as well. The CFD code of Risø DTU (National Laboratory for Sustainable Energy) is Ellipsys, and the Siemens in-house BEM code is Xblade, which is comparable with Bladed.

Table 4.1: An excerpt of the mechanical power output from paper [4]

Wind speed	RPM	Measured	Ansys CFX	Ellipsys	Xblade
m/s	U/min	kW	kW	kW	kW
6	10	400	396	392	408
8	13.5	986	950	945	967
10	16	1894	1853	1850	1850

These cognitions lead to a discussion of the simulation mistakes. Possible sources of error can be the limited mesh size, whereas this limitation can be found extremely between the interfaces of the domains, especially between rotated and stationary domains. "The "Siemens" computations were run in a parallel computing cluster with 9 Pentium 4 machines, in the year 2007".

As already mentioned, the charts should be read critically. However to get a good understanding of the influence of the boundary condition $\mathbf{v} \text{ in } = \mathbf{f}_{(z)}$, the figure 4.7 is presented. The relative error between $\mathbf{v} \text{ in } = \mathbf{f}_{(z)}$ and $\mathbf{v} \text{ in } = \text{constant}$ is 14.94 percent for a pitch angle of -0.8 degree. And it varies, as it is dependent on the pitch angle. The difference in power are the result of a higher axial velocity with b.c. $\mathbf{v} \text{ in } = \mathbf{f}_{(z)}$, which leads to a higher relative velocity. Power is a result of the lift force see in equationeq:tangential $force$.

The equation of the lift force:

$$L = c_L \cdot \frac{\rho}{2} \cdot c^2 \cdot l_c \quad (4.6)$$

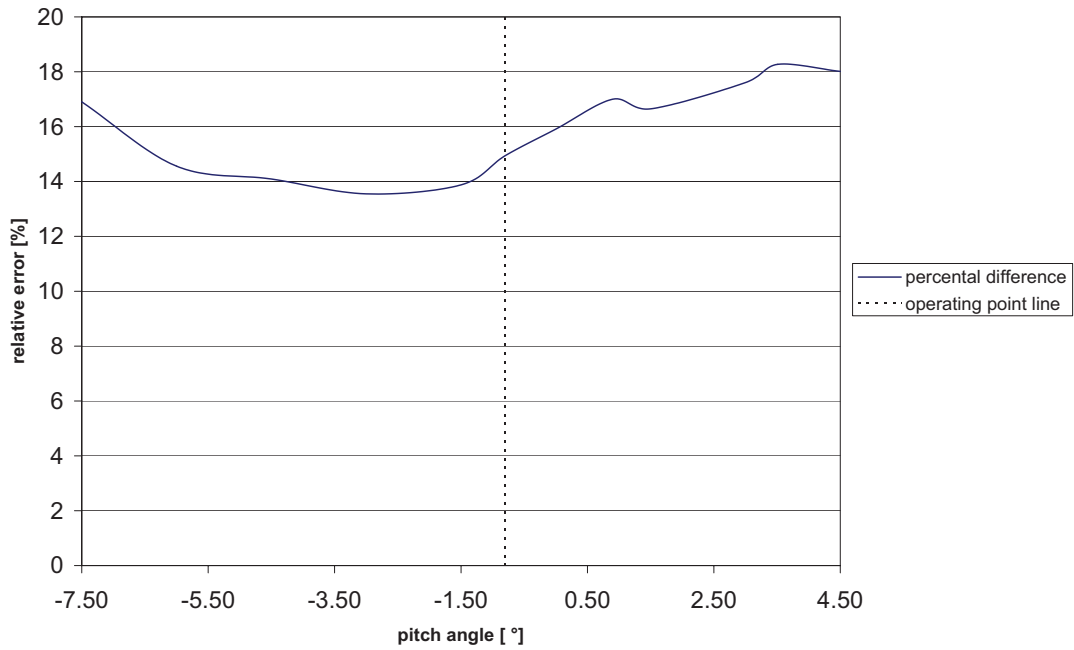


Figure 4.7: Relative error between $v = f_{(z)}$ and $v = \text{const.}$ for operating point 3, with a mesh size of 1 100 000 nodes for the rotor domain

4.1.3.1 Tip Losses

Also, the influence of the **tip loss** is very high. This loss is caused by a flow from the pressure side to the suction side at the tip of every blade. The reaction overlaps with the relative velocity component \mathbf{w} and as a result a snowballing vortex is developed. Betz develops to the concept of a reduced diameter of the rotor blade and together with the idea of Prandtl, this leads to the following equation for the tip efficiency [12]:

$$\eta_{\text{tip}} \approx 1 - \frac{1.84}{B \cdot \lambda_{\text{design}}} \quad (4.7)$$

And with equation

$$\lambda_{\text{design}} = \frac{R \cdot \omega}{v_1} \quad (4.8)$$

it leads to the result for operating point 3 listed in table 4.2.

Table 4.2: Sizes for calculating the tip efficiency (based on [12])

B	[-]	3
R	[m]	46.58
c_2 (Betz)	[m/s]	6.50
n	[rpm]	15.70
ω	[rad/s]	1.64
λ	[-]	11.78
η_{tip}	[-]	0.95

With the different grid sizes of the rotor domain taken into consideration, computations were done with and without a tip vortex realization, as mentioned in chapter 4.1.2 and chapter 2.3, for operating point 3.

A good comparison of the influence of the tip vortex was simulated with one nearly similar grid, where only the outer contour was filled with an expansion of the blocks displayed in figure 2.10. The result of the comparison is a relative error of **4.87** percent, between 1847.1 kW power without tip vortex and 1761.4 kW power with tip vortex. This can be understood as a value of the tip efficiency with a size of ($\eta_{tip} = 1 - 0.0487$) 0.9513. This value is only a relative size, the physical information is passed through the interface, however with numerical errors, as see figure 4.8 (b). Nevertheless the value correlates well with the calculated value listed in table 4.2.

The pressure plot of the two simulations is shown in figure 4.8. One reason for the geometrical enlargement of the rotor domain was that the rotor stator interface was located exactly at the blade tip, and as a result the physics at the blade tip were not correctly computed. A picture of a streamline plot for the tip vortex realization with correct settings is presented in figure 4.9.

One method to split the tip vortex, is the installation of so-called winglets. These are used on wind turbine blades to improve efficiency, besides they reduce drag and noise.

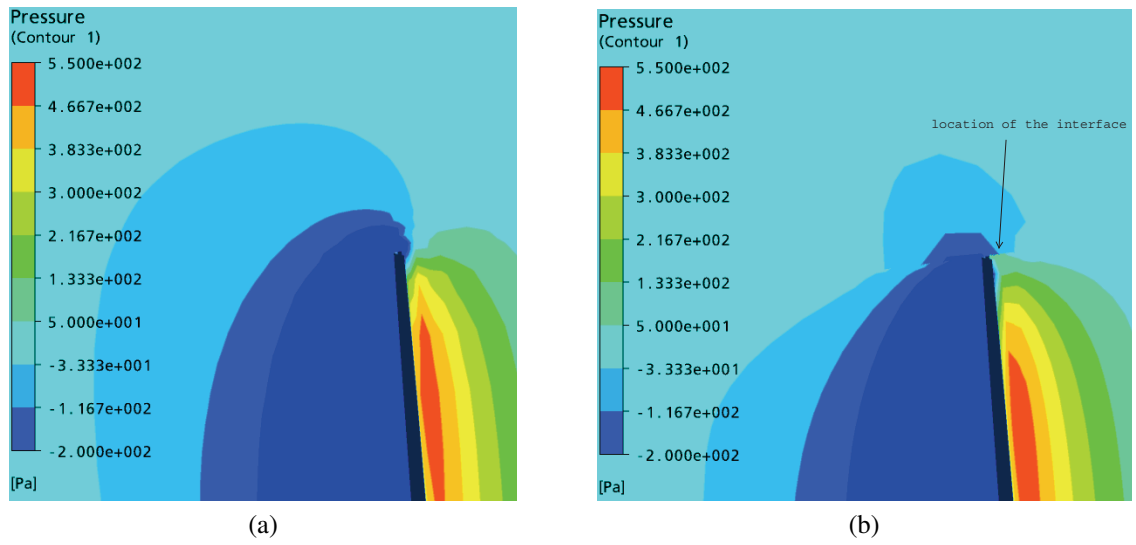


Figure 4.8: 2D pressure plot (a) with realization (b) without realization of the tip vortex

ANSYS

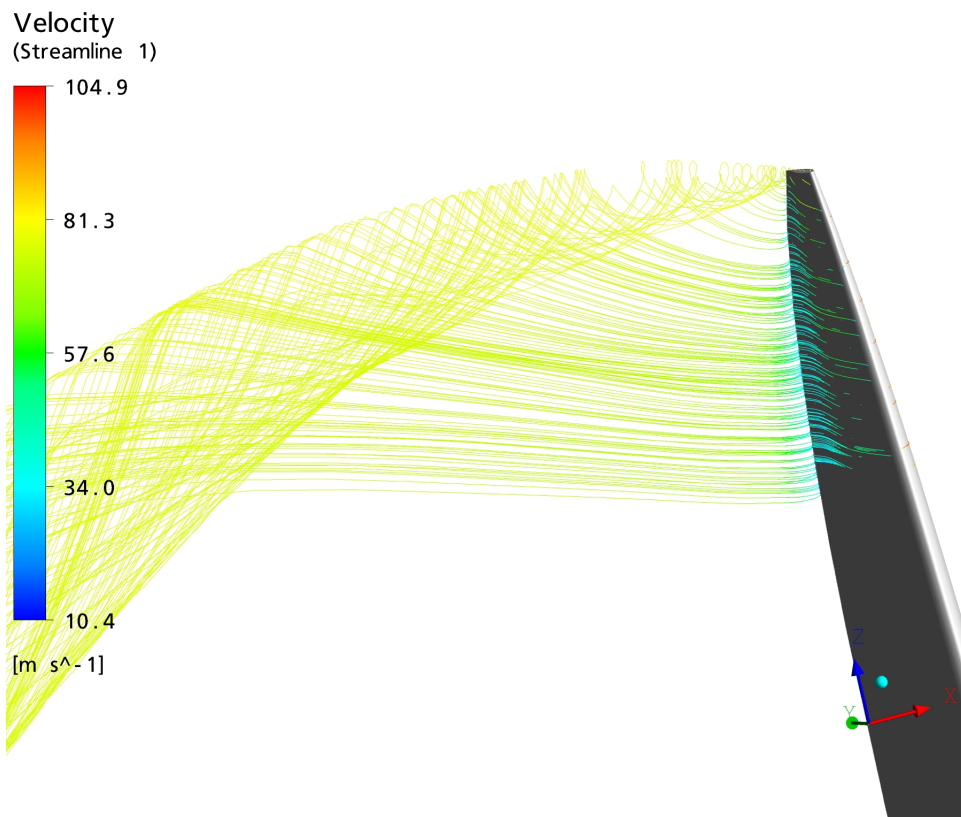


Figure 4.9: 3D streamline plot of the tip vortex

4.1.3.2 Airfoil Losses

The airfoil losses are described in section 4.3.3.

4.1.3.3 Spin Losses

The **spin losses** of the wind turbine are caused by the torque output from the air, as the circumferential force with the lever arm indicates a counter torque in the air. For fast runner turbines with $\lambda > 3$ spin losses are negligible. Figure 4.10 displays how Schmitz' theory includes the spin loss.

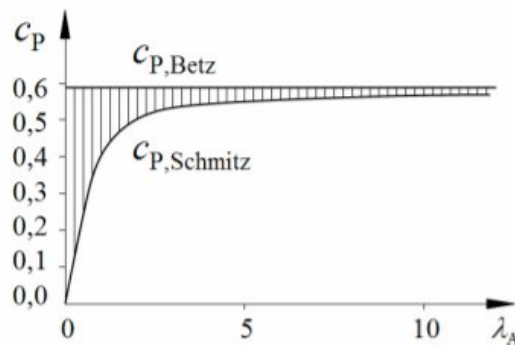


Figure 4.10: According to Betz and Schmitz, the power coefficient over tip speed ratio is displayed, the hatched area describes the spin loss [12]

A visualization of the spin with the tip vortex is presented in the picture of an experiment at Risø National Laboratory (Denmark) and is displayed in figure 4.11 (b), together with the theory of the spin flow displayed in figure 4.11 (a).

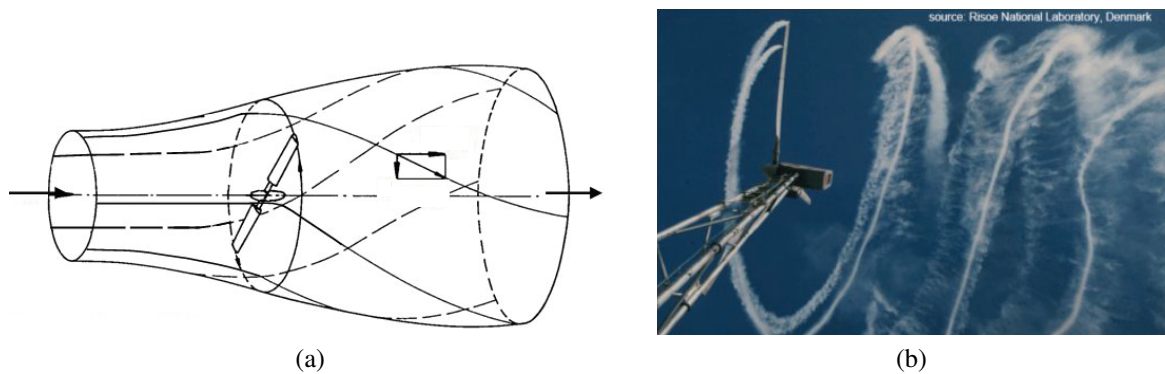


Figure 4.11: Spin flow (a) sketch [12] (b) with additional tip vortex

4.2 Mesh size

Mesh size depends on the geometrical dimensions of the simulation and the computer resources available. These two parameters determine the size of the grid cells. One part of the present thesis was to find out which mesh size is necessary to get adequate results. As of the physical behavior of the single domains the mesh was varied– in the **rotor domain** without a variation of the surrounding area and the **surrounding area** without a variation of the rotor domain.

The large volume of the whole model led to regions with a finer grid and regions with a coarse grid. First tests were done with a variation of the rotor domain mesh. For the rotor domain mesh size study, meshes 1, 2, 3, and 4 were used, listed in table 2.6. Based on **mesh 2** grid size was varied, globally. Globally represents a multiplication in every single coordinate direction of the grid. The multiplication factors are:

- 0.5 (mesh 1)
- 1.5 (mesh 3)
- 2 (mesh 4)

As a result of this variation, one mesh size of the rotor domain could be found. The deviations from mesh 4, to the other meshes are listed in table 4.3. The conclusion to be made was that **mesh 3** with a number of 1 138 050 nodes provides satisfy results. For first tests the meshes

Table 4.3: Mesh size study for operating point 3, with relative error, pitch angle +0.8 [deg]

mesh		power [kW]	relative error [%]
1	54 000 nodes rotor, $v = f(z)$	1358	-35.30%
2	310 000 nodes rotor, $v = f(z)$	1889	-10.00%
3	1 100 000 nodes rotor, $v = f(z)$	2069	-1.43%
4	2 700 000 nodes rotor, $v = f(z)$	2099	0.00%

were built without attention to y^+ . Thus the values for the meshes in table 4.3 could be regarded as relative values. As a consequence, the y^+ value, which is a dimensionless value for the first wall projection to resolve the boundary layer, was minimized. But, as a conclusion of the results presented in table 4.3, the resolution of the rotor domain mesh should be in a range of 1 000 000 to 2 000 000 nodes. However, the creation of an adequate y^+ value of the rotor domain leads to higher grid resolutions because of the additional cells around the blade. A good wall resolution leads to extremely flat surface elements. With the third dimension these elements yields bad aspect ratios. Therefore a compromise between a sensible aspect ratio and a sensible y^+ value had to be made. In order to fulfill the requirements mentioned a new rotor mesh size study was realized, see chapter 4.2.2.

4.2.1 Surrounding Mesh Size Study

The used surrounding dimensions are listed in chapter 2.3.2. In order to get a detailed view of the dependence between mesh size and flow, a variation of the grid size was realized. In table

4.4, the mesh sizes of the domains are listed. Mesh 1 was the commonly used mesh for all computations.

Table 4.4: Mesh sizes of the different surrounding domains

mesh	1	2
	[nodes]	[nodes]
inlet	979 047	3 543 150
outlet	851 445	2 520 000
outer	315 000	3 665 268

All charts are referred to the global Cartesian coordinate system, with its origin in the intersection point of the pitch axis with the rotational axis, the x-direction starting at this origin point leads streamwise to the outflow, the z-axis is oriented in blade tip direction and the y-axis is directed to the trailing edge of the airfoils.

4.2.1.1 Inlet

Chart 4.12 shows the differences between the maximal and the minimal velocity on a plane. The plane displayed is the yz-plane which is varied from the inflow to the outflow of the inlet domain. On the one hand it is shown that the geometrical dimension of the inlet domain is too big, whereas 150 meters away from the origin point the difference between the velocities is less than 0.1. On the other hand the influence of the mesh size proves to be insignificant. Only from 3 to 9 meters away from the origin their is a relative error between +28 and -10 percent. Reasons for this are the high velocity and pressure gradients of the flow in front of the rotor. As the undisturbed incidence flow hits the rotating blade with the hub, an enlargement of the streamtube is caused.

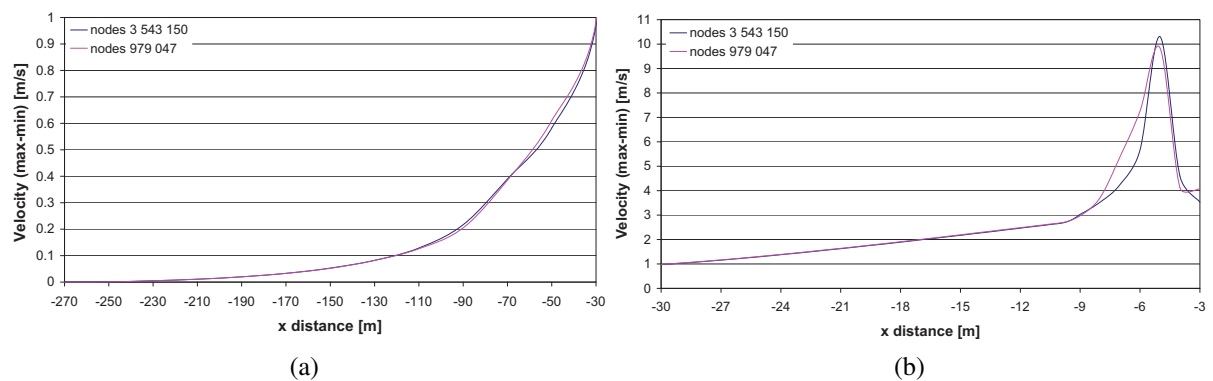


Figure 4.12: Chart of the velocity difference on yz plane at inlet domain, (a) chart has a x-axis range from -270 to -30 meters, (b) has a range from -30 to -3 meters

The results displayed in chart 4.12 are verified by creating lines through the model, which yield an absolute physical size with the local coordinates for each point on the line. In this case, the

line was drawn from inflow to outflow of the inlet domain, with y distance zero and with a variation of the z value from 10 to 450 meters. For the results see chart 4.13.

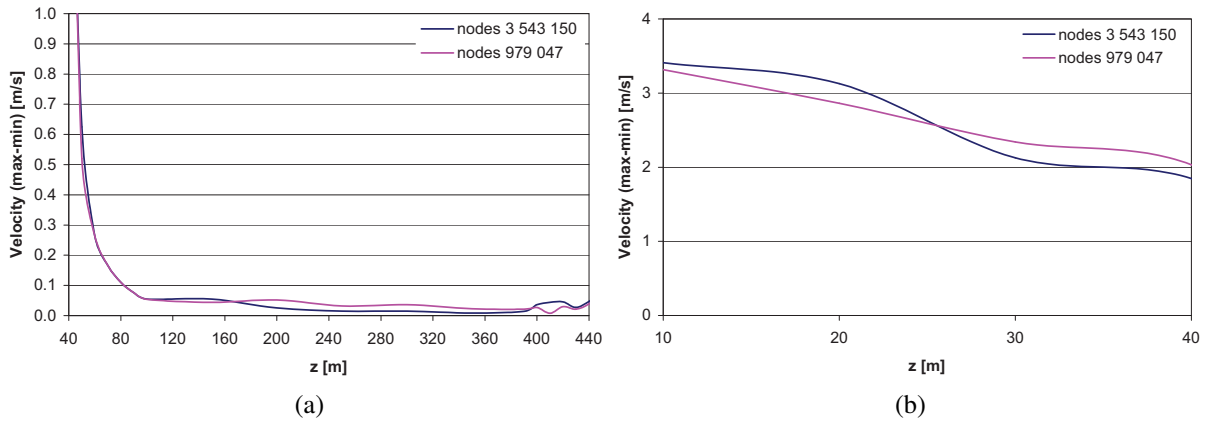


Figure 4.13: Chart of the velocity difference on lines at inlet domain, (a) chart has a x-axis range from 40 to 450 meters, (b) has a range from 10 to 40 meters

As a consequence of this evaluation the x distance of the inlet domain could be reduced from 270 meters to 150 meters, with a finer mesh resolution near the rotor domain. However, in general the influence of the chosen mesh size is marginal.

Chart 4.13 displays the influence of the rotor which can be regarded as the maximum delta velocity of 3.5 m/s with a z-value of 10 meters which leads to nearly zero at 80 meters. As a result of this evaluation the radius of the cylindrical domains could be reduced, however, in order to provide detailed information the same procedures were realized with the outer domain and with the outlet domain.

4.2.1.2 Outer

The outer mesh 2, as listed in table 4.4, was nearly 10 times bigger than the commonly used mesh. The first meters in radial direction of the outer domain not only represent the widened streamtube, but also the tip vortex flow. This enhances the hope that a finer grid in this area can reproduce gradients in a better way. As shown in chart 4.14, the x distance of -10 to +10 meters is the area where the rotor domain is located. Furthermore, the rotational domain is connected to the stationary outer domain by means of a frozen rotor interface. The located interface leads to high velocity differences in this area. But, for a better understanding cutting planes in other spatial directions were used, see chart 4.15.

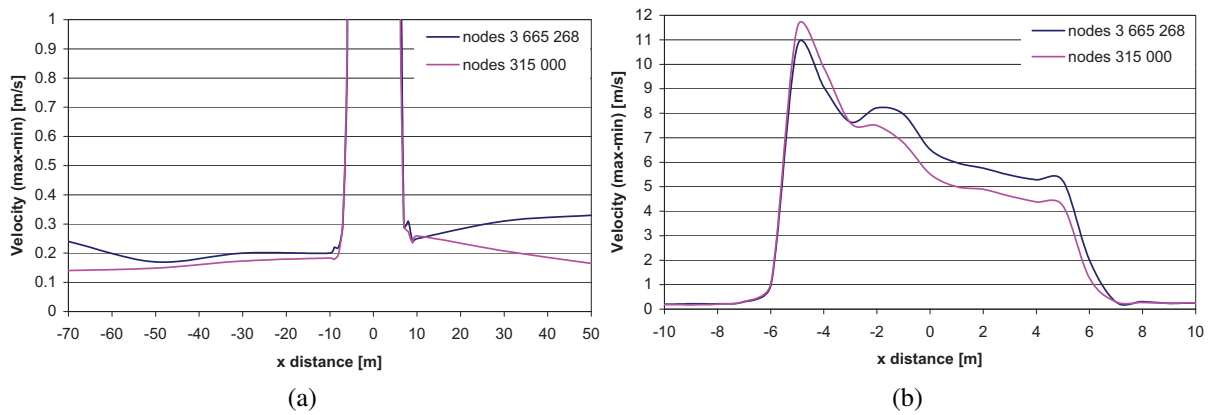


Figure 4.14: Chart of the velocity difference on yz plane at outer domain, (a) chart has a x-axis range from -70 to +50 meters, (b) has a range from -10 to +10 meters

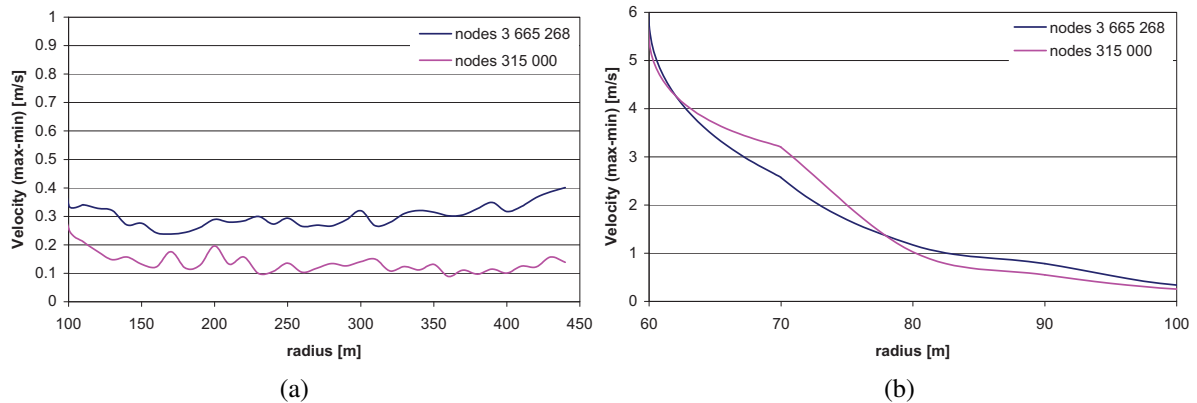


Figure 4.15: Chart of the velocity difference on a surface of revolution with outer domain mesh 1 in comparison to mesh 2, (a) chart has a x-axis range from 100 to 440 meters radius, (b) has a range from 60 to 100 meters radius

The interface mentioned is located at a radius of 55 meters. The results evaluated in chart 4.15 (b) show the importance and the influence of a refinement of the area from 60 to 100 meters radius. The results displayed in chart 4.15 (a) show the significant difference between the two meshes, however, it has to be mentioned that the surface of revolution protruding every single domain so that the location of the minimal velocity is still not known. Therefore, lines through the outer domain were used to get the velocity information. These results are displayed in chart 4.16. The lines are going in x-axis direction from inflow to outflow at the outer domain whereas the y coordinate is zero and z ranges from 60 to 450 meters.

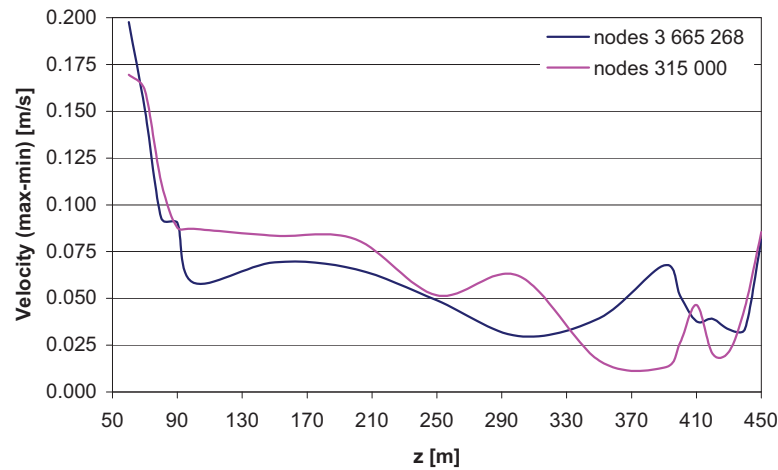


Figure 4.16: Chart of the velocity difference on lines through the outer domain, x-axis range from 60 to 450 meters

So one can conclude that the outer domain mesh study induces future work. The mesh size of the outer domain must be 2 to 3 times finer than mesh 1 and, additionally a local refinement in the area of the interface has to be realized. Chart 4.16 also shows the tendency to reduce the radius of the cylindrical domain.

4.2.1.3 Outlet

Mesh 2, used for the outlet domain, does not show any significant difference with regard to the results in comparison to mesh 1. But, it is presented that the wake flow does not disappear at a distance of 450 meters, see chart 4.17.

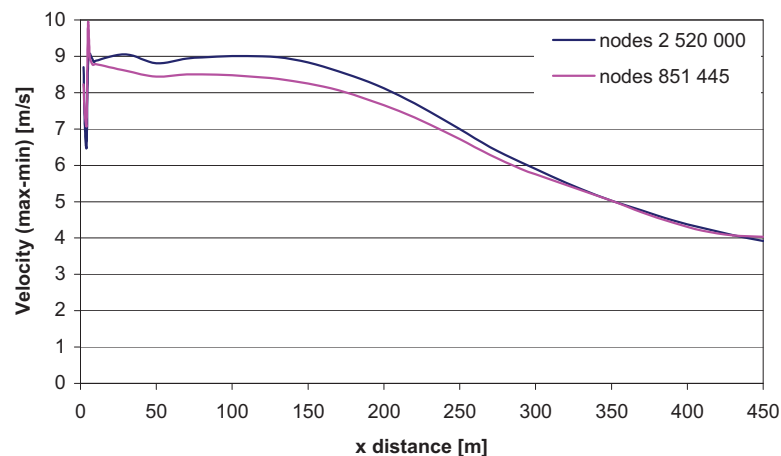


Figure 4.17: Chart of the velocity difference on yz plane at the outlet domain

The difference of the velocity on the yz plane is a measure for an uniform velocity distribution, and at a x-distance of 450 meters the value is still 4 [m/s]. This phenomena, which is produced by the rotor wake flow, is displayed in figure 4.18.

Based on these results of the surrounding mesh study, the domains were scaled down, however, an enlargement of the length of the outlet domain from 450 meters to 550 meters was realized:

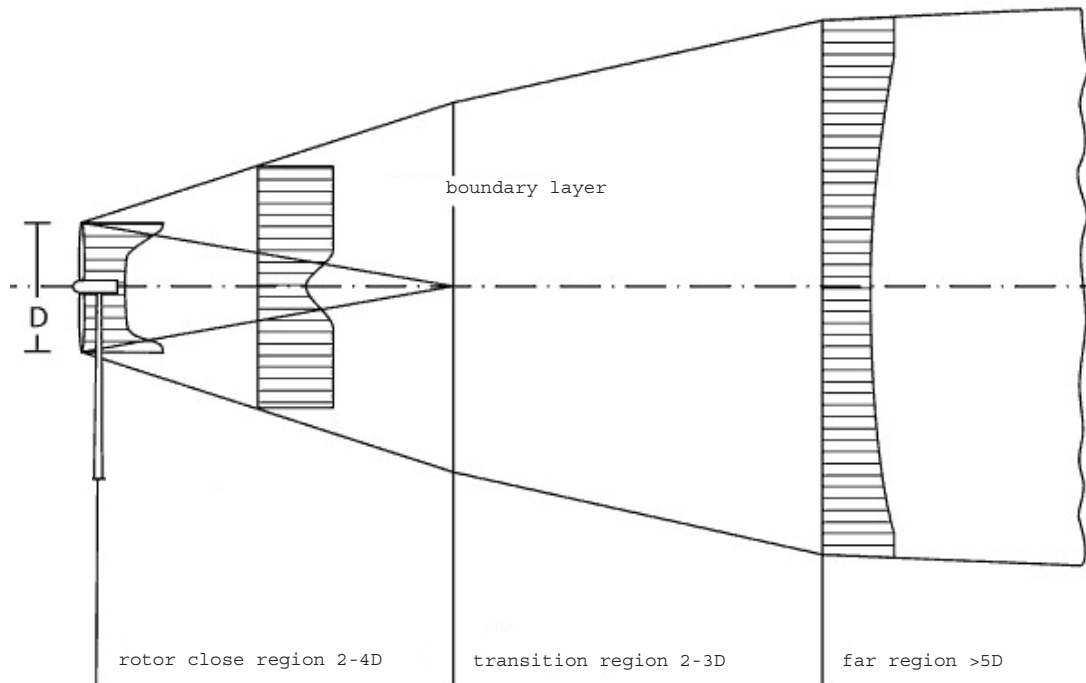


Figure 4.18: Figure of the rotor wake flow [13]

- **INLET:** length 150 [m], radius 250 [m]
- **OUTLET:** length 550 [m], radius 250 [m]
- **OUTER:** radius 250 [m]

These are the surrounding domain meshes used in chapter 4.2.2.

4.2.2 Rotor Mesh Size Study

In this chapter a new rotor mesh is realized. On the one hand it was absolutely necessary to correct false boundary conditions, as well as incorrect pitch angle references, and on the other hand it was of my great personal interest to provide the experience accrued during my work to improve the meshes.

The improved meshes were:

- **Inlet**, with new geometrical dimensions but same mesh size, listed in table 4.4 as mesh 1
- **Outlet**, same procedure
- **Outer**, same procedure
- **Rotor**

The surrounding meshes were refined, geometrical dimensions were minimized, but mesh size was kept constant. However, attention must be drawn to the rotor domain mesh:

- **Verification** of the pitch angle with a reference airfoil
- **Refinement** dimensionless wall distance y^+
- **Subjective** quality check of the grid around the airfoil

A communication mistake with a wrong information on the blade coordinate system led to an incorrect declaration of the pitch angle. The reference airfoil which determines the 0 degree pitch angle, is an airfoil of the WT93/DF2000 wind turbine with a distance of 38 meters from the root, a chord length of 1.24 meters and a twist angle of -0.01 degree. This means that the chord line of this airfoil in relation to the rotation axis declares the used pitch angle. In addition, the positive rotating direction is declared as follows: the leading edge of the airfoil must be turned against the direction of flow. From this new point of view, the blade pitch angle was checked and corrected.

Also, the boundary condition inlet was set to a constant wind profil.

Another detail to improve was the y^+ size. My interest was to reduce the spacing of the first node, away from the blade wall. In the ANSYS Solver Theory Guide, an estimate equation (4.9) for the first node spacing depending on the local Reynolds number, was given, whereas the estimates are based on the correlations for a flat plate [9]. Additionally, it must be mentioned that for a good resolution of the boundary layer the number of nodes in the boundary layer is important as well. ANSYS suggests:

- 10 nodes for the wall function
- 15 nodes for a low-Re model

With an estimation for the boundary layer thickness δ for a blunt body, see equation 4.11.

$$\Delta y = l_c \cdot \Delta y^+ \cdot \sqrt{74} \cdot Re_L^{-\frac{13}{14}} \quad (4.9)$$

$$Re_L = \frac{u \cdot l_c}{\nu} = \frac{\text{Inertial Force}}{\text{Viscous Force}} \quad (4.10)$$

$$\delta = 0.14 \cdot l_c \cdot Re_L^{-\frac{1}{7}} \quad (4.11)$$

The block structure of the whole rotor domain was divided into several blocks, the reasons are explained in chapter 2.3.1. With the blade wall edges \mathbf{k} (see figure 2.9) a determination of the spacing of the first node was possible. As listed in table 4.5, the edges of the split blocks with a different radius were used to calculate the necessary Δy for a desired Δy^+ of 20.

The ANSYS suggestion for the number of nodes in the boundary layer was not feasible. As listed in table 4.5, the single δ values are not convertible to set them as length for the blade wall edges \mathbf{k} . So, with this values a creation of the mesh was not possible. This meant that setting the length of these edges to a value within a creation was possible.

Table 4.5: Determination of the first node spacing Δy away from blade wall, for a desired y^+ value of 20

Block index	r	l_c	u	c	w	Re	Δy	δ
	[m]	[m]	[m/s]	[m/s]	[m/s]	[-]	[mm]	[mm]
3	8.00	3.60	13.15	9.75	16.37	4.5E+06	0.41	14.14
4	20.00	2.25	32.88	9.75	34.30	5.8E+06	0.20	8.51
5	30.00	1.51	49.32	9.75	50.28	5.7E+06	0.14	5.72
6	38.00	1.24	62.48	9.75	63.23	5.9E+06	0.11	4.68
7	44.00	0.74	72.34	9.75	72.99	4.1E+06	0.09	2.93

The ANSYS post surface contour plots of the blade wall with y^+ value show that the value of y^+ is higher on the suction side than on the pressure side, as of the higher velocity and lower pressure on the suction side. As a consequence, the Δy value on the blade suction side was halved. This led to a good distribution of the y^+ value between 0 and 20 over the whole blade, except the hub and near hub region.

The last step to improve the grid quality was, to resize the O-grid edges (see figure 2.9) around the blade, in order to get a subjective smooth grid in the xy plane. Also, the number of nodes in chordwise direction was refined to get a flusher surface of the airfoil. As example, the figure of the smooth grid at a height of 40 meters is shown in figure 4.19.

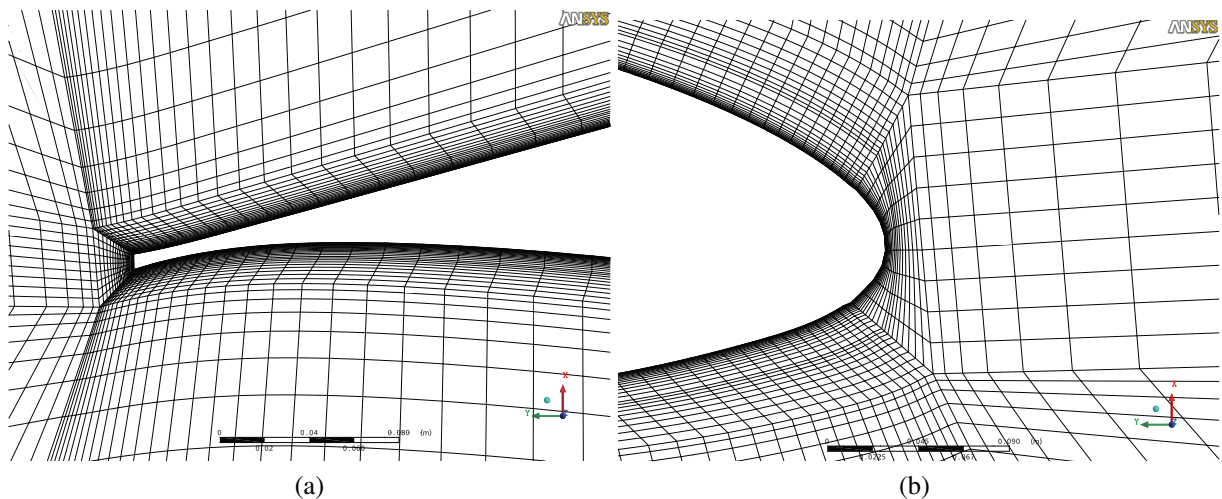


Figure 4.19: Figure of the grid around the airfoil in xy plane at 40 meters, (a) view at the trailing edge, (b) view at the leading edge

With these adjustments, a few meshes were recreated to evaluate the power curve of the simulation in comparison to the curves of the company Windtec. The meshes created are listed in tables 4.6 and 4.7.

The mesh resolution fine with a scale factor of 0.8 was used to simulate the different pitch angles, from -3 degrees to + 3 degrees. The results in power, in efficiency and in power coefficient

Table 4.6: New mesh size study grids for the rotor domain with the scale size

Mesh	Mesh size	Scale size	Nodes	Quads	Hexas
1	coarse	x 0.4	296 349	36 016	278 240
2	middle	x 0.6	977 371	80 856	936 792
3	fine	x 0.8	2 264 937	142 144	2 193 664
4	very fine	x 1	3 928 112	208 962	3 823 389

Table 4.7: Simulation matrix with the recreated meshes, the red x in the table marks the simulated meshes

		1 coarse	2 middle	3 fine	4 very fine
nodes	-	296 349	977 371	2 264 937	3 928 112
quads	-	36 016	80 856	142 144	208 962
hexas	-	278 240	936 792	2 193 664	3 823 389
pitch angle	3	x	x	x	x
pitch angle	1.5	x	x	x	x
pitch angle	0.9	x	x	x	x
pitch angle	0	x	x	x	x
pitch angle	-0.8	x	x	x	x
pitch angle	-1.5	x	x	x	x
pitch angle	-3	x	x	x	x

are displayed in figures 4.20 and 4.21. The reason for using the mesh fine is, that in the mesh study the difference of the power was the lowest between Bladed result and simulation with fine grid, see figure 4.22.

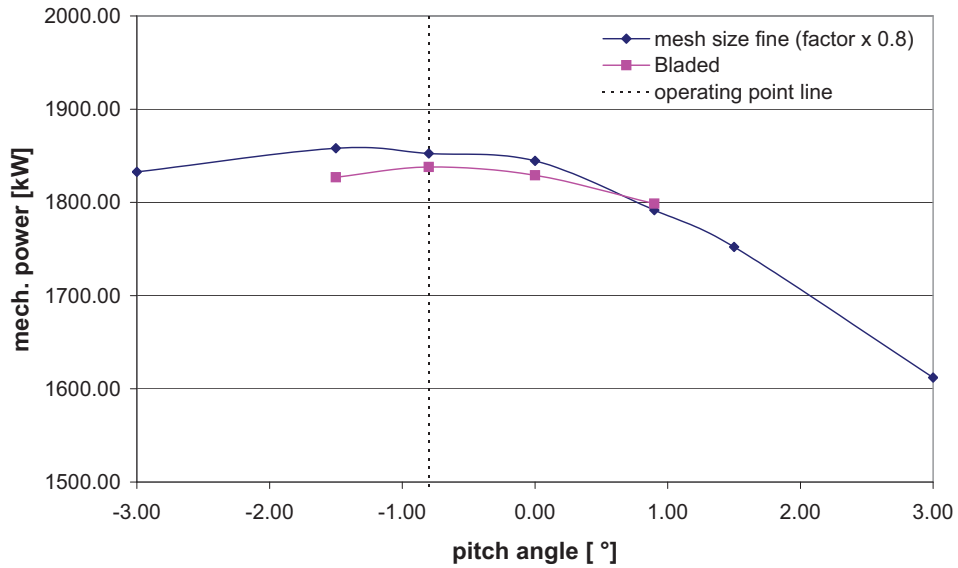


Figure 4.20: Result of mechanical power for operating point 3, ANSYS versus Bladed

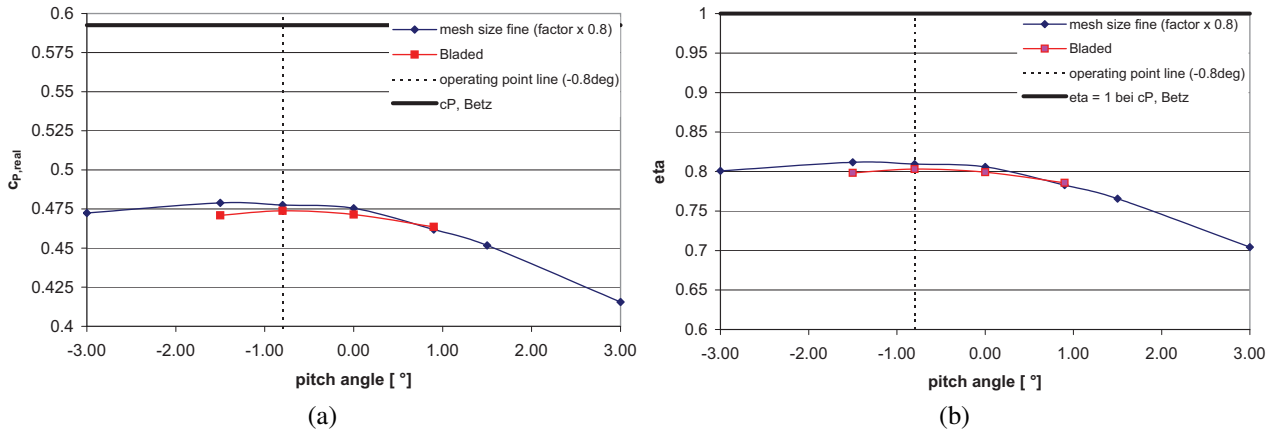


Figure 4.21: Results for operating point 3, (a) power coefficient curve, (b) efficiency curve, ANSYS versus Bladed

The compromise between the y^+ value, and the aspect ratio is at the expense of a bad aspect ratio over the rotor domain mesh. However in order to appreciate the influence of the aspect ratio a comparative simulation was done. This simulation was computed by the company Windtec with their powerful workstation. The rotor domain mesh fine was refined in blade tip direction (spanwise) nearly 4 times to minimize the aspect ratio, but, the grid resolution in the xy plane was stayed constant. The result of the refinement was a rotor domain mesh with approximately **8 million nodes**. Furthermore the solver was started with double precision to reduce rounding errors caused by the still quite high aspect ratio. The mesh achieved provides so-called **high fidelity** resolution.

The results for different mesh sizes with a constant pitch angle of -0.8 degree are displayed in figure 4.22.

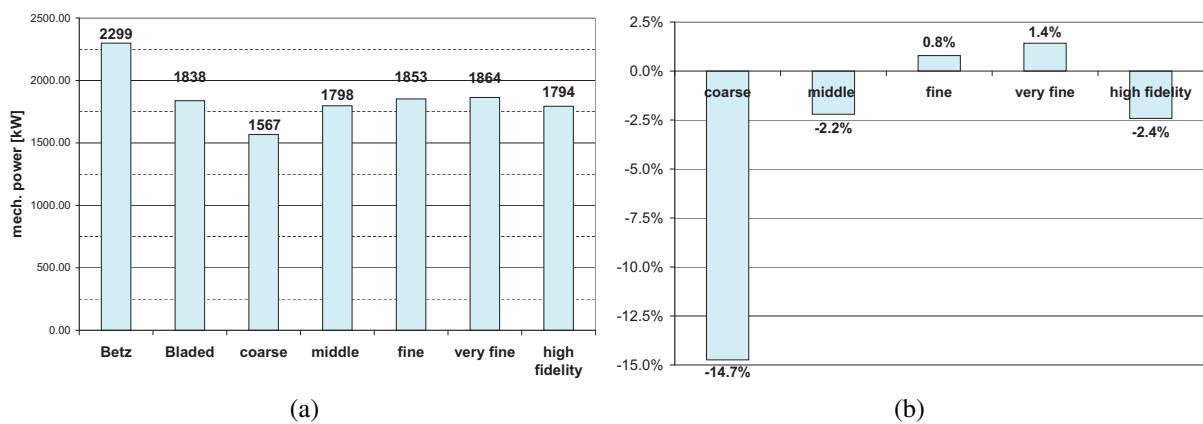


Figure 4.22: Results for operating point 3 with pitch angle -0.8 degree, with a nearly constant averaged y^+ value of 17, (a) mechanical power, (b) deviation from Bladed

At this point, the deviation to the result of Bladed are quite low, however a trend to one rotor mesh setup is still not visible. Hence, the y^+ values and the aspect ratios were evaluated for the rotor wall blade. The evaluation is listed in table 4.8.

Table 4.8: Y^+ and aspect ratio values for the meshes displayed in figure 4.22

mesh	nodes	y^+ averaged	y^+ min value	y^+ max value	aspect ratio averaged	aspect ratio min value	aspect ratio max value
coarse	296 349	17.6	0.5	449.1	4 107.5	13.6	23 279.9
middle	977 371	17.6	0.3	456.5	3 042.7	8.9	22 183.9
fine	2 264 937	17.1	0.7	462.4	2 291.6	5.4	21 462.9
very fine	3 928 112	16.6	0.8	462.8	1 875.9	3.6	18 820.3
high fidelity	8 027 913	18.5	0.5	466.7	605.3	4.4	6 465.9

As listed above, the y^+ values are constant over the different meshes, however for further inves-

tigations the idea of a refinement in chordwise direction was born. The chordwise resolution should have a great influence on the drag coefficient and a lower influence on the lift coefficient. These influences on the coefficients result in an difference in power. The method of extracting power from the profile coefficients is explained in chapter 4.3.3.3.

The chordwise resolution based on the rotor mesh middle, was varied as follows:

- 50 nodes chordwise
- 100 nodes chordwise
- 150 nodes chordwise
- 200 nodes chordwise
- 250 nodes chordwise

The results are shown in figure 4.23,– the trend to a lower power with higher grid resolution is visible. But, the curve trend shows that for a finer resolution a lower mechanical power could be expected. Also, the influence of the aspect ratio, which can be seen as a measure of the element size in spanwise direction in this case, is of great interest. The difference in power, between the **fine** and the **high fidelity** mesh is displayed in figure 4.24.

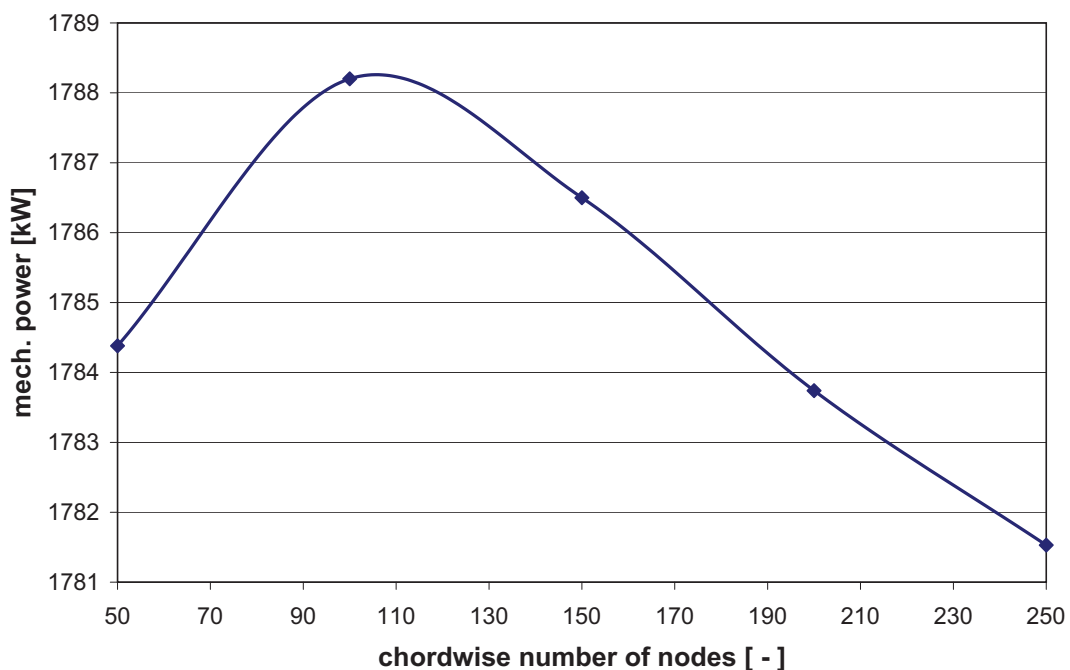


Figure 4.23: Influence of the chordwise refinement on the mechanical power

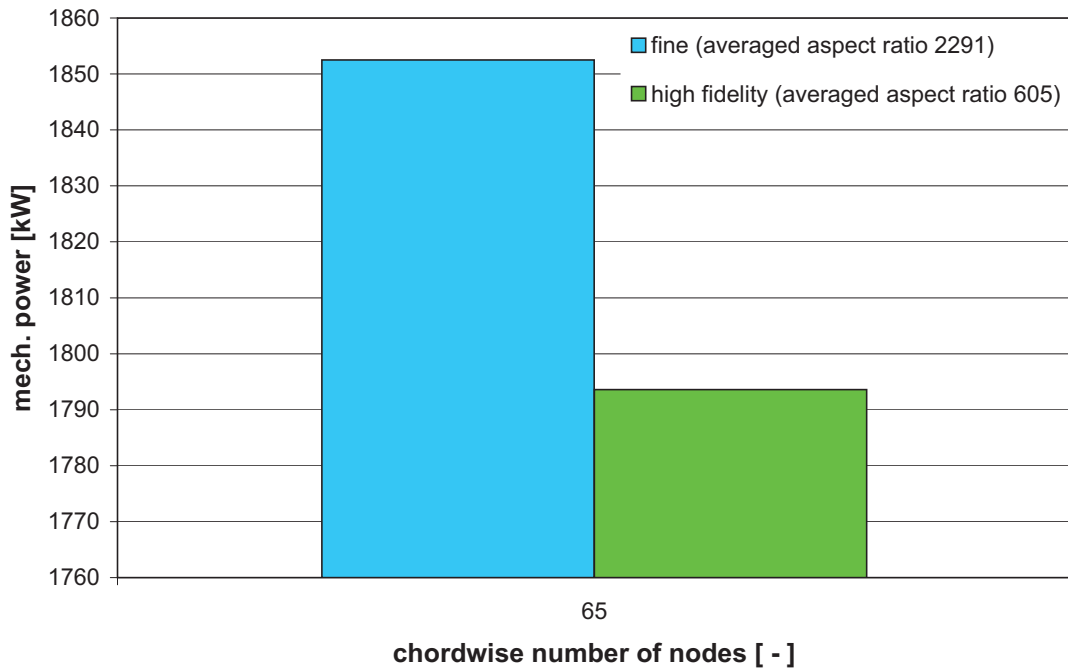


Figure 4.24: The influence of the aspect ratio on the mechanical power

To explain the difference in power the lift and drag coefficient of figure 4.24 at a height of 33.275 meters is evaluated for the results see figure 4.25.

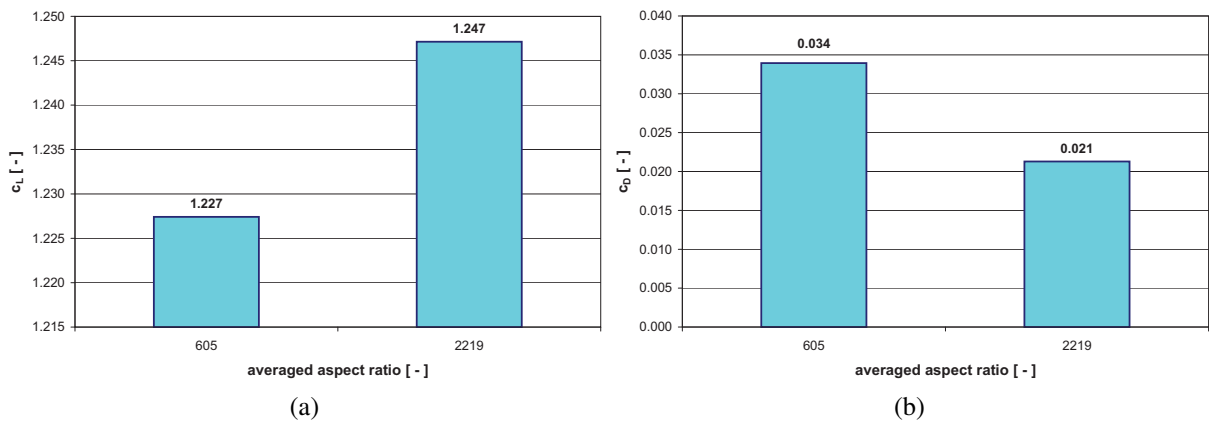


Figure 4.25: The influence of the spanwise refinement, (a) lift coefficient over aspect ratio, (b) drag coefficient over aspect ratio

The lift and drag coefficients over the blade length are also of great interest. In figure 4.26 the coefficients for a different chordwise resolution over the normalized blade length are displayed. It can be clearly seen that, in the transition region (transition region: passage from a circular profile to a well formed airfoil) where the flow is separated, which is caused by the Coriolis force and the oval contour of the airfoil, up to the area of 0.1 normalized blade length a finer chordwise grid resolution is required. The area from 0.2 to 0.4 normalized blade length also needs a finer resolution, as of the big chord lengths of 3.6 meters at 0.2 normalized blade length

and chord lengths of 2.4 meters at 0.4 normalized blade length. The causes of the big chord lengths are shown in figure 4.32.

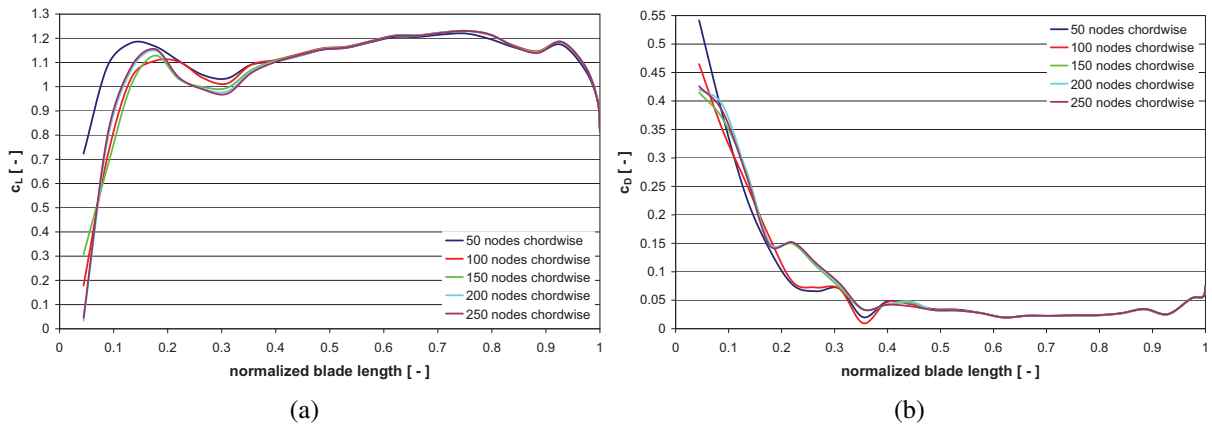


Figure 4.26: The influence of the chordwise refinement over the whole blade, (a) lift coefficient over normalized blade length, (b) drag coefficient over normalized blade length

In order to get a better view of the influence of the chordwise refinement, lift and drag coefficients at different heights were plotted see figure 4.27. The results of the lift and drag coefficient are in correlation with the mechanical power output.

Looking at the 33.275 meters airfoil, between the 250 nodes and the 100 nodes, the averaged drag coefficient have a value of 0.02235 with a deviation of $\pm 0.6\%$. The great deviations at the near hub region lead to the cognition that the refinement should be between 150 and 250 nodes or even higher if computational resources are available.

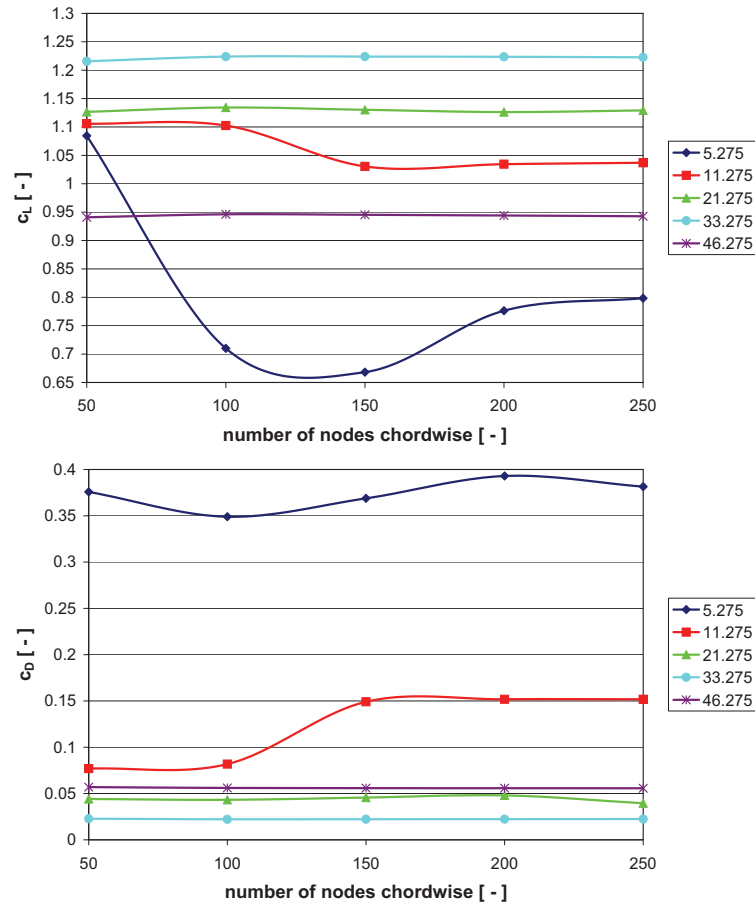


Figure 4.27: The influence of the chordwise refinement, (a) lift coefficient over number of nodes, (b) drag coefficient over number of nodes

Last but not least the plots of the pressure coefficients for the different chordwise resolutions are presented in figure 4.28. The only influence can be seen at the stagnation point region, at the inflow region of the airfoil. The highest differences of the different resolutions are to be found at the suction side, the minus c_p area. The stagnation point is located at the pressure side see figures 4.29 and 4.30, which indicates zero velocity and high pressure. The high gradient in the pressure coefficient at the suction side is caused by the wrong incident flow, which leads to a very high acceleration from the stagnation point on the pressure side to the suction side. The pressure coefficient characteristics on the suction side show an area of high pressure gradient, caused by the circulation from pressure side to suction side. This implies a high acceleration, an area of low pressure gradient from 0.05 to 0.35 normalized chord length with a critical inflection point at the maximum thickness, and an area of a middle pressure gradient from 0.35 to 1 normalized chord length. The inflection points are critical because of the change in pressure gradient, which can lead to transition from laminar to turbulent. Besides decelerating flows have the tendency to separate.

The amplitude on the suction side from 0 to 0.03 normalized chord length, origins in a surface discontinuity which is displayed in figure 4.30 and which was checked and remodeled for the evaluations realized in chapter 4.3.3.2.

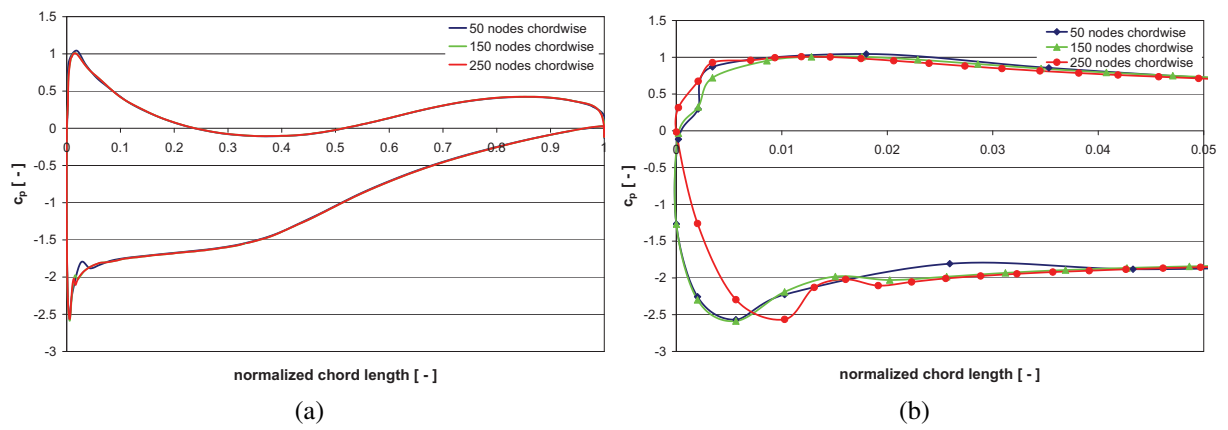


Figure 4.28: The influence of the chordwise refinement at the airfoil at 33.275 meters, (a) pressure coefficient over normalized chord length, (b) zoomed view at the stagnation point region

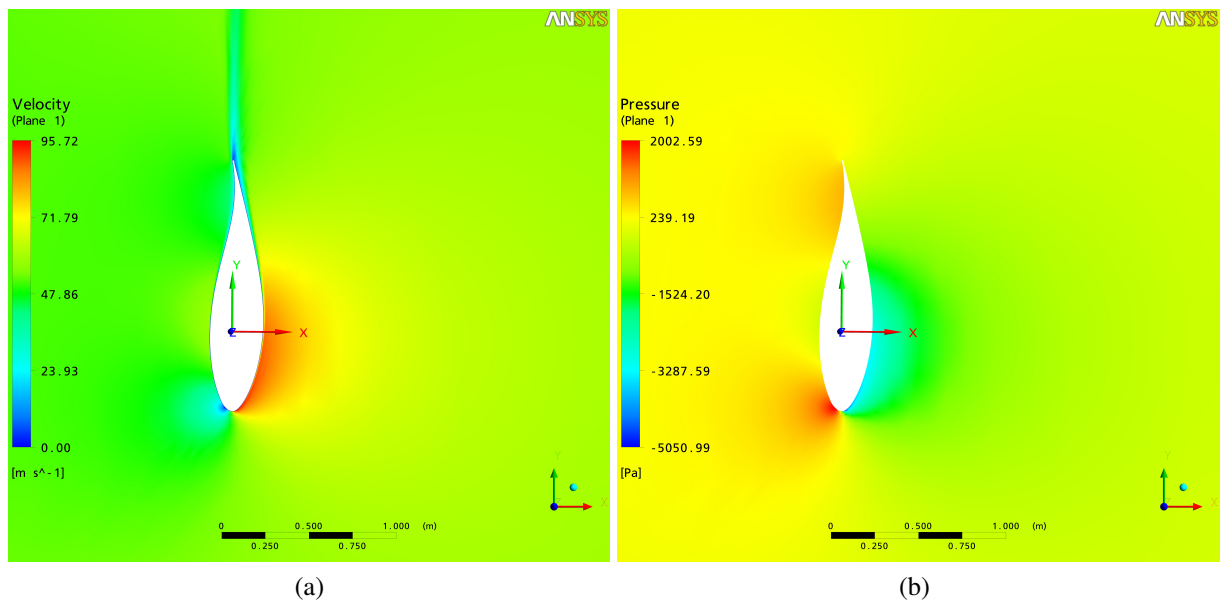


Figure 4.29: Post plots at 33.275 meters to explain the pressure coefficient plot, (a) velocity plot, (b) pressure plot,

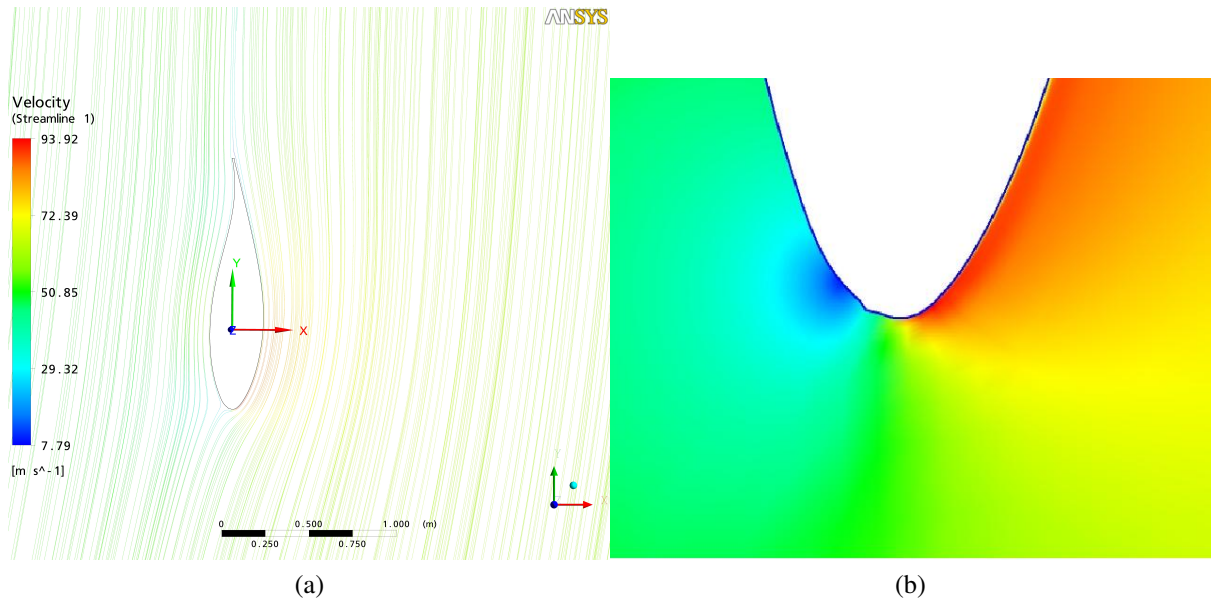


Figure 4.30: Post plots at 33.275 meters to explain the pressure coefficient plot, (a) streamlines plot, (b) surface discontinuity

All these figures show the grid requirement for a realistic simulation. The resolution in spanwise direction has the greatest influence. The truth of the correct result lies in between, the high fidelity result because of its additional refinement in spanwise direction and the usage of a higher number of nodes in chordwise direction.

To sum up the requirements:

- Spanwise refinement (low aspect ratio)
- High number of nodes chordwise (with respect to different airfoil regions)

4.3 Airfoil

In this section Blade WT93 is described together with an evaluation of the simulations which lead to diverse coefficients, forces and angles. Also, a simplified blade design process is presented. To my great pleasure i got the lift and drag coefficients of the simulated blade were provided by the company Windtec. And, last but not least, a detailed view of an airfoil was developed.

4.3.1 Aerodynamics

First, it has to be said that an airfoil is a body to create lift. Especially often used horizontal axis wind turbine airfoils are:

- NACA 63-4xx and NACA 63-6xx series
- NACA 64-4xx
- S8xx series
- FFA W-xxx
- Riso-A1-xxx
- DU xx-W-xxx

As an example of the denotations of an airfoil a sketch is presented in figure 4.31.

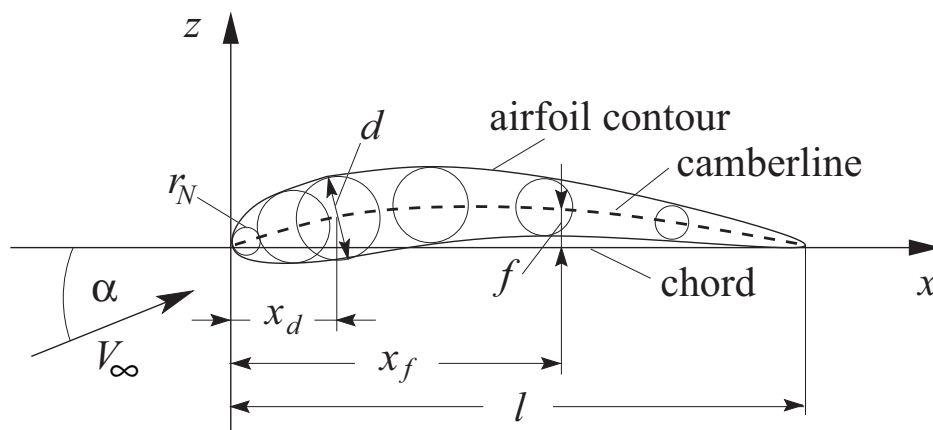


Figure 4.31: Airfoil sketch and nomenclature [18]

The explanation of the airfoil sketch is listed below.

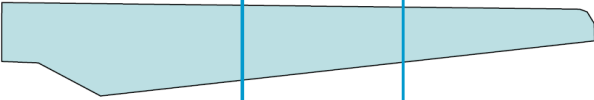
Chord: Connection between leading and trailing points of the camberline.

Camberline: Connects the center of circles drawn into the airfoil shape. Camber f , relative camber f/l , position of maximum camber x_f , relative position of maximum camber x_f/l .

Thickness distribution: Circles around the camber line. Maximum thickness d , relative thickness d/l , position of maximum thickness x_d , relative position of maximum thickness x_d/l .

Nose radius: r_N , relative nose radius r_N/l .

The usage of airfoils depends on their operation purpose. For wind turbine purposes, they are used for power generation by means of a turbine. The design targets for a wind turbine blade are summarized in figure 4.32.



Thickness-to-chord ratio	> .28	.28 - .21	.21 >
High maximum lift-to-drag ratio	●	●●	●●●
Low max. and benign post stall			●●
Insensitivity to roughness	●	●●	●●●
Low noise		●	●●●
Geometric compatibility	●●	●●	●●
Structural demands	●●●	●●	●

Figure 4.32: Design targets for a HAWT blade [14]

It is proved that a total HAWT blade has to fulfill a lot of requirements. In figure 4.33 an airfoil under flow conditions is displayed.

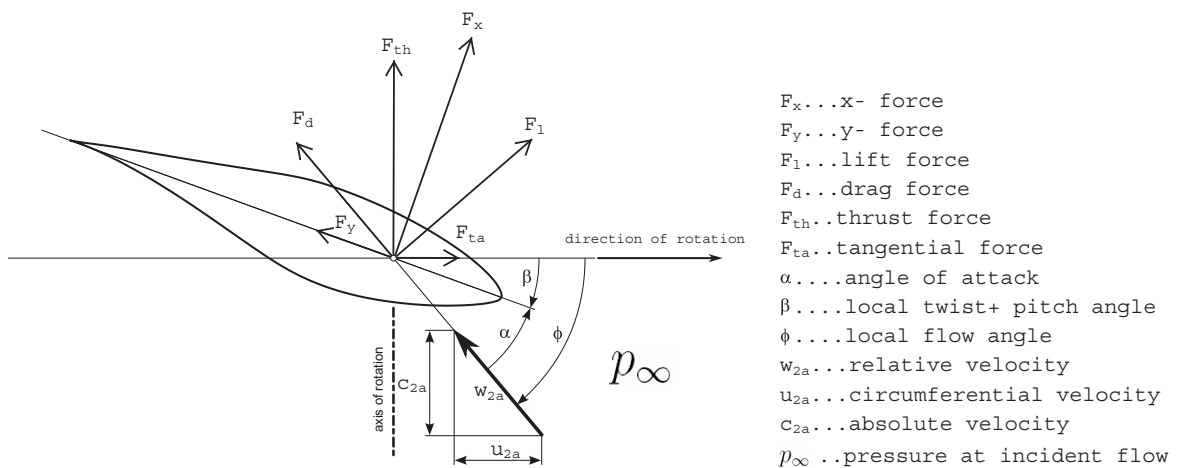


Figure 4.33: Notation of the force situation at an airfoil (based on [27])

The aerodynamic coefficients are described by the following equations:

$$c_l = \frac{F_1}{\rho/2 \cdot c^2 \cdot l_c} \tag{4.12}$$

$$c_d = \frac{F_d}{\rho/2 \cdot c^2 \cdot l_c} \quad (4.13)$$

$$c_p = \frac{P - P_\infty}{\rho/2 \cdot c^2} \quad (4.14)$$

$$c_f = \frac{\tau_w}{\rho/2 \cdot c^2} \quad (4.15)$$

4.3.1.1 Simplified Blade Design Process

To begin with, it must be mentioned that the power is taken out of the wind, by means of a velocity change caused by the airfoil. The undisturbed axial approaching flow is flowing off behind the blade with counter twist and decelerated axial velocity.

Euler's turbine fundamental equation 4.16 describes the power added to or removed from the flow.

The equations used and figures 4.34 and 4.36 are based on [15].

$$Y = H_u \cdot g = H \cdot \eta_u \cdot g = \pm(u_1 \cdot c_{1u} - u_2 \cdot c_{2u}) \quad (4.16)$$

For an axial machine, the specific blade work is presented in figure 4.34.

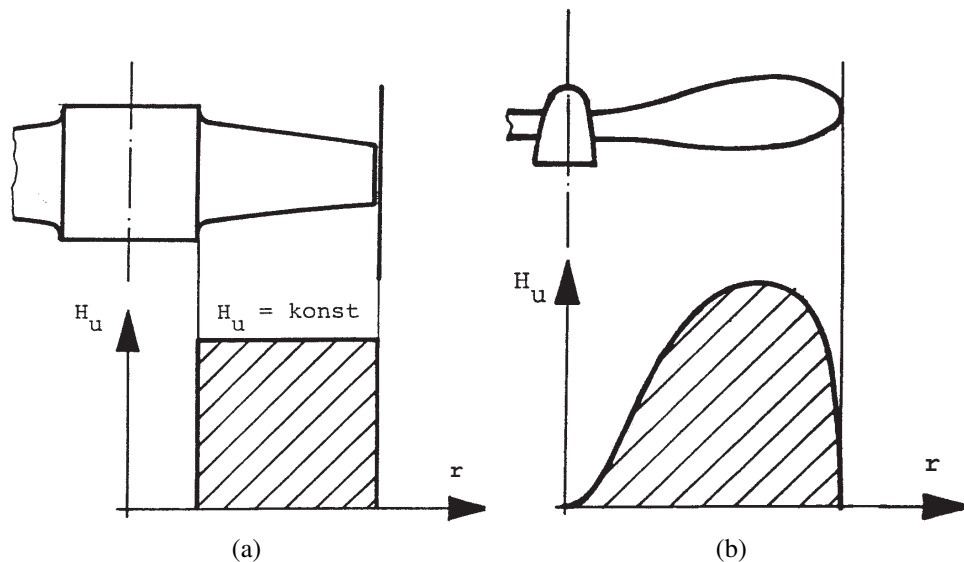


Figure 4.34: Sketch of the specific blade work over radius, (a) a shrouded machine with a constant H_u , (b) a non-shrouded machine with a variable H_u over the radius

A sketch of the streamtube is displayed in figure 4.35, showing the widening of the streamtube because of the continuity equation as well as the static pressure and the axial velocity distribution over the length.

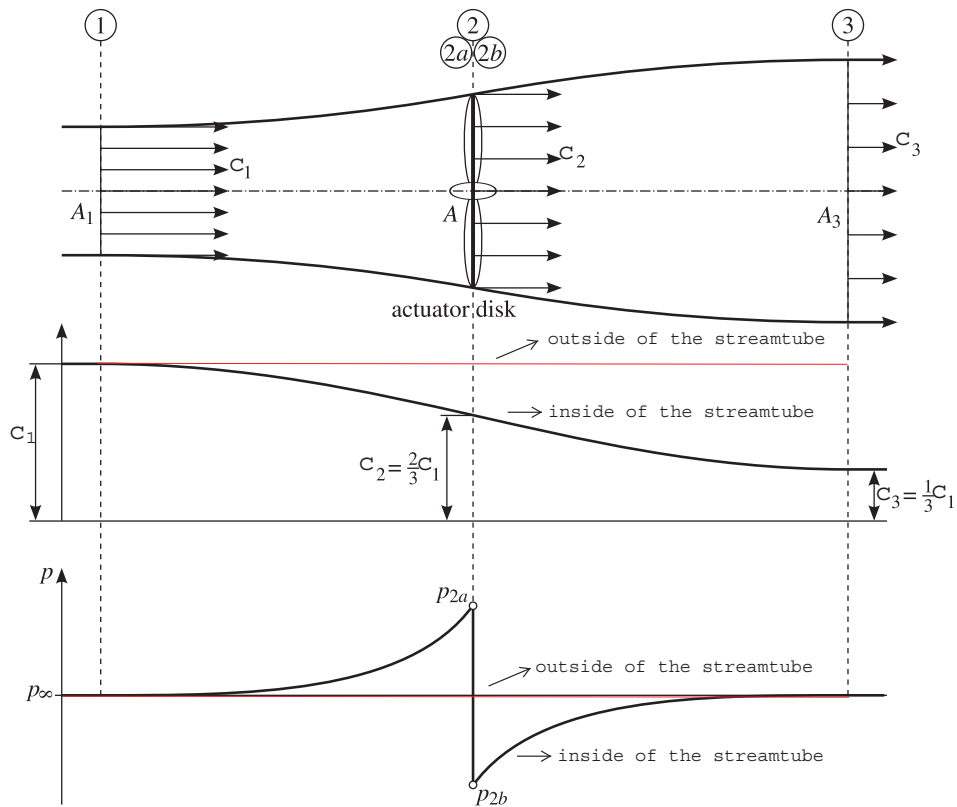


Figure 4.35: Slip stream streamtube with static pressure and axial velocity distribution (based on [27])

Future on a one-dimensional design process of an axial turbine blade is presented.

The existing energy high is the existing energy high difference between the inlet plane 1 and the outlet plane 3. With the Bernoulli equation, static pressure is the same in both planes and the geodetic high is negligible. The equation 4.17 shows the energy high between 1 and 3 (planes of figure 4.35).

$$H = \frac{c_1^2 - c_{3m}^2}{2 \cdot g} \quad (4.17)$$

With the reduced axial velocities mentioned in subsec 4.1.1 velocities are well known. Euler's turbine fundamental equation is simplified to equation 4.18 by means of the same circumferential component (axial machine).

$$H \cdot \eta_u = \frac{1}{g} \cdot u \cdot (c_{u2a} - c_{u2b}) \quad (4.18)$$

With the condition of a twist-free incoming flow at blade inlet **2a** equation 4.18 becomes equation 4.19.

$$H \cdot \eta_u = \frac{1}{g} \cdot u \cdot -c_{u2b} \quad (4.19)$$

The η_u equation 4.20 becomes equation 4.21 with the simplifications of no airfoil drag and in case the flow from 1 to 2a and from 2b to 3 is lossless.

$$\eta_u = 1 - \frac{h_v}{H} \quad (4.20)$$

$$\eta_u = 1 - \frac{c_{u3}^2}{2 \cdot g \cdot H} \quad (4.21)$$

The connection between c_{u3} and c_{u2b} derives from a constant twist between 2b and 3, as well as the ratio of $r_{2b}/r_3 = \sqrt{A_{2b}/A_3}$ and the continuity equation, which see equation 4.22.

$$c_{u3} = c_{u2b} \cdot \sqrt{\frac{c_{3m}}{c_{2bm}}} \quad (4.22)$$

Combined with equation 4.21 and equation 4.22, equation 4.19 becomes the quadratic equation 4.23.

$$c_{u2b}^2 \cdot \frac{c_{m3}}{2 \cdot g \cdot c_{m2b}} - c_{u2b} \cdot \frac{u}{g} - H = 0 \quad (4.23)$$

With the availability of the rotor speed, the circumferential velocity component \mathbf{u} can be determined. The inlet velocity c_1 is determined by the Betz Factor (ideal, loss-free) the $c_{2am} = c_{2bm} = c_1 \cdot \frac{2}{3}$. Then, the relative component w_{2a} is determined. With equation 4.23 the circumferential component of the absolute velocity (c_{u2b}) is determined. Thus, it is possible to draw the velocity triangle, calculated with these equations, see figure 4.36.

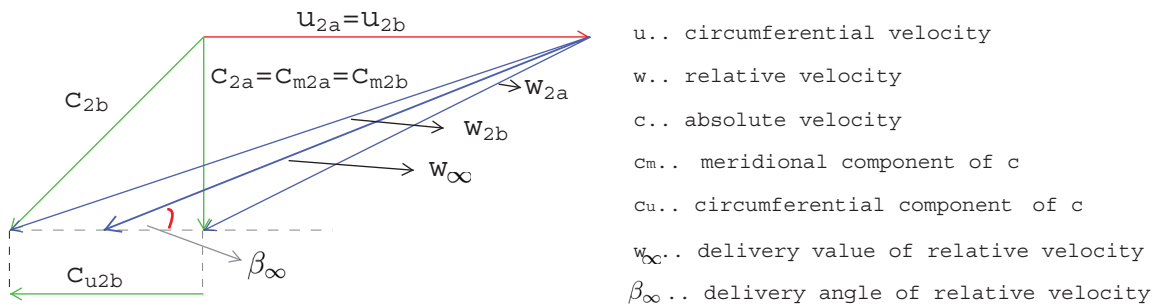


Figure 4.36: Sketch of the velocity triangle of a wind turbine flow at a defined radius

Equation 4.24 shows the delivery velocity w_{∞} for the flow through an axial wing grid with its flow angle β_{∞} in equation 4.25.

$$w_{\infty} = \sqrt{c_{m2a}^2 + \left(u - \frac{1}{2} \cdot c_{u2b}\right)^2} \quad (4.24)$$

$$\tan\beta_{\infty} = \frac{c_{m2a}}{u - \frac{1}{2} \cdot c_{u2b}} \quad (4.25)$$

The power of one blade is described by equation 4.26.

$$\Delta P = \Delta \dot{V} \cdot H_u \cdot \rho \cdot g = \frac{2 \cdot r \cdot \pi \cdot \Delta r}{B} \cdot c_{m2b} \cdot H \cdot \eta_u \cdot \rho \cdot g \quad (4.26)$$

The power of the blade can also be calculated on the basis of $\Delta P = F_{ta} \cdot u$ with equation 4.27.

$$F_{ta} = l_c \cdot \Delta r \cdot \frac{\rho}{2} \cdot w_{\infty}^2 \cdot c_l \cdot \sin(\beta_{\infty}) \quad (4.27)$$

An equalization of ΔP with consideration of the partition $t = 2 \cdot r \cdot \pi / B$ leads to equation 4.28.

$$c_l \cdot \frac{l_c}{t} = \frac{2 \cdot g \cdot H \cdot \eta_u}{w_{\infty} \cdot u} \quad (4.28)$$

Equation 4.28 describes the behavior of an airfoil. With the forced velocities \mathbf{u} and w_{∞} , the airfoil must achieve the ratio of $c_l \cdot \frac{l_c}{t}$ to work off the head with the circumferential efficiency η_u . At this point one can choose the airfoil with the lift coefficient and the associated angle of attack, with a high glide ratio. And with these values, it is then possible to calculate the necessary chord length and the twist angle of the airfoil.

4.3.2 WT93 – Blade Description

The WT93/DF2000 blade of the simulated wind turbine is a blade of 6 different airfoils,– the airfoils are threaded on the pitch axis, and over the radius they have different chord lengths (equation 4.28). The characteristics of the blade is listed in table 4.9. The rows marked green are the source of the pictured airfoils at different heights which see figure 4.37.

Table 4.9: Characteristics of the simulated Blade WT93 [1] (10.2010)

Radius	Blade radial position L	Chord length	Twist angle	Twist axis	Relative thickness	Pitch axis	Airfoil section
[m]	[m]	[m]	[deg]	[% chord]	[%]	[% chord]	[-]
1.275	0	2.200	15	25	100.00	50.0	1
3.275	2	2.415	15.03	25	89.87	46.6	1
5.275	4	2.898	14.94	25	70.98	39.8	1
7.275	6	3.377	14.30	25	54.17	34.8	1
9.275	8	3.603	12.72	25	43.19	32.8	1
11.275	10	3.516	10.08	25	37.13	32.3	2
13.275	12	3.257	7.47	25	33.76	32.2	3
15.275	14	2.978	5.89	25	31.30	32.1	3
17.275	16	2.709	4.99	25	29.33	32.0	4
19.275	18	2.467	4.40	25	27.62	32.0	4
21.275	20	2.251	3.91	25	26.17	32.0	4
23.275	22	2.059	3.43	25	24.96	32.0	5
25.275	24	1.889	2.96	25	23.97	32.0	5
27.275	26	1.742	2.50	25	23.17	32.0	5
29.275	28	1.616	2.05	25	22.51	32.0	5
31.275	30	1.511	1.61	25	21.91	32.0	5
33.275	32	1.426	1.18	25	21.26	32.0	5
35.275	34	1.361	0.77	25	20.43	31.8	6
37.275	36	1.304	0.38	25	19.48	31.5	6
39.275	38	1.240	0.01	25	18.63	31.0	6
41.275	40	1.152	-0.31	25	18.08	30.4	6
43.275	42	1.022	-0.56	25	18.02	29.4	6
45.275	44	0.795	-0.38	25	17.98	27.6	6
46.275	45	0.411	0.29	25	18.00	30.3	6
46.475	45.2	0.248	0.71	25	18.00	34.8	6

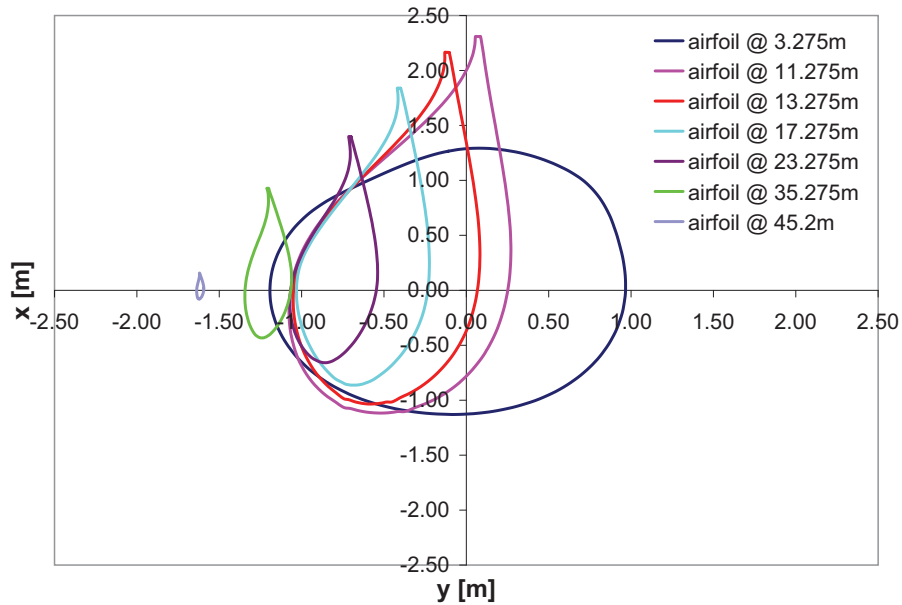


Figure 4.37: Airfoils at specific radii

The pictured airfoils are based on the global Cartesian coordinate system, which is described in chapter 4.2.1. They are created on the basis of the result file of a simulation: through a cut between a plane at a defined radii and the blade surface, and the thus created polyline is exported. The reasons for the choice of a circular airfoil at a radius of 1.275m with the transition to a fine airfoil are:

- mechanical stability and stiffness
- the possibility of pitching

To reach mechanical stability big chord lengths of the airfoils are also required. The different twist angles, which are necessary to fulfill the calculated velocity triangles, are displayed in figure 4.38.

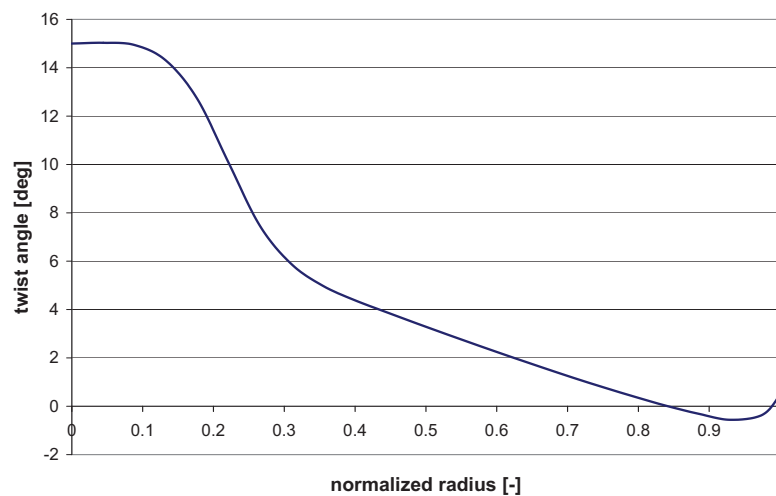


Figure 4.38: Twist angle of the WT93 blade over normalized radii

4.3.2.1 Detailed View of Airfoil on 33.275 [m]

In this chapter a detailed view of airfoil 5, presented in table 4.9 is made (yellow marked). As this airfoil is developed by Technical University of Delft, I asked Mr. Nando Timmer to send the airfoil data to me. The reason of my request was the characteristic s-tail at the trailing edge of the DU developed airfoil.

In figure 4.39, a comparison of the DU-93-W-210 airfoil and the airfoil at 33.275 meters is displayed. It becomes evident, that the 2 airfoils are the same. Number 210 describes the relative thickness (d/l), which is similar to the value of 21 percent (d/l) in table 4.9 at a radius of 33.275m.

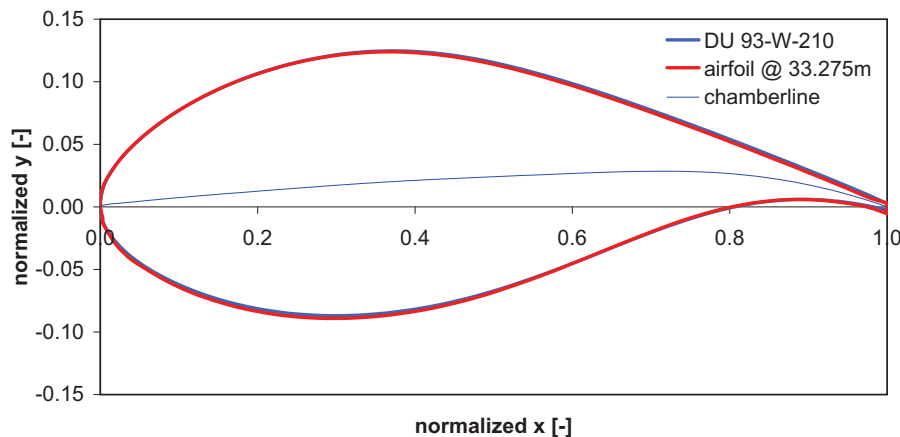


Figure 4.39: A comparison of the DU-93-W-210 airfoil, with the airfoil at 33.275m height

The other used airfoils of the WT93 blade, see airfoil section 5 (table 4.9) have different relative thicknesses,– and the other airfoil sections presented a different airfoil.

Airfoils for HAWTs are designed for a operation at low angles of attack,– in this region the lift coefficients are high and the drag coefficients are quite low. The herein examined DU-93-W-210 airfoil is a laminar airfoil as displayed in figure 4.40, whereas the NACA 4415 airfoil is a normal one, and the green line represent the NACA 65₃ - 418 airfoil which is a laminar airfoil. The DU-93-W-210 line shows the same trend like the NACA 65₃ - 418 line. The values of both NACA profiles are assumed out of [16]. The trend of the laminar airfoils is of great interest, because the operational point of the DU-93-W-210 profile at the WT93 blade is at a Reynolds number of nearly 6×10^6 . But the measured values of TU Delft are only up to 3×10^6 . The NACA 65₃ - 418 profile shows a size of **0.0048** of the c_d at $Re = 6 \times 10^6$. This tendency compared with the DU-93-W-210 profile leads to lower c_d values at high Reynolds numbers ($Re = \frac{\text{Inertial Force}}{\text{Viscous Force}}$).

The big advantage of laminar profiles is the low drag, which is caused by the fact that this profile moves the transition point in direction of the trailing edge. The transition point is in the boundary layer and describes the point where the laminar flow with low wall friction is changed to a turbulent flow with high wall friction. Generally, this transition from laminar to turbulent appears, when the fluid flow streams against an increased static pressure. At a profile this happens on the suction side when the pressure minimum is reached. Normally, this positive characteristic of a laminar profile is given by a big thickness distribution. The maximum

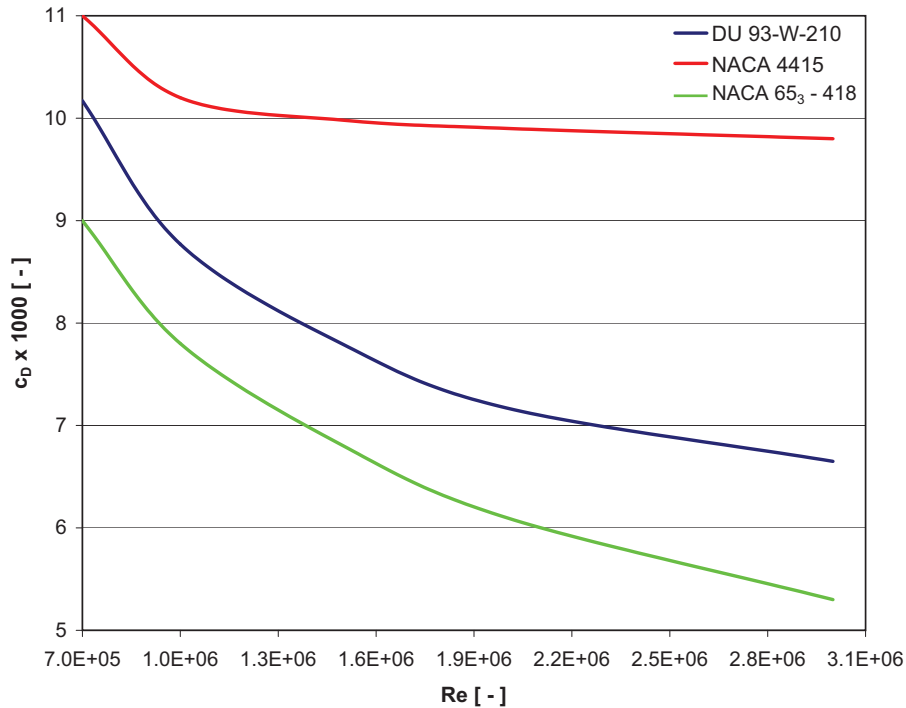


Figure 4.40: A comparison of the DU-93-W-210 airfoil with 2 NACA profiles the NACA 65₃ - 418 profile is a laminar one

thickness is located at 40 to 60 percent of the chord, in comparison to normal profiles where it is located at 20 to 30 percent of the chord. It has to be kept in mind, that the DU-93-WT-210 has the maximum thickness located at 21 percent, but a c_d behavior like a laminar profile. A disadvantage of conventional laminar profiles is the sensitivity to, pollution, dear drops and geometrical modifications. But, in the presentation of Nando Timmer [14] a simulation with roughness consideration of a DU 91-W2-250 airfoil is done,– and it shows a quite better behavior with roughness than the NACA 63-425 airfoil. Roughness leads to lower lift and higher drag coefficients.

The following tables 4.42 and 4.41 show the measured lift and drag coefficients over the angle of attack of the DU-93-W-210 airfoil for $Re = 1 \times 10^6$ and 3×10^6 .

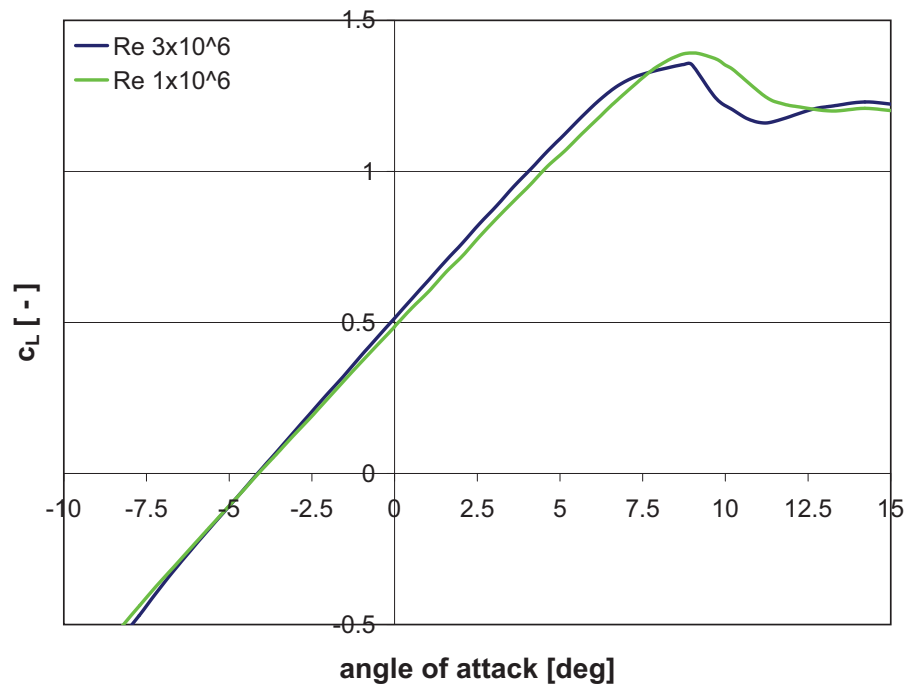


Figure 4.41: The measured lift coefficient over the angle of attack, for DU-93-W-210

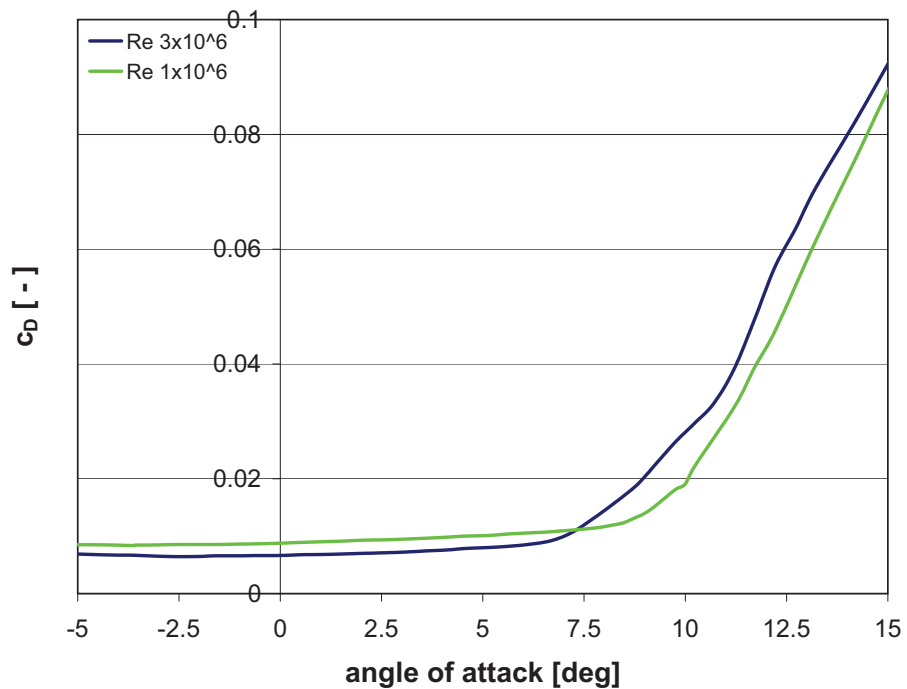


Figure 4.42: The measured drag coefficient over the angle of attack, for DU-93-W-210

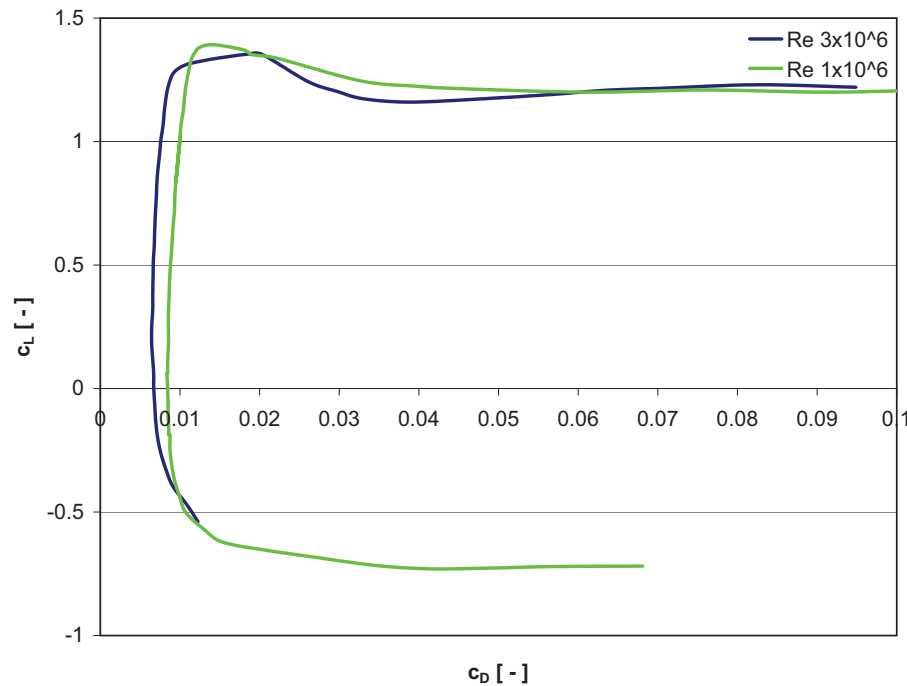


Figure 4.43: Measured airfoil polar, for DU-93-W-210

The airfoil behavior can be divided into three categories of flow regimes [17]:

- The attached flow regime (according to the potential theory)
- The high lift/stall development regime
- Flat plate/fully stalled regime

The attached flow regime: *At low angles of attack (up to 7 degrees for the DU-93-W-210 airfoil), the flow is attached to the upper surface of the airfoil. In this attached flow regime, lift increases with the angle of attack and drag is relatively low. [17] This is a linear gradient as shown in equation 4.29 [18]:*

$$c_l = \frac{dc_l}{d\alpha} \cdot (\alpha - \alpha_0) \quad (4.29)$$

The high lift/stall development regime: *In this regime (from 7 to 11 degrees for the DU-93-W-210 airfoil), the lift coefficient peaks as the airfoil becomes increasingly stalled. Stall occurs when the angle of attack exceeds a certain critical value (high angle of attack, and depending on the Reynolds number) and separation of the boundary layer on the suction side takes place. This causes a wake formed above the airfoil, which reduces lift and increases drag. This condition can occur at certain blade locations or conditions of wind turbine operation. It is sometimes used to limit wind turbine power in high winds. For example, many wind turbine designs using fixed pitch blades rely on power regulation control via aerodynamic stall of the blades. That is, as wind speed increases, stall progresses outboard along the span of the blade (toward the tip), causing decreased lift and increased drag. In a well-designed, stall regulated machine, this results in nearly constant power output as wind speed increases above a certain*

value. [17]

Flat plate/fully stalled regime: At larger angles of attack up to 90 degrees, the airfoil acts increasingly like a simple flat plate with a nearly equal lift and drag coefficient at an angle of attack of 45 degree and a zero lift value at 90 degree. [17]

Also, the developing of the drag coefficient is worth to be looked at. As displayed in figure 4.42, the horizontal region describes the attached flow, whereas with higher angles of attack the flow gets separated. The drag coefficient consists of a pressure and a friction fraction. The wall friction drag dominates for attached flows. The boundary layer effects on the airfoil coefficients are displayed in figure 4.44. An example for behavior is presented in table 4.45. It is indicated, that the skin friction coefficient gets lower with higher angles of attack.

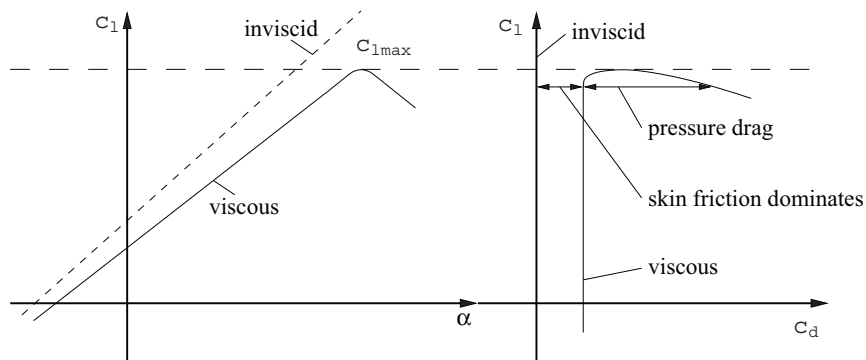


Figure 4.44: Influence of the viscous effects for an airfoil [19]

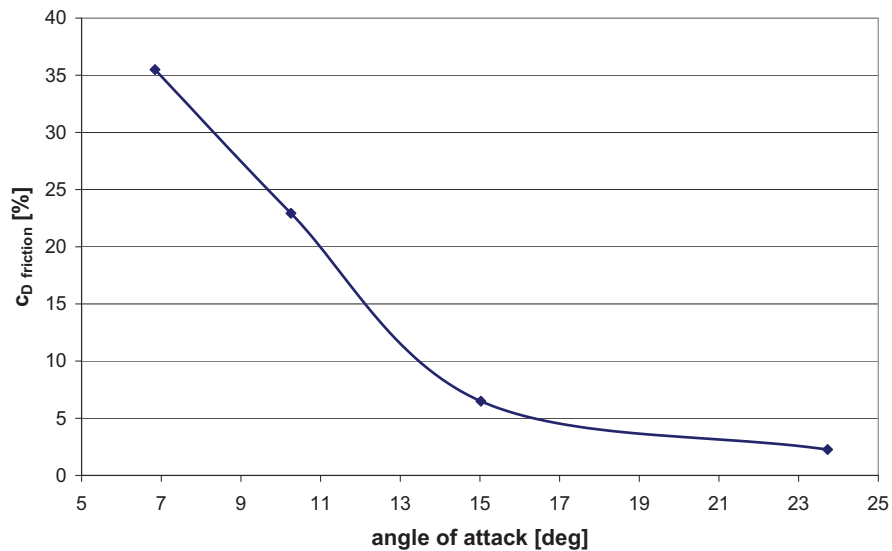


Figure 4.45: Influence of the angle of attack on the skin friction coefficient for the DU-93-WT-210 (results from simulation)

For the airfoil at a height of 33.275 [m] the laminar turbulent transition was calculated with JavaFoil. **The transition** which is drawn in the airfoil contour see figure 4.46 was calculated

with a 2D airfoil simulation program, with an angle of attack of 6 degrees and a Reynolds number of 6×10^6 . Due to the fact, that a detailed transition simulation of the WT93 blade with ANSYS CFX, would blow up this diploma thesis, it was disclaimed. However, in a few literary sources a better correlation of the profile coefficients with the experiment, when using the additional transition model is mentioned.

JavaFoil is a relatively simple program, which uses several traditional methods for airfoil analysis. The following two methods build the backbone of the program:

The potential flow analysis is done with a higher order panel method (linear varying vorticity distribution). Taking a set of airfoil coordinates, it calculates the local, inviscid flow velocity along the surface of the airfoil for any desired angle of attack.

The boundary layer analysis module steps along the upper and the lower surfaces of the airfoil, starting at the stagnation point. It solves a set of differential equations to find the various boundary layer parameters. It is a so-called integral method. The equations and criteria for transition and separation are based on the procedures described by Eppler. Compared with CalcFoil, this module has been completely rewritten and cleaned up. [20]

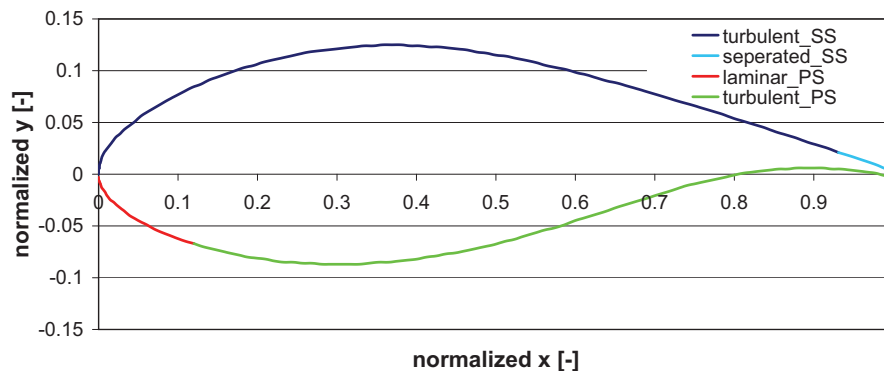


Figure 4.46: The transition point located at the airfoil at 33.275m

The description of the flow over an airfoil, with the development of the boundary layer and with separation, is explained in figure 4.47.

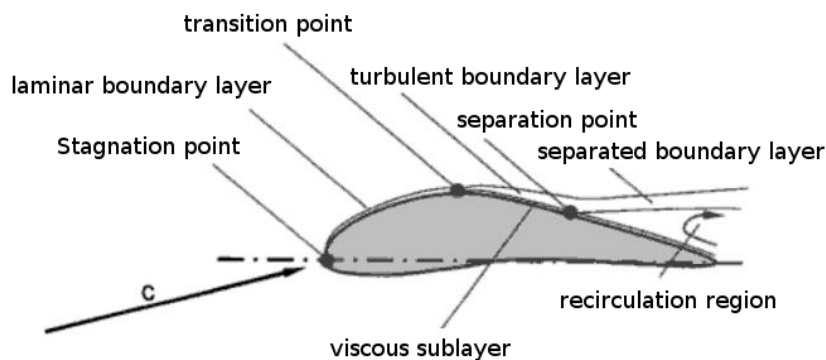


Figure 4.47: Sketch of the flow over an airfoil, with transition and separation [12]

4.3.3 Interpretation of the Results

The results of the simulation can be evaluated in the way, presented in figure 4.48.

$z = 39.275\text{m}$

chord = 1.24m

lift force= 3764 N

drag force= 55 N

thrust force = 3746 N

tangential force= 350 N

angle of attack = 5.37 deg

$Re = 6.1 \times 10^6$

glide ratio = 68.7

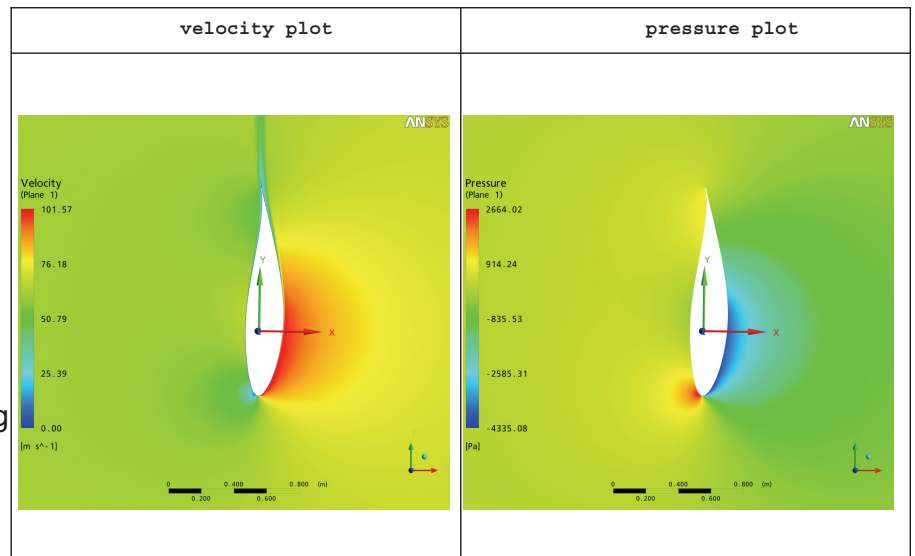


Figure 4.48: Calculated values with velocity and pressure plot at 39.275 meters

4.3.3.1 Reduced axial Velocity Method (Rav Method)

The local angle of attack of an airfoil is defined by the angle between the relative velocity direction and the chord line. The problem is that the definition of the angle of attack is important to determine the lift and drag coefficients. The technique used is the so-called averaging technique applied by Hansen et. al. ([22]), Johansen and Sorensen ([23]) and Hansen and Johansen ([24]).

The method is a way to determine the actual inflow velocity taking into account the decrease in axial flow due to the presence of the blade. The annular averaged axial velocity at a specific radial position under consideration was determined by a surface of revolution parallel to the rotor, whereas this surface of revolution was swept from upstream to downstream in axial direction, see figure 4.49. The surface of revolution was created over the radius with a different angle to get nearly the same area at every radii,– thus smooth the calculated area averaged velocity.

The results of the application of this method for a height of 33.275 [m] are displayed in figure 4.50, whereas the red line symbolizes the biggest x-distance of the airfoil at 33.275 meters. (Note: the y coordinate shows into the direction of the chord line) This value was calculated for all radii of the blade, see table 4.9. The calculated value is the axial velocity (= absolute velocity).

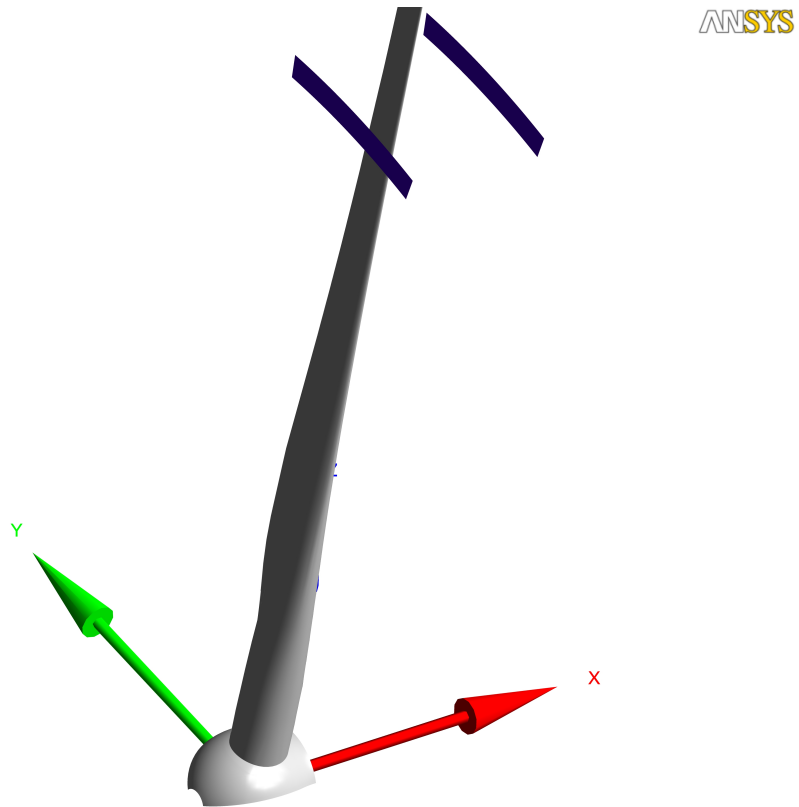


Figure 4.49: View at the axial velocity method in ANSYS CFX Post, 2 surfaces of revolution are presented

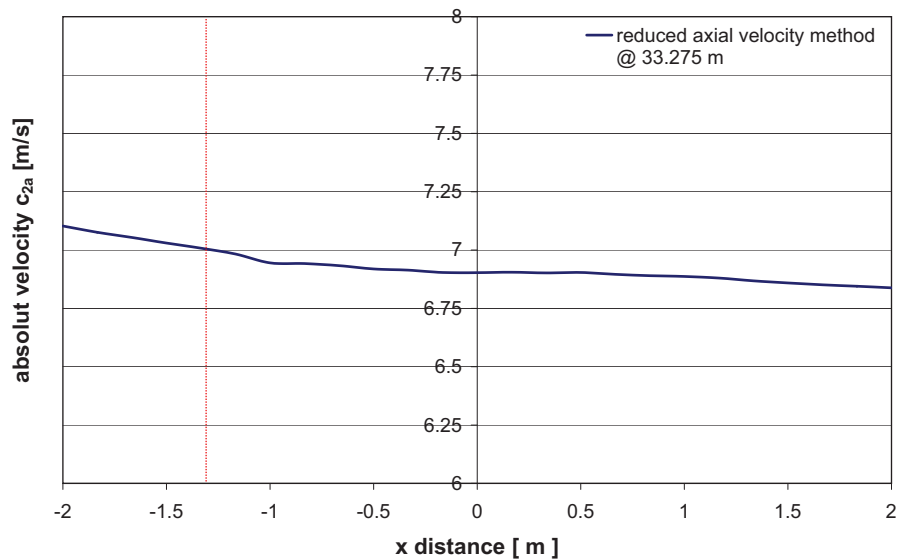


Figure 4.50: The plotted absolute velocity over the x distance at 33.275 meters height

In figure 4.33 the different angles are displayed. With equations 4.30, 4.31 and 4.32 the axial induction factor and the local angle of attack can be calculated. The result of these calculations is displayed in figure 4.53.

$$a = \frac{c_1 - c_{2a}}{c_1} \quad (4.30)$$

$$\phi = \arctan \cdot \frac{(1 - a) \cdot c_1}{(1 + \hat{a}) \cdot u_{2a}} \quad (4.31)$$

$$\alpha = \phi - \beta \quad (4.32)$$

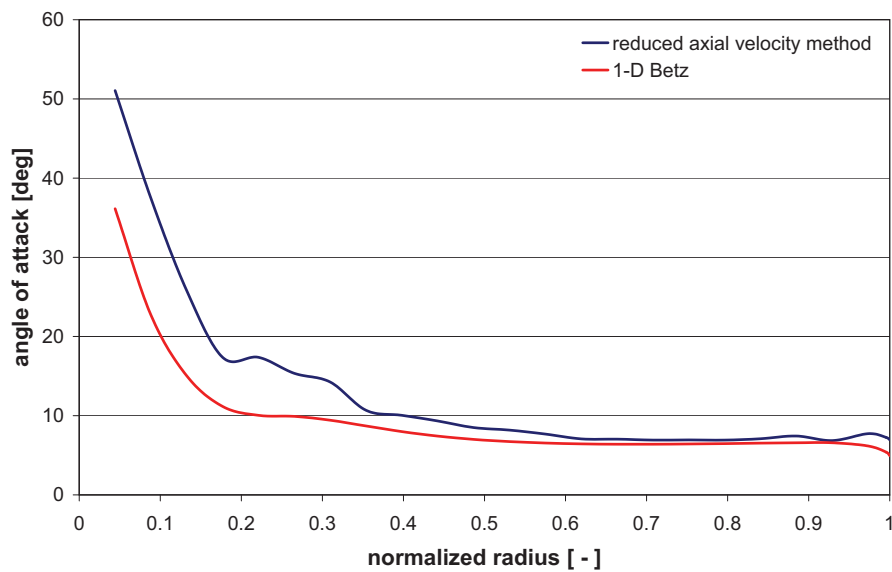


Figure 4.51: The differences between the Rav method and the 1D idealized Betz method is compared, the angle of attack over the normalized radius is displayed

The forces necessary for calculating the coefficients were exported from ANSYS CFX Post. This procedure was chosen, to create a plane, to intersect the rotor wall and to create a polyline on the intersection and the wall. With the twist and the pitch angle it was possible to create a coordinate frame with the y-axis in direction of the trailing edge, which is the coordinate frame on which the x-force and y-force were based (forces see figure 4.33). Based on the created coordinate frame and the polyline, every calculated physical value could be exported. In this case, it was the normalized force in x and y direction, and with angle α (angle of attack) the forces could be converted into the lift and the drag force. The normalized force is the width force per unit on a line in the direction of a specified axis.

The created coordinate frame for an airfoil is displayed in figure 4.52

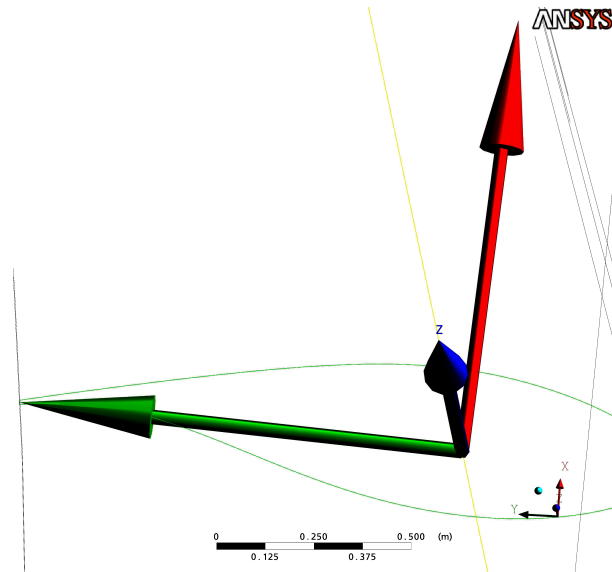


Figure 4.52: Created coordinate frame for an airfoil

4.3.3.2 Comparison of the Results for the Airfoil at 33.275 [m]

In this chapter, the evaluated results of the coefficients of the airfoil at 33.275 meters, which is the DU-93-W210 profile, are compared with numerical simulation evaluations by [25] and measurements at the TU Delft. The numerical simulations for this airfoil were found in [25]. To begin with, it has to be proved that the angle of attack, which is a size dependent on many variables, has great influence on the calculated lift and drag coefficients. The pressure coefficient is the only value to be evaluated directly. The deviation of the different evaluation methods for the drag and lift coefficients is presented in figure 4.53. The influence of the angle of attack on the calculated drag coefficient is relatively high, see figure 4.54. The angle of attack on the DU-93-W-210 airfoil, is **6.396** with the Betz method and **6.927** with the Rav method. Therefore, the evaluated results of the drag coefficient compared to the measured results should be seen critical.

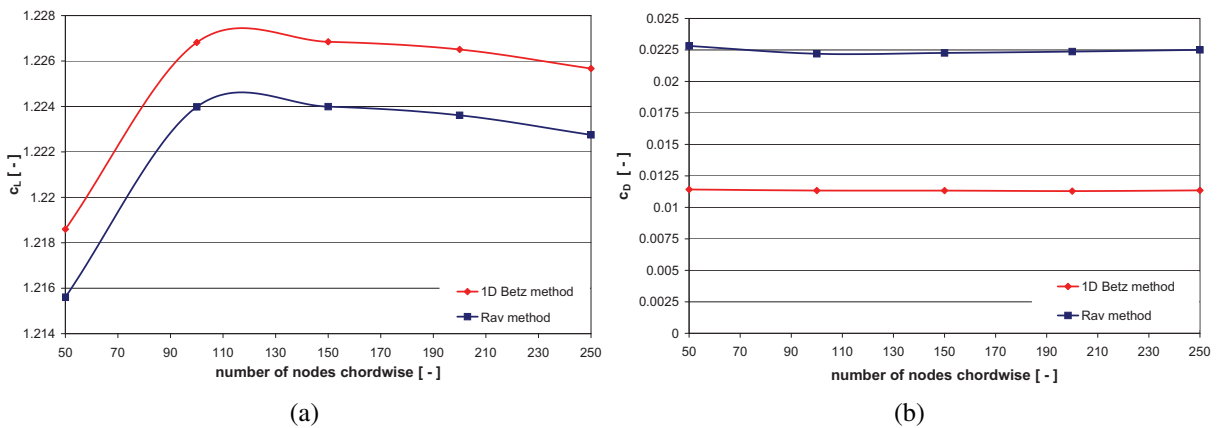


Figure 4.53: In both figures, the differences between the Rav method and the 1D idealized Betz method are compared, (a) shows the lift coefficient over the number of nodes, (b) shows the drag coefficient over the number of nodes

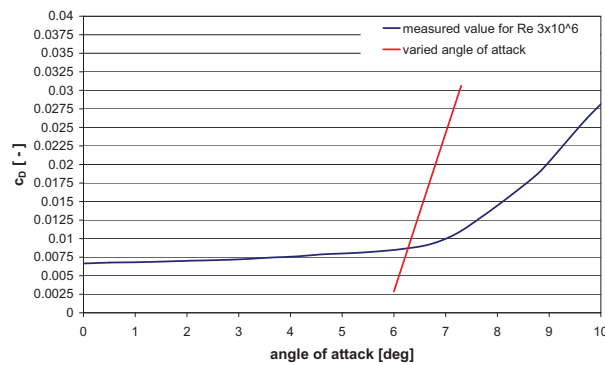


Figure 4.54: Varied angle of attack, based on the Rav method, and influence on the drag coefficient

Generally, many literary sources mention that a 3D fully turbulent simulation over-predicts the drag coefficient. A reason for this is the too fast and too large growth of the turbulent boundary layer. However in reality, mostly a laminar boundary layer is located first. A laminar boundary layer leads to a lower skin friction drag.

This turbulent boundary layer influences the effective airfoil contour. The effective airfoil contour consists of the geometrical airfoil contour plus the boundary layer thickness. The flow over the airfoil must go surround this effective contour and additionally, the stagnation point can be displaced.

Different numerical models (3D DES and 2D RANS) with and without transition taken from [25] are compared with the measurements by the TU DELFT and with the 3D RANS (SST fully turbulent) simulation realized by myself. The differences in drag and lift coefficients are displayed in figures 4.55 and 4.56.

The mesh of the rotor domain used consists of 12 nodes on the leading and trailing edge and 150 nodes in chordwise direction. Furthermore to correct the surface discontinuity shown in figure 4.30, a new surface creation with a subsequent remesh in ICEM CFD was generated.

The variation of the angle of attack was achieved by means of different number of revolutions. This again leads to different velocity triangles. It has to be mentioned, that the variation of the number of revolutions induces different Reynolds numbers. However, the influence of the Reynolds number in the range from 10^6 to 10^7 on the lift and drag coefficient is low. The calculation and evaluation of the angles with the Reynolds number is listed in table 4.10.

Table 4.10: Different number of revolutions with the associated calculated beta infinity (with equation 4.25, the evaluated angle of attack, the Reynolds number and the mechanical power

n	β_∞	α	Reynolds number	mech. power
[min-1]	[deg]	[deg]		[kW]
5	19.267	28.593	2.0E+06	91.373
6	16.535	23.728	2.4E+06	237.504
7	14.440	20.158	2.7E+06	423.110
8	12.794	17.347	3.1E+06	617.763
9	11.472	15.023	3.5E+06	828.438
10	10.391	13.111	3.9E+06	1050.863
11	9.492	11.552	4.2E+06	1267.224
12	8.733	10.255	4.6E+06	1453.678
13	8.084	9.156	5.0E+06	1605.448
14	7.524	8.218	5.4E+06	1734.222
15	7.035	7.389	5.7E+06	1815.683
15.7	6.729	6.843	6.0E+06	1841.228
16	6.606	6.615	6.1E+06	1837.706
17	6.225	5.923	6.5E+06	1837.737
18	5.885	5.330	6.9E+06	1829.349
19	5.581	4.814	7.2E+06	1818.762
20	5.306	4.353	7.6E+06	1799.504
30	3.551	1.386	1.1E+07	454.651
40	2.667	0.258	1.5E+07	-2690.460

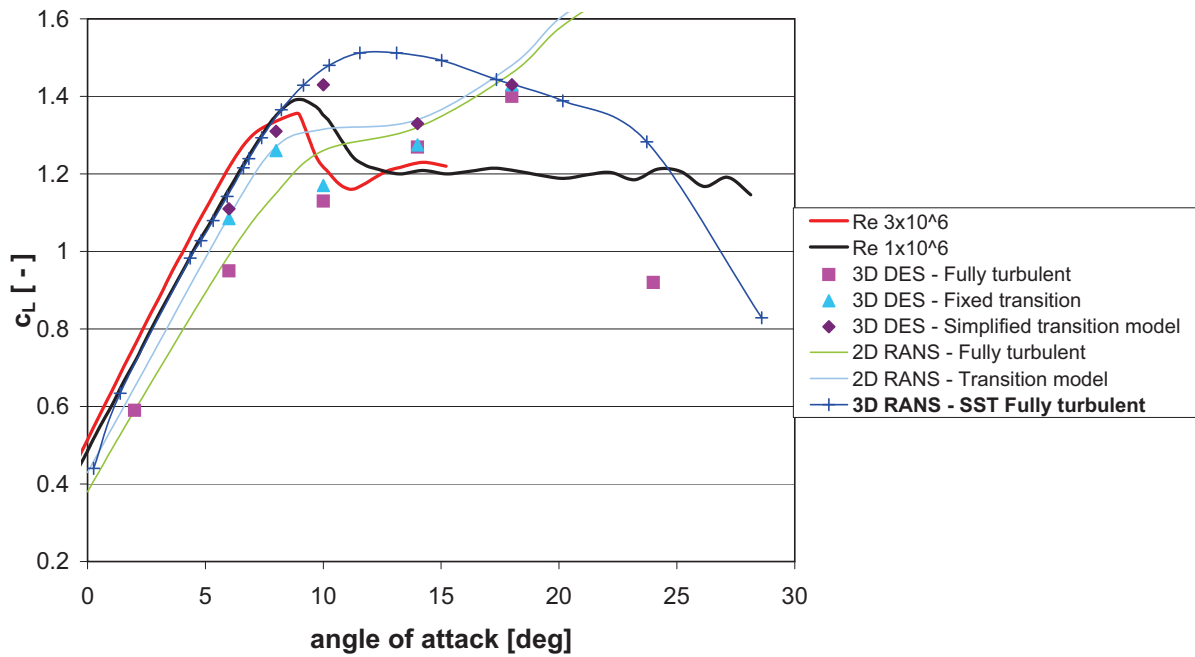


Figure 4.55: The lift coefficient over the angle of attack

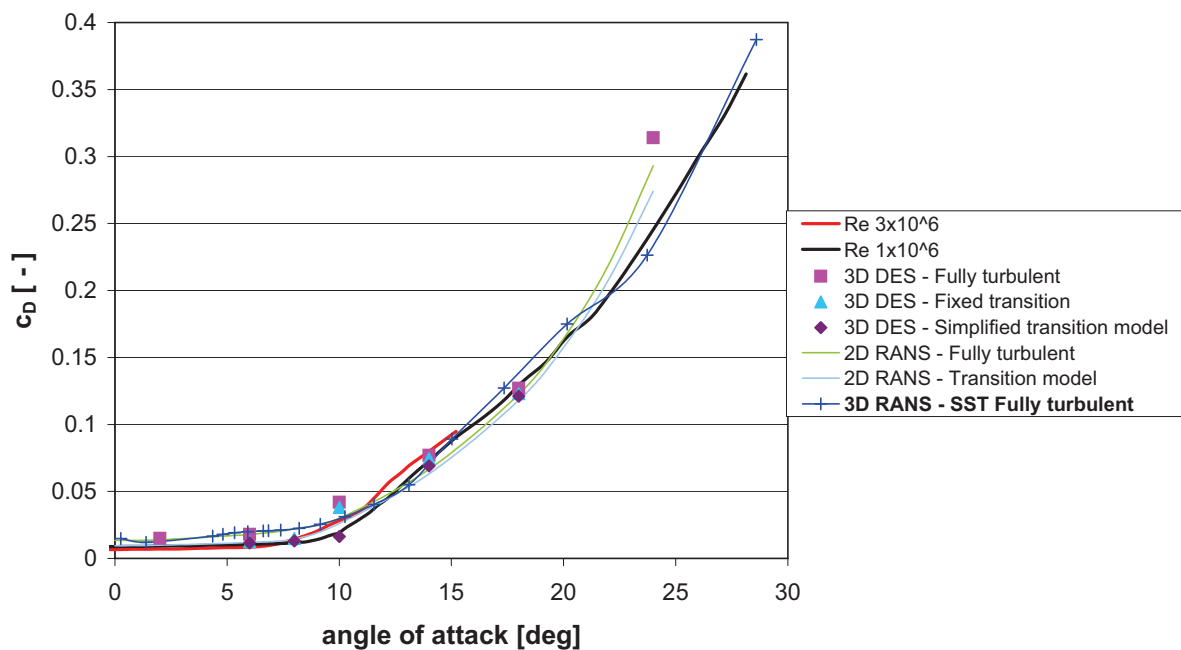


Figure 4.56: The drag coefficient over angle of attack

Attached flow regime:

It can be seen that the **3D RANS SST Fully turbulent simulation** results in a quite low deviation of the lift coefficient. However a high deviation of the drag coefficient is displayed. The reason for this effect is the above mentioned too fast and large growth of the turbulent boundary layer, which can be proved by the skin friction distribution, see figure 4.58. The turbulence model used does not resolve the laminar boundary layer as of a too high y^+ value, see figure

4.66.

At an angle of attack of 6 degree the **3D DES** leads to a high deviation of the lift and drag coefficients, which is caused by the pressure coefficient distribution, see figure 4.57. The closed area of the pressure coefficient distribution is equivalent to the lift force, – in this case the closed area is small with an additional separation near the trailing edge. The skin friction distribution is quite the same as with the 3D RANS SST fully turbulent simulation.

The best results are produced by the **3D DES with transition**, which predict quite good agreement with the experiment, especially with the drag coefficient. This is made visible by the skin friction distribution of the transition models. The skin friction is much lower compared to the other models. The reason for this is a first laminar boundary layer with a transition at a x/chord length of 0.35 and a following turbulent boundary layer. A visualization of the flow over the airfoil is displayed in figure 4.59.

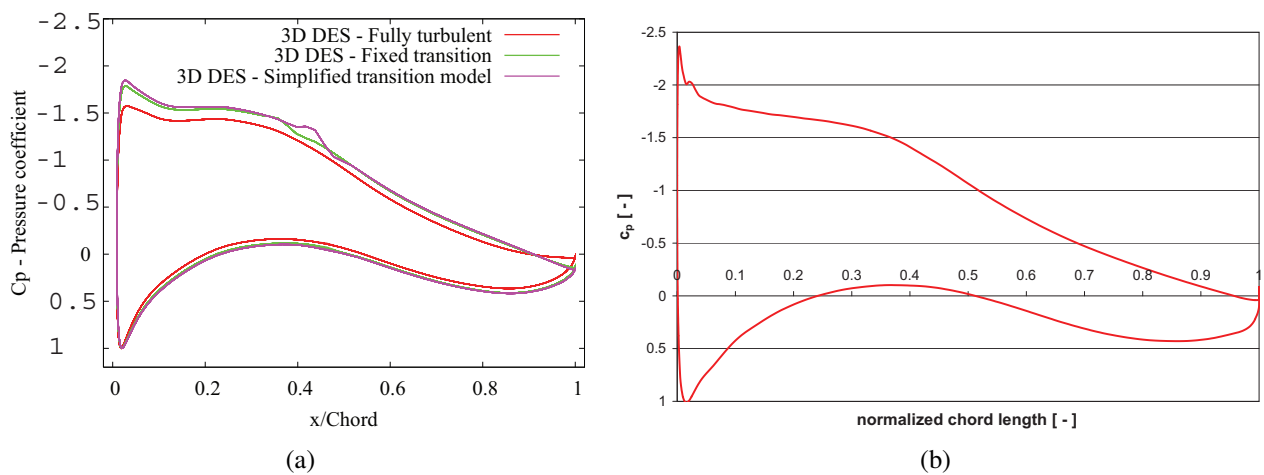


Figure 4.57: (a) shows the pressure coefficient plot at an angle of attack of 6 degrees (based on [25]), (b) pressure coefficient plot at an angle of attack of 6 degrees, 3D RANS SST fully turbulent simulation

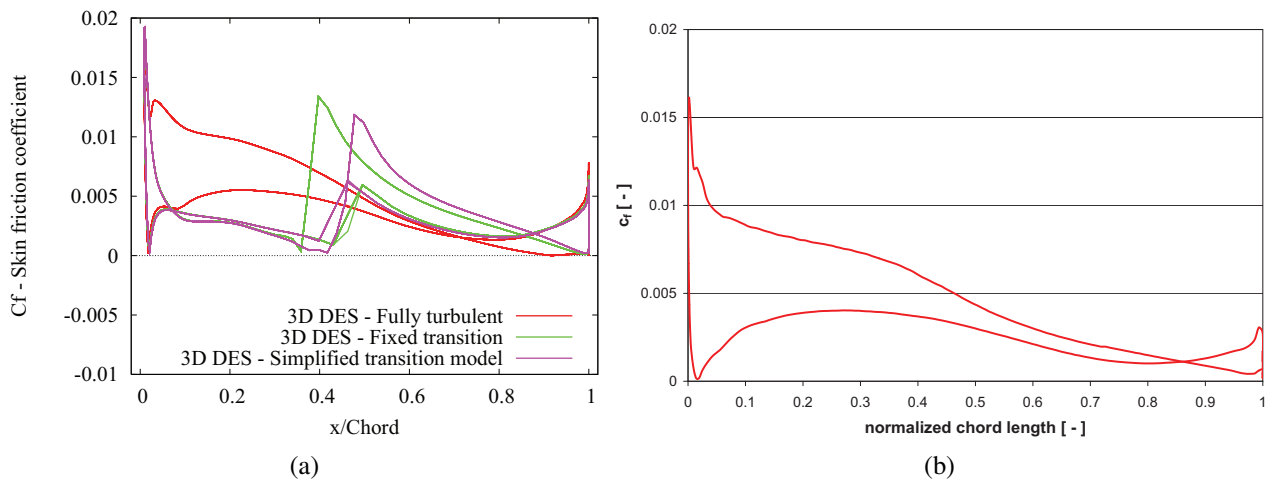


Figure 4.58: (a) skin friction coefficient plot at an angle of attack of 6 degrees (based on [25]), (b) skin friction coefficient plot at an angle of attack of 6 degrees, 3D RANS SST fully turbulent simulation

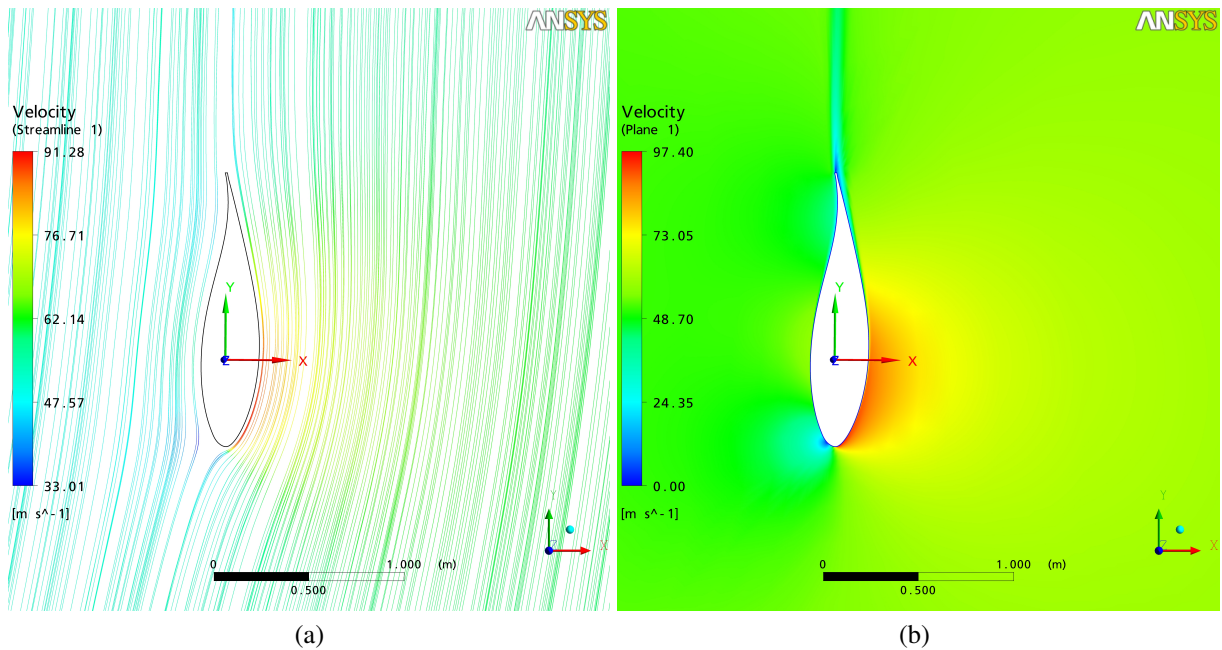


Figure 4.59: 3D simulated flow over the DU-93-WT-210 airfoil at an angle of attack of 6 degrees, (a) 2D view at the surface streamlines of the flow, (b) velocity plot

High lift/stall development regime:

In this area the evaluation is done at an angle of attack of 10 degrees. The **3D DES with fixed transition** predict the lift and drag coefficients accurately. This model also predicts the stall regime which displays a collapse of the lift coefficient. The pressure coefficient distribution shows a large separation area which indicates a loss in lift. And, a large regime of a turbulence boundary layer can be seen in the skin friction distribution.

The model with the nearly same results is the **3D DES**. However this model is not able to predict the stall regime between an angle of attack of 7 to 10 degrees.

The **3D DES with simplified transition** shows nearly the same pressure coefficient distribution like the **3D RANS SST fully turbulent simulation** with no separation area, – which leads to high lift coefficients. The skin friction distribution depicts the absolutely opposite development of the **3D DES with simplified transition** and the **3D RANS SST fully turbulent simulation**, which on the one hand leads to a high drag coefficient for the 3D RANS SST simulation and on the other hand to a low drag coefficient for the 3D DES simulation.

The pressure coefficients and skin friction coefficients at an angle of attack of 10 degrees are presented in figures 4.60 and 4.61. A visualization of the flow over the airfoil is displayed in figure 4.62.

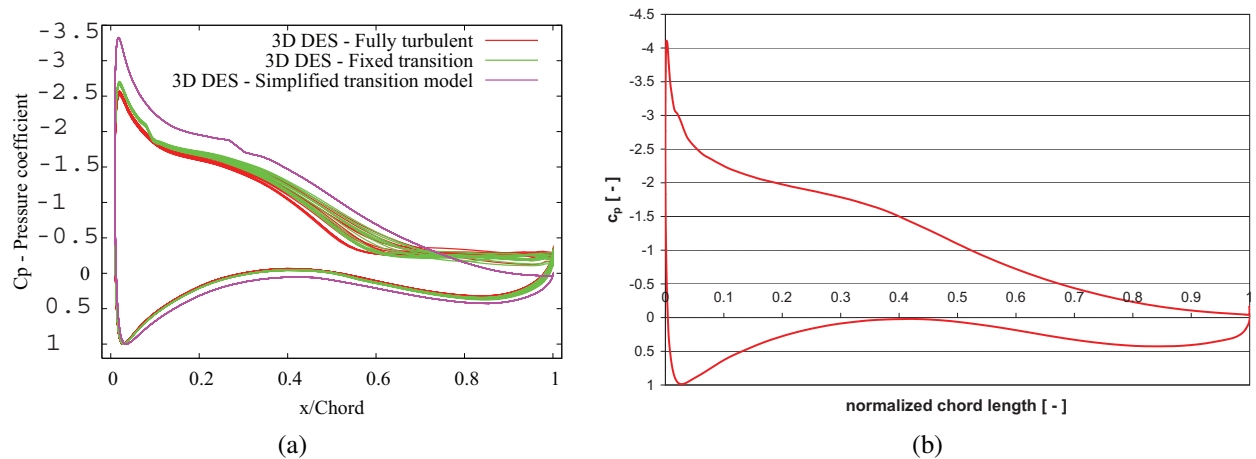


Figure 4.60: (a) pressure coefficient plot at an angle of attack of 10 degrees (based on [25]), (b) pressure coefficient plot at an angle of attack of 10 degrees, 3D RANS SST fully turbulent simulation

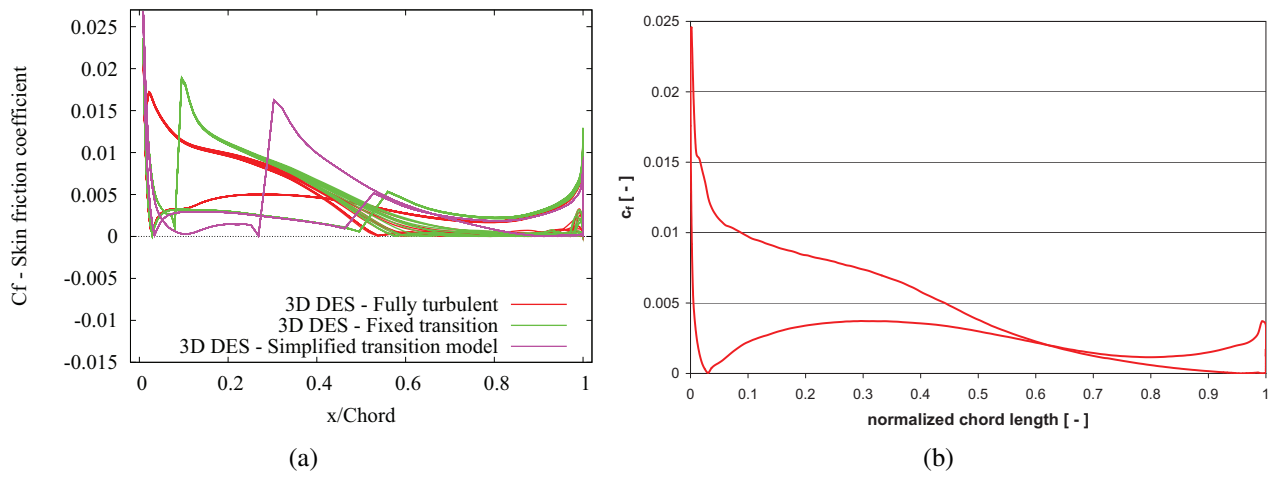


Figure 4.61: (a) skin friction coefficient plot at an angle of attack of 10 degrees (based on [25]), (b) skin friction coefficient plot at an angle of attack of 10 degrees, 3D RANS SST fully turbulent simulation

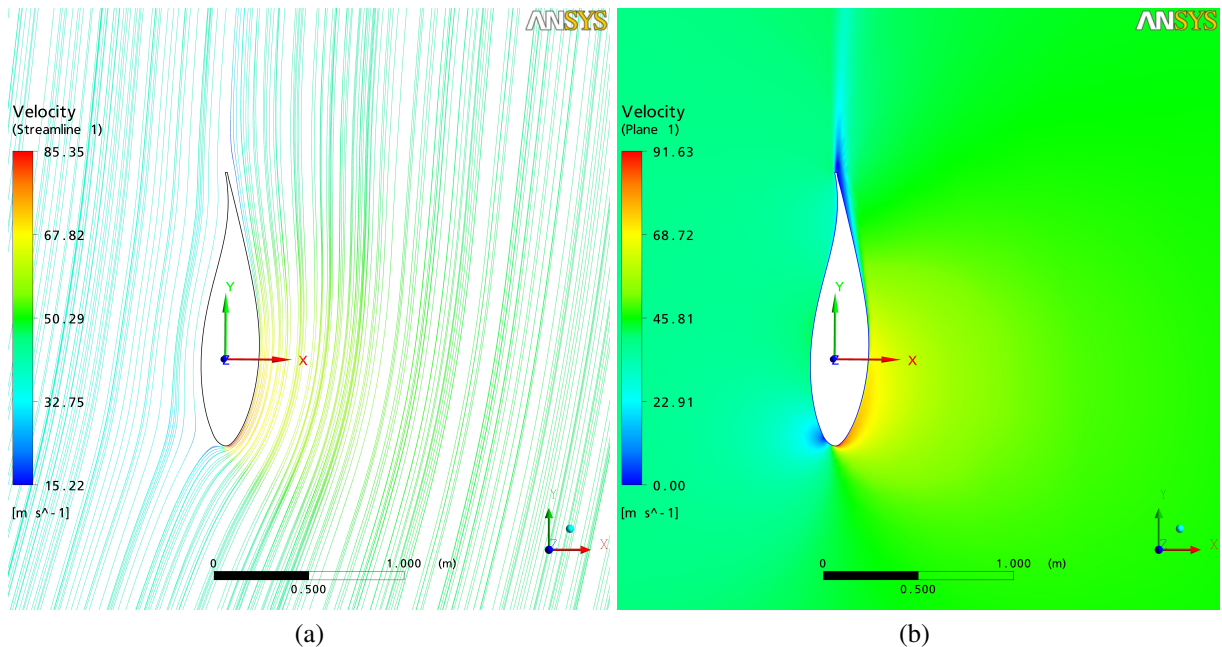


Figure 4.62: 3D simulated flow over the DU-93-WT-210 airfoil at an angle of attack of 10 degrees (a) 2D view of the surface streamlines of the flow, (b) velocity plot

Flat plate/fully stalled regime:

In this flat plate regime the interpretation is done at an angle of attack of 14 degrees.

The pressure coefficients of all models show nearly the same distribution, especially the separation area on the suction side at a x/chord length from 0.5 to 1. Only the **3D RANS SST fully turbulent simulation** distribution is generally too high, which leads to a too high lift coefficient.

The drag coefficient in the flat plate regime is quite well predicted, which originates from the existence of the turbulent boundary layer in the measurement.

The pressure coefficients and skin friction coefficients at an angle of attack of 14 degrees are displayed in figures 4.63 and 4.64. For the visualization of the flow over the airfoil see figure 4.65.

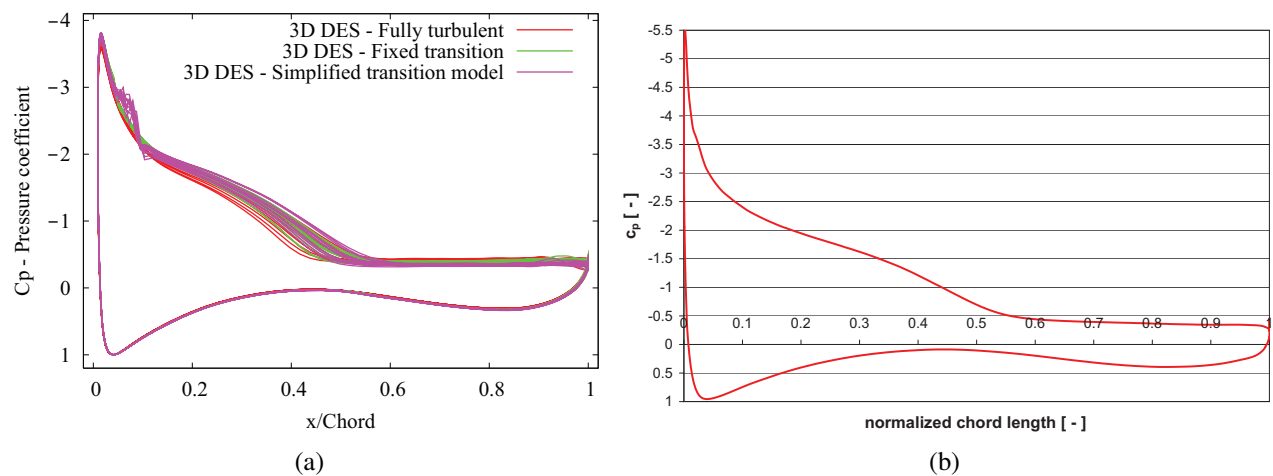


Figure 4.63: (a) pressure coefficient plot at an angle of attack of 14 degrees (based on [25]), (b) pressure coefficient plot at an angle of attack of 14 degrees, 3D RANS SST fully turbulent simulation

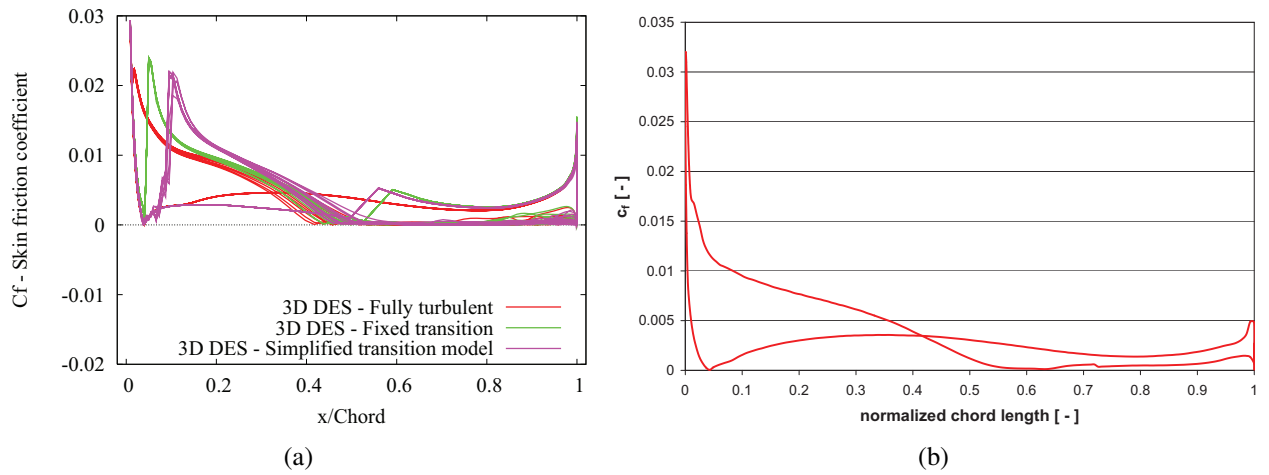


Figure 4.64: (a) skin friction coefficient plot at an angle of attack of 14 degrees (based on [25]), (b) skin friction coefficient plot at an angle of attack of 14 degrees, 3D RANS SST fully turbulent simulation

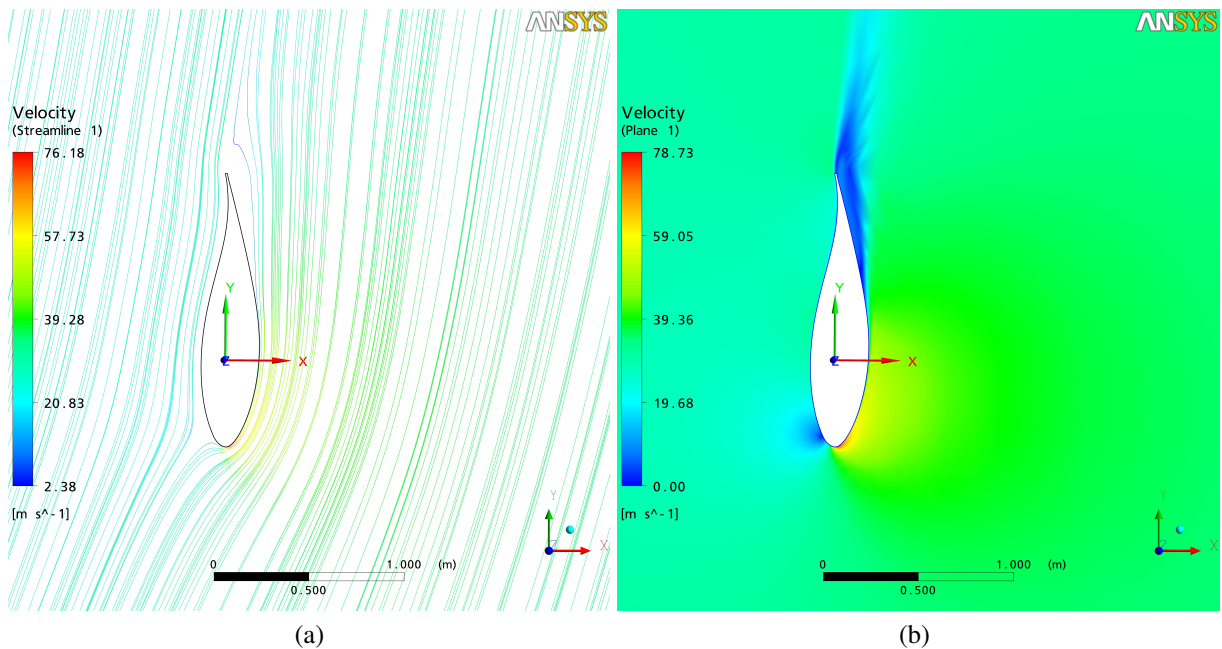


Figure 4.65: 3D simulated flow over the DU-93-WT-210 airfoil at an angle of attack of 14 degrees, (a) 2D view of the surface streamlines of the flow, (b) velocity plot

Generally, it is obvious that for low angles of attack, where the flow is mostly attached, the predicted lift coefficients compare better with the measurement. The reasons for the too high drag coefficients are going to be mentioned later. Opposed to higher angles of attack, where the flow is mostly separated, the coefficients are overpredicted. In the paper "Detached-eddy simulation of a Flow Around the NREL Phase VI Blade" the reasons for these behaviors are explained:

This is primarily caused by two factors. First, the RANS simulation produces too much viscosity, which causes a delay of separation, leading to a region of attached flow that is too large. This in turn leads to a predicted lift that is too high. Secondly, the turbulence model does not correctly take into account the transport of momentum in the far field. This is because turbulence modelled in a RANS simulation is assumed isotropic, which will force the flow to be kept artificially two-dimensional as opposed to real turbulent flow. Here large-eddy simulation (LES) is in general successful. As opposed to RANS, which is time-averaged, LES uses spatial averaging, or filtering, of the NavierStokes equations, where the large eddies are resolved, or simulated, and only the smaller eddies are modelled assuming isotropic turbulence. In this way the correct three-dimensionality of the flow is predicted. The size of the grid cells govern the size of those eddies responsible for the transport of momentum to be resolved, and the smaller eddies to be modelled using a proper subgrid-scale (SGS) model. Close to the wall the turbulent eddies are so small (for Reynolds numbers relevant for wind turbine applications) that LES is an impractical solution method with respect to computational cost, since very small grid cells and also small time steps would be required to resolve the small eddies. One way to circumvent this is to combine a RANS model in the boundary layer with a LES model in the far field. The present method was suggested by Spalart et al. and is called detached-eddy simulation (DES). In this way the small attached eddies in the boundary layer will be modelled using a RANS turbulence model and the detached eddies in the far field will be resolved using an LES approach. In other words: A detached-eddy simulation is a three-dimensional unsteady numerical solution using a single turbulence model, which functions as a subgrid-scale model in regions where the grid density is fine enough for a large-eddy simulation, and as a Reynolds-averaged model in regions where it is not. Recent results, using the detached-eddy simulation model have shown better accuracy for highly separated flows owing to the better resolution of three-dimensional flow structures.[26]

The y^+ distribution over the airfoil is presented in figure 4.66 (a). It shows the highest y^+ value at the leading edge on the suction side, caused by the high acceleration of the flow from the stagnation point on the pressure side to the suction side. The averaged value of the y^+ is 10.7. Figure 4.66 (b) provides the velocity profile of a turbulent boundary layer on a hydraulic smooth wall, – and the y^+ distribution of the evaluated simulation lies between the buffer layer and the fully turbulent region.

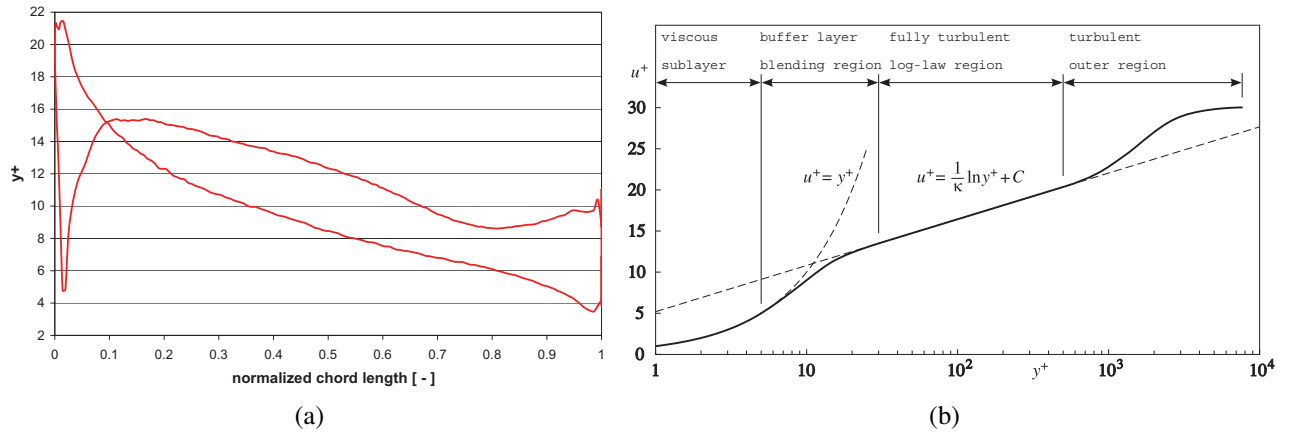


Figure 4.66: (a) Y^+ distribution of the evaluated simulation at 33.275 meters height, (b) velocity profile of a turbulent boundary layer on a smooth hydraulic wall (based on [27])

The influence of the y^+ value on the single airfoil section is very high regarding the drag coefficient, see table 4.11. In order to resolve the boundary layer correctly, and thus the wall shear, it is necessary to reach y^+ values of max. 1. With higher y^+ values the boundary layer changes and consequently the wall shear and the drag coefficient becomes higher. And the chosen simulation models take into account of the transition. In this case, a finer resolved mesh regarding the transition model and the y^+ value was limited by the computational performance.

Table 4.11: Influence of the y^+ value on the lift and drag coefficients simulated in comparison to the measurements for 7 degrees angle of attack

	y^+ ave	aspect ratio ave	c_l	c_d	c_l error	c_d error
	[-]	[-]	[-]	[-]	[%]	[%]
very fine	78.42	1 937.20	1.1134	0.0290	-13.02	213.79
middle	10.48	3 129.07	1.2280	0.0224	-4.06	142.31
measurement			1.28	0.00924	0.00	0.00

4.3.3.3 Airfoil Losses

The airfoil losses are caused by the drag of the airfoil. An idealized airfoil provides no drag losses. In order to be able to get a feeling for the height of the airfoil losses of the blade used it is necessary to have the aerodynamic coefficients of the wing.

The power of the wind turbine is calculated by equation 4.33 as an integration over the blade. A sketch of the integration over the blade is displayed in figure 4.67.

$$P = \omega \cdot B \cdot \sum r \cdot dF_{ta} \quad (4.33)$$

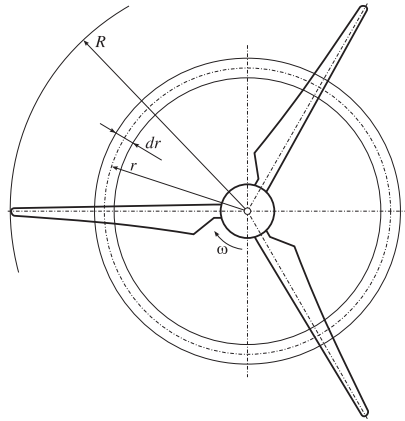


Figure 4.67: Circular ring segment for the incremental calculation of the power [27]

The tangential force can be calculated as idealized with no drag of the airfoil or as real with lift and drag of the airfoil. The equation is stated below:

$$F_{ta,ideal} = \frac{\rho}{2} \cdot c^2 \cdot l_c \cdot dr \cdot c_L \cdot \sin(\phi) \quad (4.34)$$

$$F_{ta,real} = \frac{\rho}{2} \cdot c^2 \cdot l_c \cdot dr \cdot (c_L \cdot \sin(\phi) - c_D \cdot \cos(\phi)) \quad (4.35)$$

The airfoil efficiency can be derived from the quotient of $\frac{F_{ta,real}}{F_{ta,ideal}}$, which leads to the equation:

$$\eta_{airfoil} = 1 - \frac{c_d}{c_l} \cdot \frac{1}{\tan(\phi)} \quad (4.36)$$

Thus, it can be proved that the losses are inversely proportional to the glide ratio. By means of equation 4.33 it can be demonstrated that the airfoil should have high glide ratios (>50) in the outer blade area, where huge moments occur because of the long lever arm. To evaluate the power of the wind turbine, different airfoil sections were realized in order to be able to calculate the power as a summation, see equation 4.33 and table 4.12. The analyzed data were further used to calculate the airfoil losses. To prove the results of the evaluated sizes, the summation

is compared with the results of ANSYS Post. The calculated force should be of the same size as the evaluated force according to ANSYS Post.

Table 4.12: Power calculation with evaluated values of the simulation: 150 nodes chordwise, leading and trailing edge 12 nodes, $n = 15.7$ [rpm], $\alpha = 6.843$ [deg] and operating point 3, see table 4.10

r	distance from root	ϕ	w	l_c	c_l	c_d	glide ratio	η_{airfoil}	mech. power
[m]	[m]	[deg]	[m/s]	[m]					[kW]
3.275	2	65.06	12.77	2.45	0.6790	0.4303	1.58	0.71	3.63
5.275	4	51.77	14.02	2.93	0.7984	0.3886	2.05	0.62	7.51
7.275	6	39.77	15.56	3.37	1.0336	0.2788	3.71	0.68	17.00
9.275	8	29.63	17.54	3.57	1.1318	0.1512	7.49	0.77	27.94
11.275	10	26.79	20.77	3.49	1.0254	0.1348	7.60	0.74	37.09
13.275	12	21.53	23.46	3.24	1.0456	0.0859	12.17	0.79	46.02
15.275	14	18.50	26.48	2.99	1.0770	0.0712	15.12	0.80	56.18
17.275	16	14.47	29.33	2.72	1.1229	0.0310	36.17	0.89	64.81
19.275	18	13.50	32.59	2.47	1.1338	0.0415	27.29	0.85	72.79
21.275	20	12.66	35.85	2.26	1.1435	0.0449	25.48	0.83	81.69
23.275	22	11.04	38.99	2.06	1.1718	0.0320	36.66	0.86	90.19
25.275	24	10.26	42.23	1.89	1.1773	0.0311	37.83	0.85	97.92
27.275	26	9.31	45.44	1.75	1.1984	0.0267	44.96	0.86	105.57
29.275	28	8.27	48.64	1.62	1.2225	0.0188	64.94	0.89	112.86
31.275	30	7.75	51.89	1.53	1.2326	0.0212	58.12	0.87	119.56
33.275	32	7.22	55.14	1.44	1.2391	0.0206	60.04	0.87	126.04
35.275	34	6.86	58.41	1.36	1.2401	0.0219	56.53	0.85	132.69
37.275	36	6.44	61.67	1.30	1.2305	0.0214	57.55	0.85	137.55
39.275	38	6.16	64.95	1.30	1.2161	0.0233	52.08	0.82	147.75
41.275	40	6.14	68.25	1.15	1.2058	0.0302	39.92	0.77	140.40
43.275	42	5.41	71.47	1.02	1.1999	0.0227	52.97	0.80	131.20
45.275	44	6.52	74.92	0.79	1.0838	0.0517	20.96	0.58	46.09
46.275	45	6.71	76.61	0.41	0.9438	0.0546	17.29	0.51	11.87
46.475	45.2	6.85	76.96	0.24	0.8189	0.0725	11.30	0.26	0.54

The result for the mechanical power calculated is $\sum P = 1814.9$ [kW], see table 4.12 and the power calculated with ANSYS CFX Post is 1841.2 [kW]. This led to the cognition that the calculation of forces and angles is quite good. Different literary sources claim that high glide ratios (>50) have to be applied in the outer area of the blade. However, as listed in table 4.12, a high glide ratios are rarely reached as of the too high drag coefficient prediction for one airfoil, see 4.3.3.2. The size of the drag coefficient predicted with ANSYS at a radii of 33.275 meter, is 0.021 however, the measured size of the drag coefficient of this airfoil (DU-93-W210) at an angle of attack of 6.84 degrees is 0.00924, (a deviation of nearly 56%).

4.4 Flow Physics

Different flow phenomena which cannot be illustrated by means of 2D simulations are known. These so-called 3D effects are:

- Large separation regions
- Changes in lift and drag coefficients
- Dynamic stall effects

A change in lift and drag, between the 2D wind tunnel measurement and the 3D simulation, can be noticed. Compared to the 2D measurements, in the near hub region a higher lift coefficient is allocated, and in the blade tip region a lower lift coefficient is allocated. These are both caused by 3D effects.

As of the low flow velocity, the influence of the Coriolis and of the centrifugal force is heavily. Under these influences the flow separates and moves radial in direction to the blade tip. This behavior is displayed in figures 4.68 and 4.69. The separated helix flow is located up to 16 meters height, see figure 4.69 (a).

The separation can also be detected at the pressure coefficient distribution over the sectional planes at the blade. In figure 4.70, the streamline plot with the associated pressure coefficient plot are displayed. The negative pressure coefficient on the pressure side produces a negative lift which results in a low (or negative) power at this wing section, i.e. listed in table 4.12 at row 3.275 meters. The pressure coefficient plots, together with the associated velocity or/and streamline plots, are made up to a height of 15.275 meters, see figure 4.70, 4.71, 4.72 and 4.73. The difference between a separated and an attached flow on the airfoil is presented in figure 4.74.

The figures included in this section are evaluated based on the 250 nodes chordwise rotor mesh.

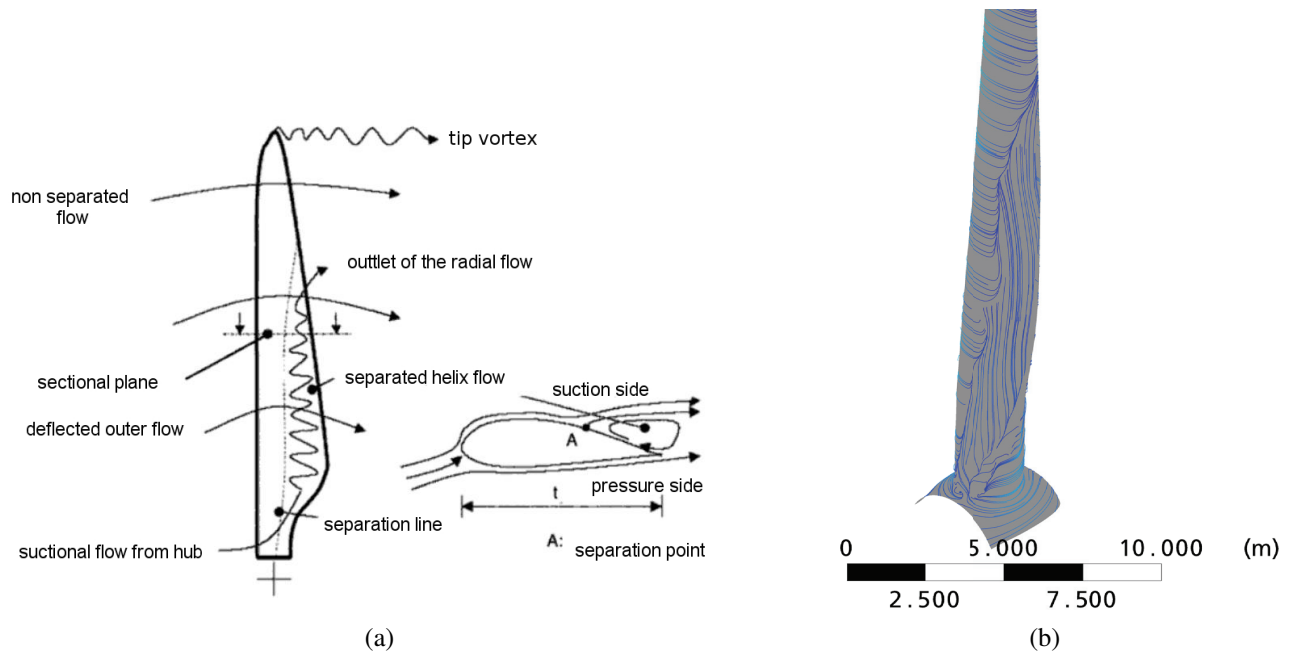


Figure 4.68: (a) Sketch of the flow in the separation area on the suction side (based on [12]), (b) 3D view of a streamline plot on the suction side

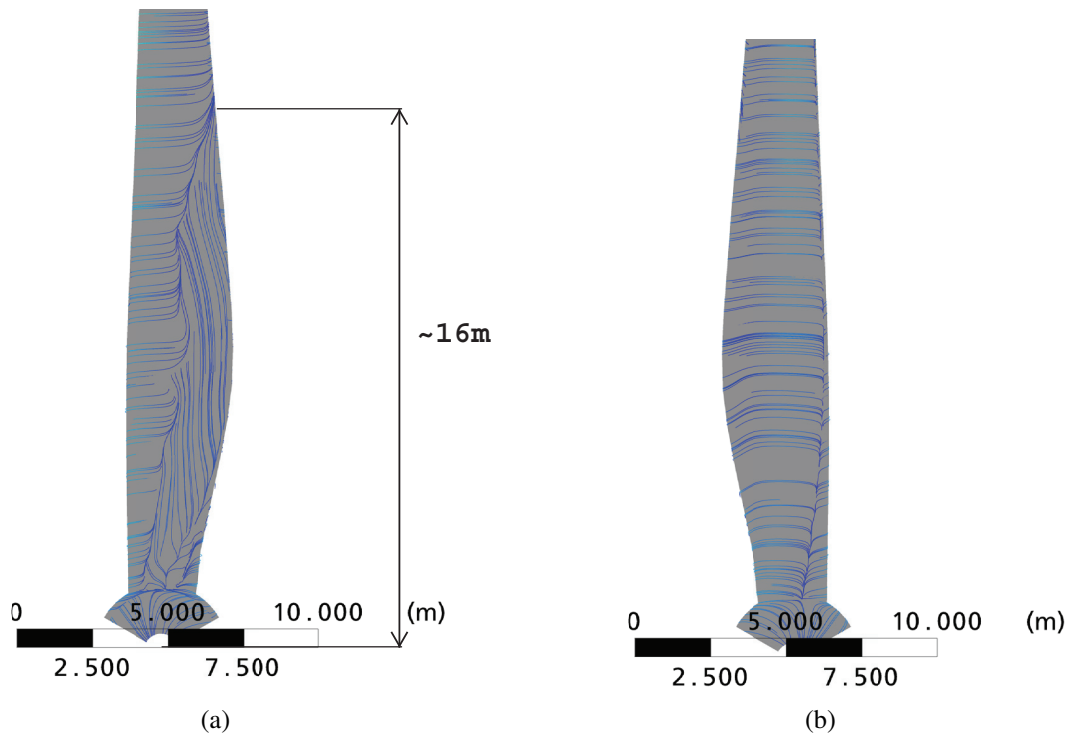


Figure 4.69: (a) 2D view of the surface streamline plot on the suction side, (b) 2D view of the surface streamline plot on the pressure side

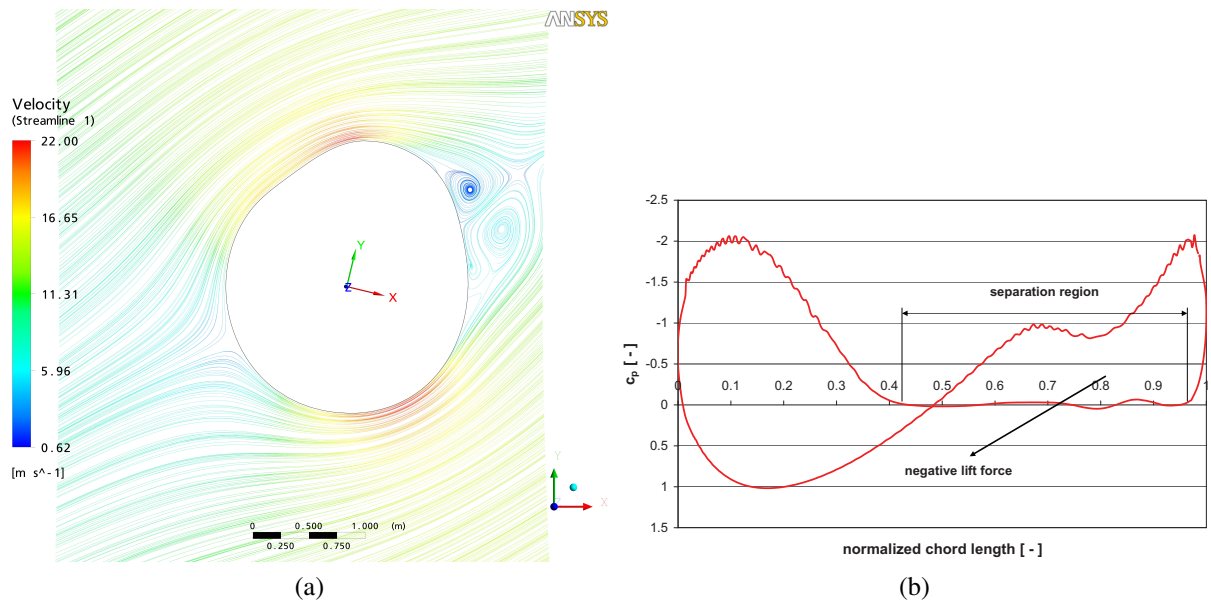


Figure 4.70: Sectional plane at a height of 3.275 meters, (a) 2D view of the surface streamline of the flow, (b) pressure coefficient plot over the normalized chord length

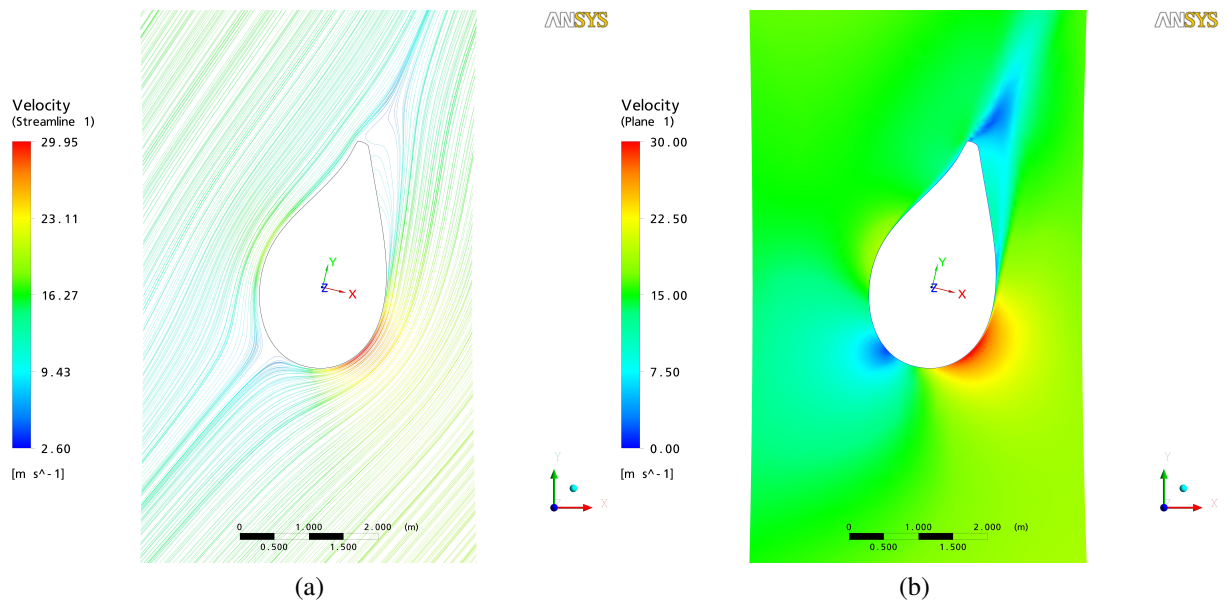


Figure 4.71: Sectional plane at a height of 7.275 meters, (a) 2D view of the surface streamline of the flow, (b) velocity plot

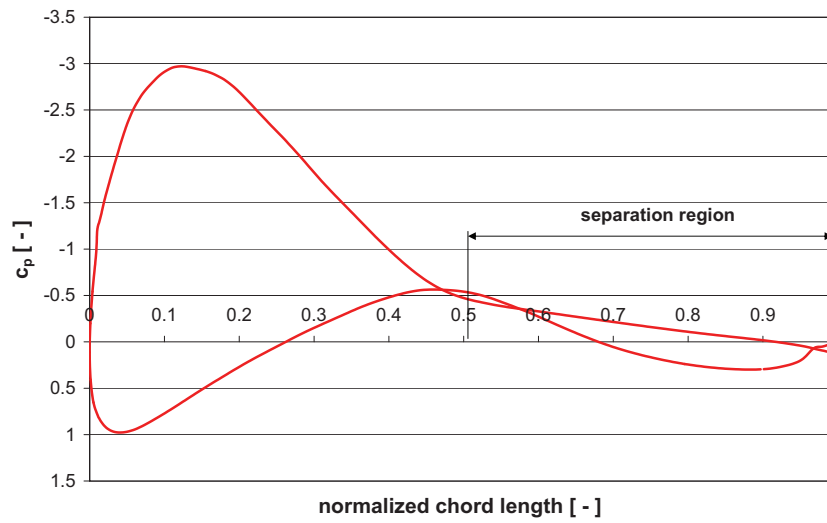


Figure 4.72: Pressure coefficient plot over the normalized chord length at 7.275m height

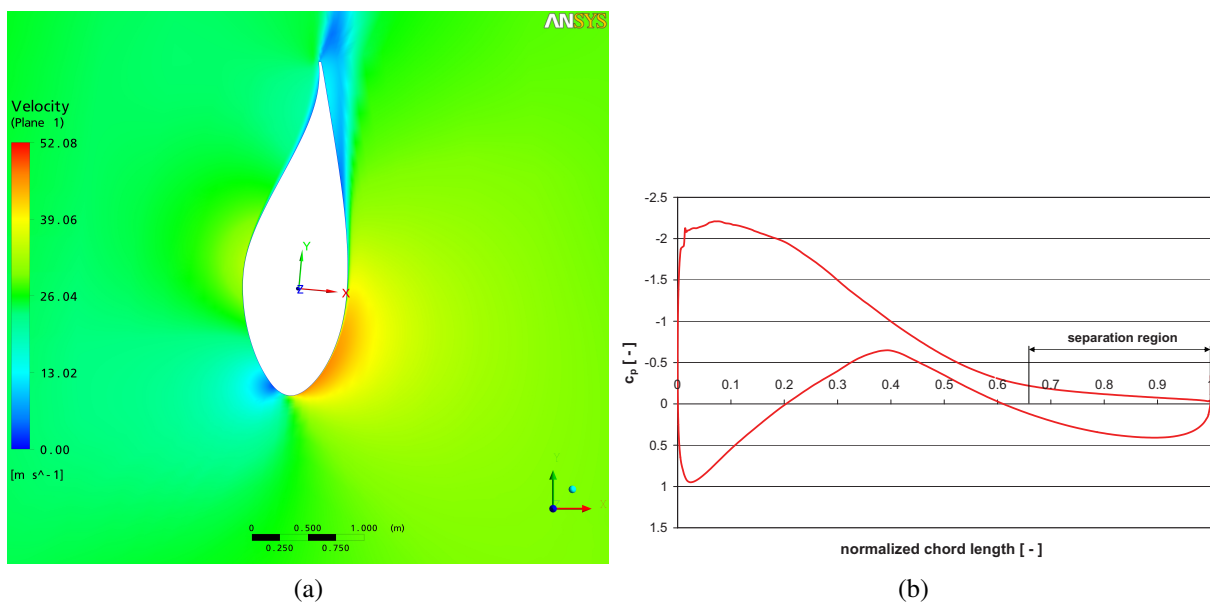


Figure 4.73: Sectional plane at a height of 15.275 meters, (a) velocity plot, (b) pressure coefficient plot over the normalized chord length

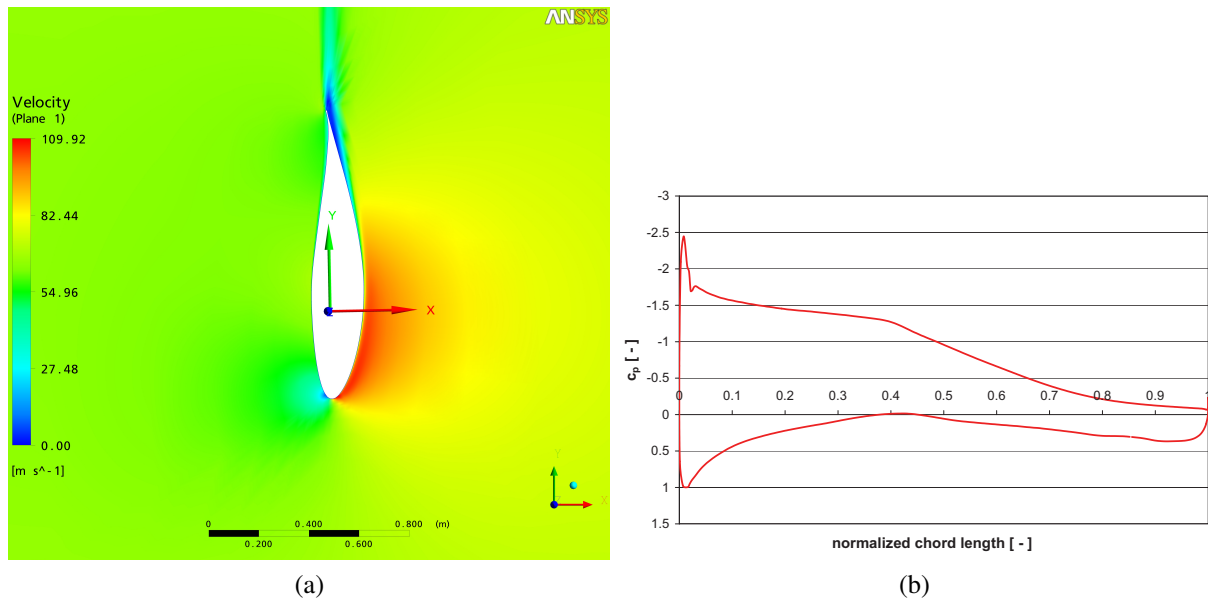


Figure 4.74: Sectional plane at a height of 41.275 meters, (a) velocity plot, (b) pressure coefficient plot over the normalized chord length

Another phenomenon is the **dynamic stall**, presented in figure 4.75. Whereas dynamic stall refers to rapid aerodynamic changes. *Dynamic stall will occur on any airfoil or other lifting surface when it is subjected to time-dependent pitching, plunging or vertical translation, or other type of motion, that takes the effective angle of attack above its normal static stall angle. Under these circumstances, the physics of the onset of flow separation and the development of stall is distinctly different to the stall mechanism exhibited by the same airfoil under static (quasi-steady) conditions. Dynamic stall has been extensively studied experimentally, mostly using oscillating two-dimensional airfoils in wind tunnel experiments. The majority of the documented experimental results are for airfoils oscillating in pitch (angle of attack), but there are some limited amounts of data available for other types of motions, such as plunging oscillations and constant angular rate (ramp) type motion. If dynamic stall becomes sufficiently severe on a wind turbine or a helicopter rotor, it can produce loads that may quickly exceed the structural fatigue limits. [21]*

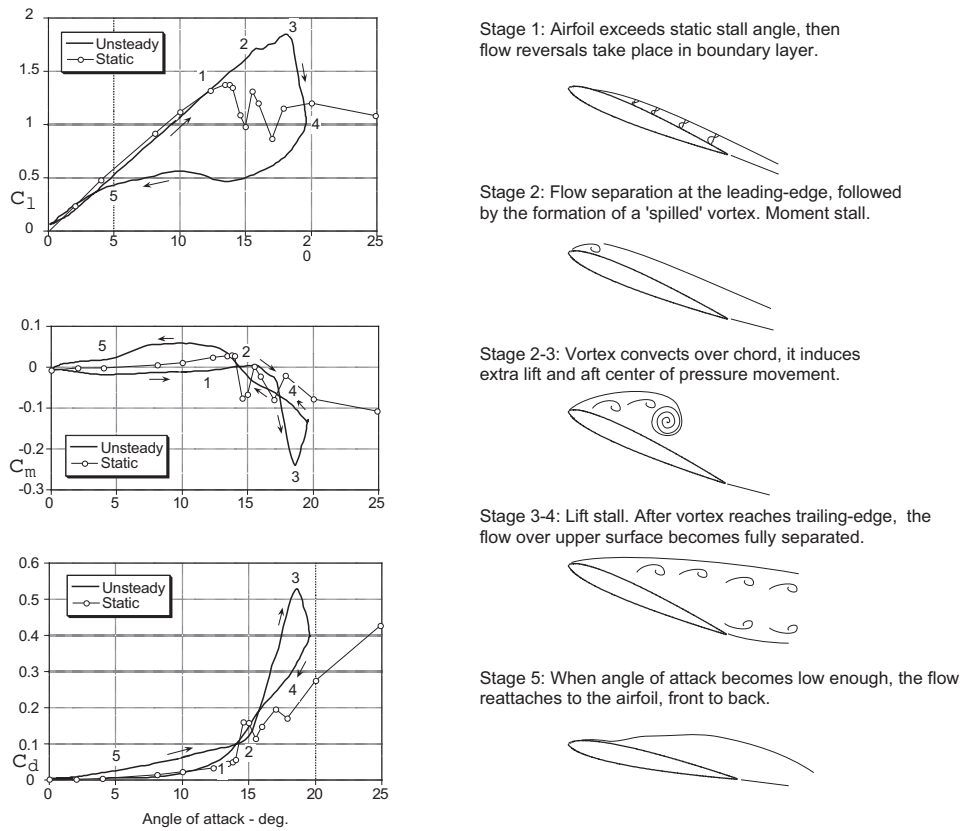


Figure 4.75: Schematic presentation of unsteady airloads and flow physics for a 2D airfoil undergoing dynamic stall [21]

5 Total Wind Turbine Model

In order to complete my diploma thesis, the complete wind turbine was modeled, see figure 5.1. It was my motivation to fulfill the demands started by the company Windtec.

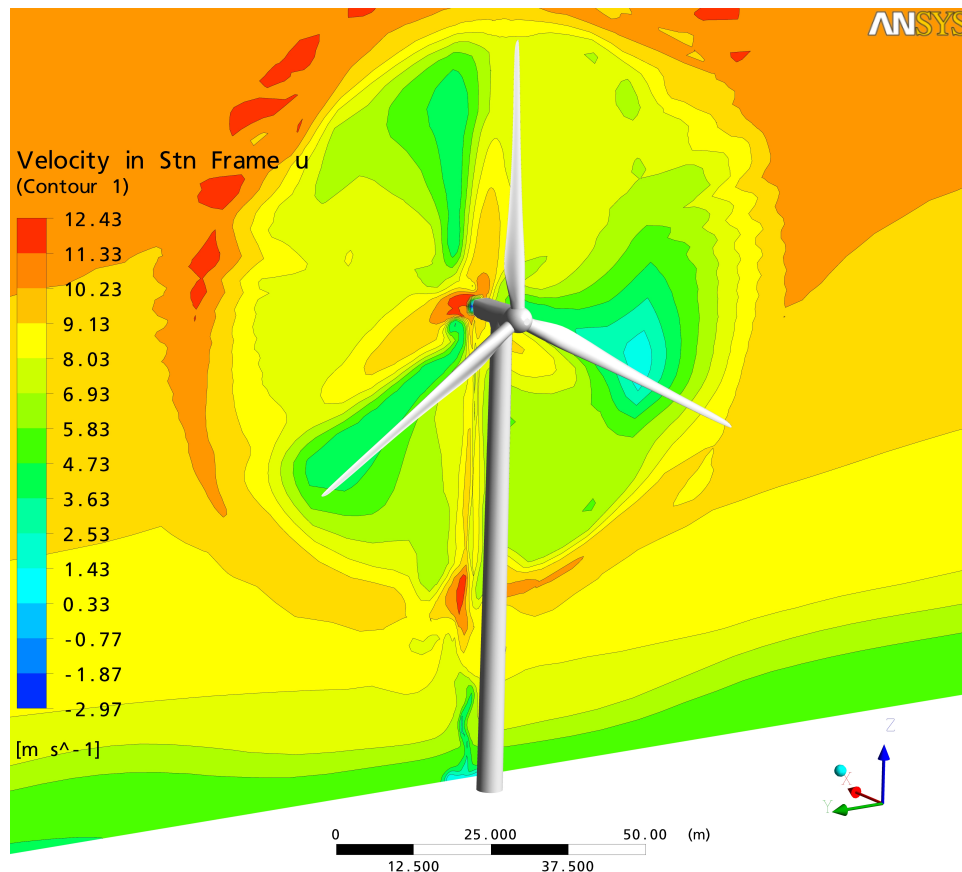


Figure 5.1: 3D view of the 360 degrees model, with a "stationary velocity u " contour plot in the background

5.1 Grid Construction

The challenge of grid construction was to model the different parts of the wind turbine:

- 360 degrees rotor consists of 3 blades and a spinner
- Nacelle
- Tower

- Surrounding area

The already existing rotor mesh was taken, whereas the geometry with the block structure was rotated around the y-axis about 4.5 degrees. As this was the original orientation between the rotational axis of the rotor and the axis of the tower, this model is displayed in figure 5.2. To mesh the complete 360 degree model was not possible because of the high number of nodes and the limitation in computer working memory. As a result, the single 120 degree rotor was copied into ANSYS CFX Pre about the rotational axis to a full circle model. The periodic interfaces were glued together with a non-periodic GGI interface.

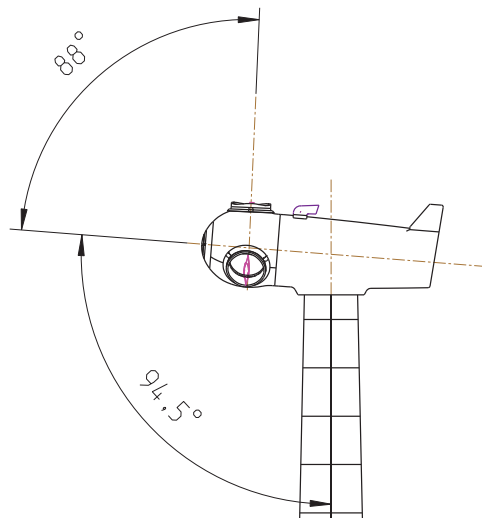


Figure 5.2: Axis orientation between the tower and the rotor

Based on the geometrical informations of the above-mentioned rotated mesh, the stationary area was modeled in total. The stationary domain consists of the nacelle, the tower and the surrounding area.

In order to create a structured mesh, a very complicated block structure was needed. A sketch of the near rotor region block structure of the stationary domain is displayed in figure 5.3, where the Xs symbolize the deleted blocks and the horizontal and vertical lines symbolize the block borders. Based on this sketch, the block structure in ICEM CFD was generated, see figure 5.4. Table 5.1 includes all statistic mesh data.

Table 5.1: Table statistic mesh data

domain	nodes	elements
rotor	2 932 113	2 810 376
stationary	3 151 240	3 077 248
total	6 083 353	5 887 624

The inlet boundary condition was the wind profile explained in chapter 3.1. The surfaces between the rotational domain and the stationary domain were connected by means of a frozen rotor interface.

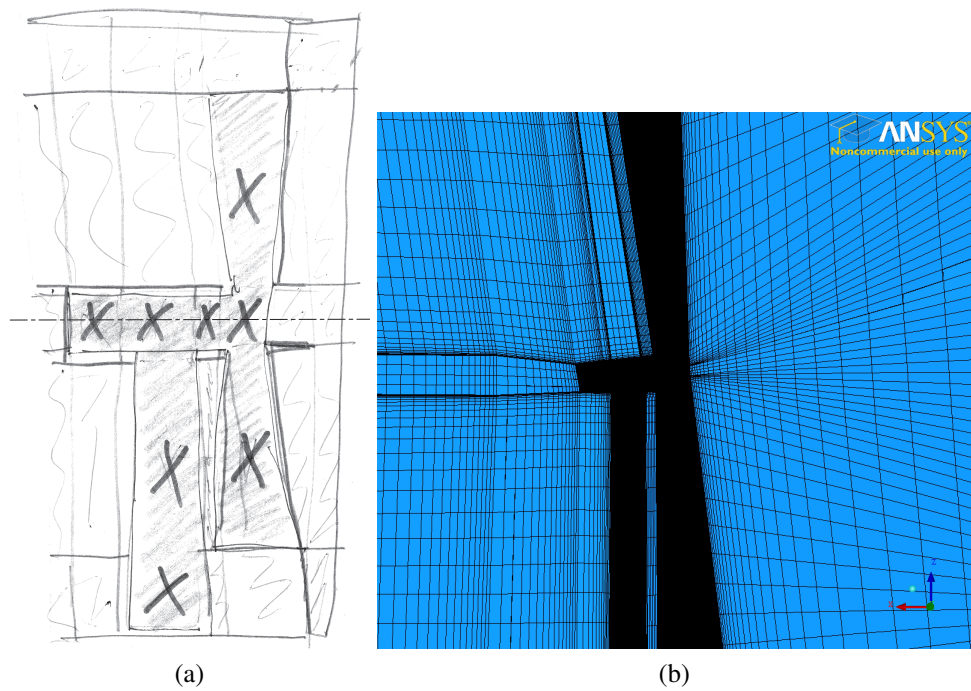


Figure 5.3: (a) sketch of the block structure for the stationary domain, (b) generated grid

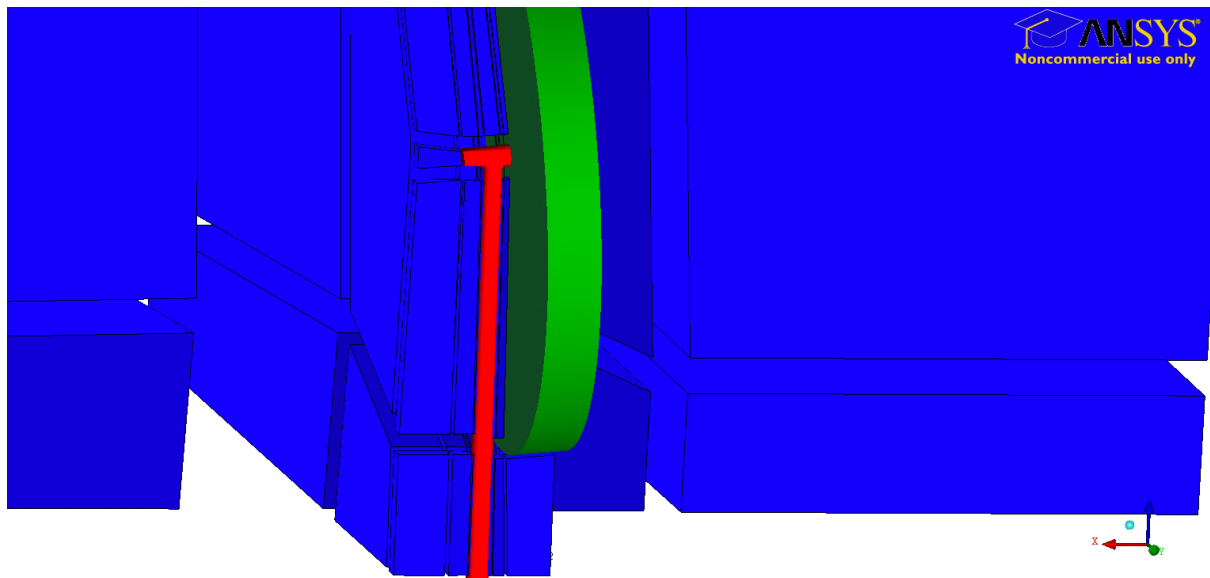


Figure 5.4: Picture of the block structure in ICEM, red marks the tower and the nacelle, green the rotor domain, the blue cuboids are the blocks, stationary domain

5.2 Results

The steady-state simulation with the calibrations of the 120 degree simulation results in a mechanical power of **1807 kW** after 600 time steps.

For the evaluation concerning the anemometer and cooler positioning, a velocity plot was made at a x distance of 8 meter. It seems, that this region at the end of the nacelle, where the original cooler is positioned, includes the highest velocities, see figure 5.6. However, for realistic results a transient simulation has to be done.

Furthermore diverse plots of interesting points are displayed in figures 5.5, 5.7 and 5.8.

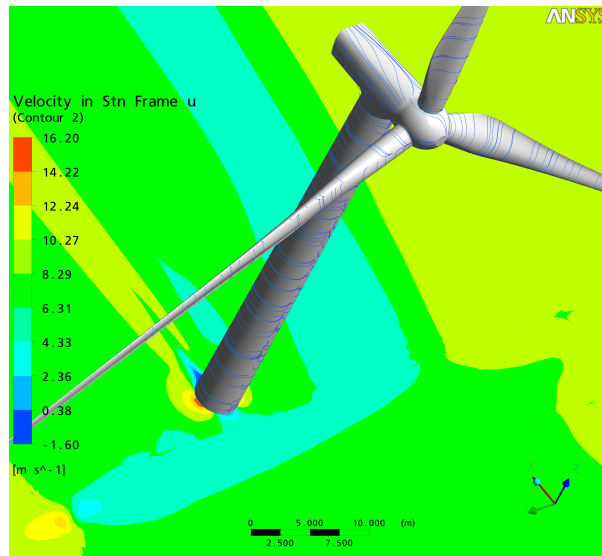


Figure 5.5: Velocity u in stationary frame at z = -20 meters, with a surface streamline plot showing the tower influence

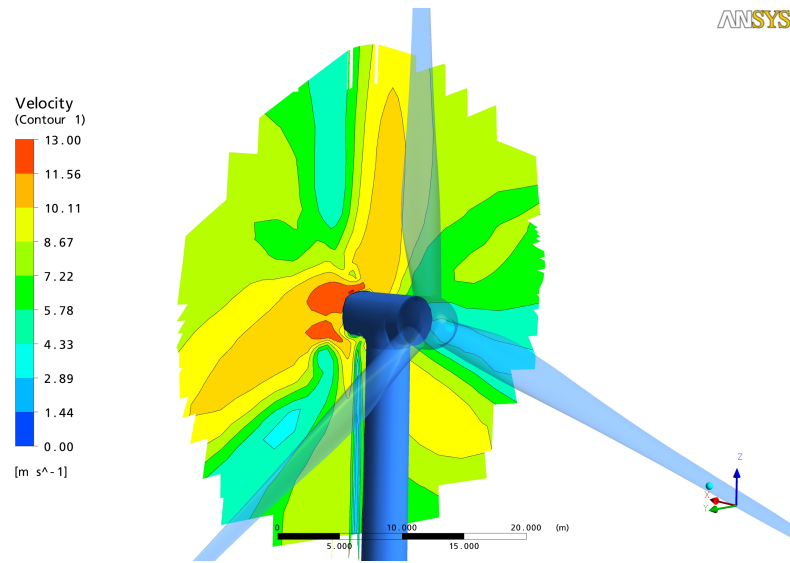


Figure 5.6: Velocity contour plot concerning the anemometer and cooler positioning at $x = 8$ meters

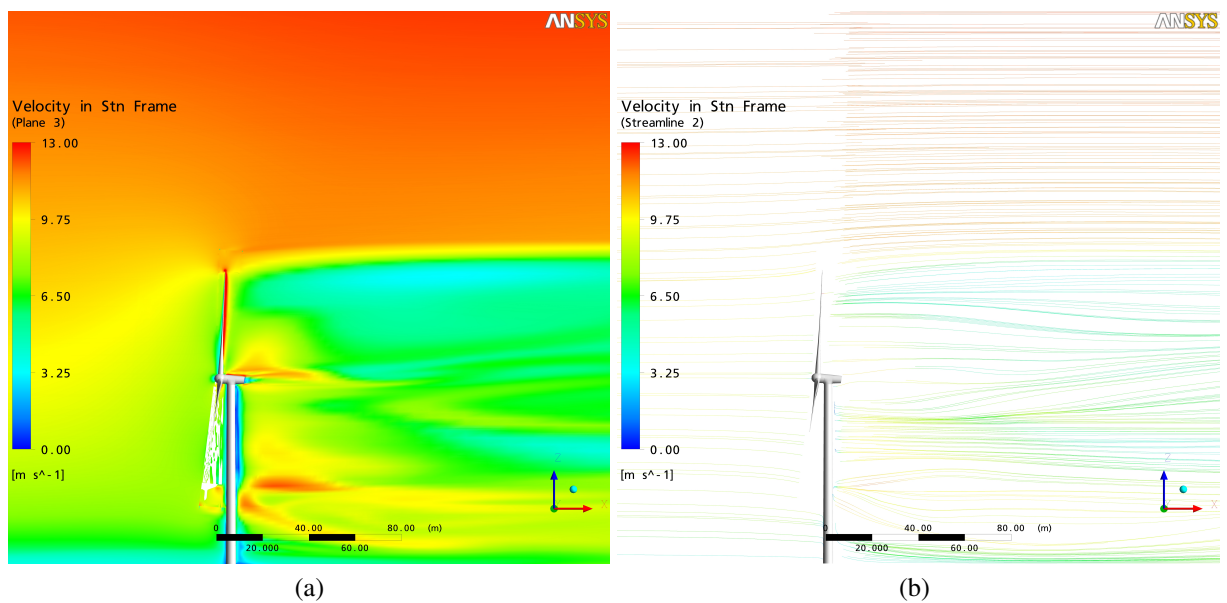


Figure 5.7: (a) Velocity u in stationary frame at a xz plane with $y = 0$ meters, (b) surface streamline plot on a xz plane with $y = 0$ meters

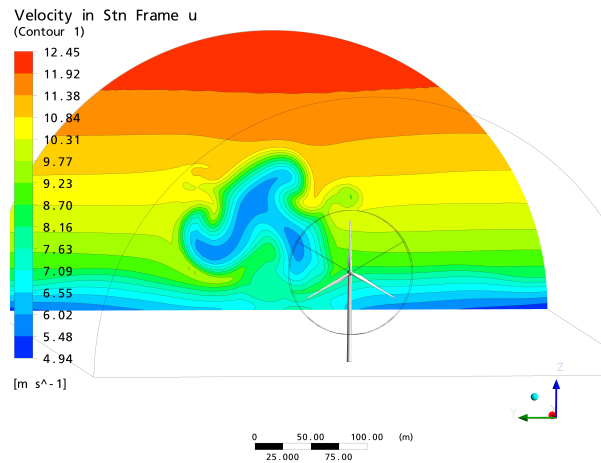


Figure 5.8: Velocity u in stationary frame plot on a yz plane at x = 550 meters, shows spin flow with additional tip vortex

5.3 Outlook

For future investigations it is recommended to realize a refinement of this simulation. Furthermore, the realization of a transient simulation of the whole wind turbine model is necessary, in order to analyze the rotor-, tower- and nacelle interactions. The rotor tower interactions are caused by the near tower region, and this region leads to a change in the airfoil approaching flow.

Also, the situation of wind parks is of great interest as of the phenomenon of the rotor wake, which leads to higher turbulences in the afterwards approaching flow.

6 Outlook

This diploma thesis describes the work flow of building up a CFD simulation. The influence of the turbulence and numerical model on the coefficients, especially the lift and drag coefficient, is presented. There is always the question: "What is my aim?" And, based on this question, a numerical and turbulence model with the right mesh adjustments concerning the y^+ value has to be chosen.

Also, the influence of the refinements of the grid is presented as its knowledge saves a lot of working effort. The acknowledgment of the grid influence is also of good help when computational resources are restricted.

In my opinion, the work presented is a cornerstone and, based on it many other points of interest can be simulated. A simulation of a wind turbine offers many interesting and open work fields. Every kind of interaction is worth to be investigated. Also, there is a large potential of flow optimization around every component. And, the area of fluid structure interaction (CFD CSD Coupling) is a region of much further development as well.

List of Figures

2.1	Power curve [1]	2
2.2	The result in Excel for spinner	4
2.3	Procedure of intersection in ProE WILDFIRE	5
2.4	Procedure of intersection in ProE WILDFIRE for the blade, the result is displayed in figure 2.7	5
2.5	The distortion of the J-grid around the airfoil	6
2.6	The wind turbine boundary condition	7
2.7	Sorted airfoil	8
2.8	The dimensions of the surrounding area and the wind turbine wake (based on paper [6])	9
2.9	A larger scale sketch of the O-grid structure around the airfoil and edge declaration	12
2.10	3D-view of the block structure in spanwise direction (a) with realization (b) without realization of the tip vortex in the rotational domain	12
2.11	Sketch of the block structure with outer contour points and with dash lines which show the divisions of the block and edge declaration	14
2.12	Sketch of the O-grid block structure around the airfoil with edge declaration	15
2.13	Detail of the surrounding mesh	18
3.1	Sketch of the domains with denotation	19
3.2	(a) Sketch of the earth boundary layer (based on [12]), (b) chart of the results of equation 3.1 with $a = 0.2$, $v_r = 9.75$ [m/s] and $z_{Hub} = 80$ [m]; additionally a sketch of the rotor is presented	21
3.3	The residuals and the power curve for Auto Timescale at operating point 2	23
3.4	The residuals and the power curve for Physical Timescale 0.1s at operating point 2	24
3.5	The residuals and the power curve for Local Timescale Factor 10 at operating point 2	25
3.6	A larger scaled view at the power curve chart with Local Timescale Factor 10 at operating point 2	26
4.1	The calculated power over the pitch angle with different mesh sizes of the rotor domain for operating point 1	29
4.2	The calculated power over the pitch angle with different mesh sizes of the rotor domain for operating point 2	29
4.3	The calculated power over the pitch angle with different mesh sizes of the rotor domain for operating point 3, results for different boundary conditions and additionally the results for the tip vortex realization	30

4.4	The power coefficient over the pitch angle with different mesh sizes of the rotor domain for operating point 3, results for different boundary conditions and additionally the results for the tip vortex realization	30
4.5	The mechanical efficiency over the pitch angle with different mesh sizes of the rotor domain for operating point 3, results for different boundary conditions and additionally the results for the tip vortex realization	31
4.6	The calculated power over the pitch angle with different mesh sizes of the rotor domain for operating point 4	31
4.7	Relative error between $v = f_{(z)}$ and $v = \text{const.}$ for operating point 3, with a mesh size of 1 100 000 nodes for the rotor domain	33
4.8	2D pressure plot (a) with realization (b) without realization of the tip vortex . .	35
4.9	3D streamline plot of the tip vortex	35
4.10	According to Betz and Schmitz, the power coefficient over tip speed ratio is displayed, the hatched area describes the spin loss [12]	36
4.11	Spin flow (a) sketch [12] (b) with additional tip vortex	36
4.12	Chart of the velocity difference on yz plane at inlet domain, (a) chart has a x-axis range from -270 to -30 meters, (b) has a range from -30 to -3 meters . . .	38
4.13	Chart of the velocity difference on lines at inlet domain, (a) chart has a x-axis range from 40 to 450 meters, (b) has a range from 10 to 40 meters	39
4.14	Chart of the velocity difference on yz plane at outer domain, (a) chart has a x-axis range from -70 to +50 meters, (b) has a range from -10 to +10 meters . .	40
4.15	Chart of the velocity difference on a surface of revolution with outer domain mesh 1 in comparison to mesh 2, (a) chart has a x-axis range from 100 to 440 meters radius, (b) has a range from 60 to 100 meters radius	40
4.16	Chart of the velocity difference on lines through the outer domain, x-axis range from 60 to 450 meters	41
4.17	Chart of the velocity difference on yz plane at the outlet domain	41
4.18	Figure of the rotor wake flow [13]	42
4.19	Figure of the grid around the airfoil in xy plane at 40 meters, (a) view at the trailing edge, (b) view at the leading edge	44
4.20	Result of mechanical power for operating point 3, ANSYS versus Bladed . . .	46
4.21	Results for operating point 3, (a) power coefficient curve, (b) efficiency curve, ANSYS versus Bladed	46
4.22	Results for operating point 3 with pitch angle -0.8 degree, with a nearly constant averaged y^+ value of 17, (a) mechanical power, (b) deviation from Bladed	47
4.23	Influence of the chordwise refinement on the mechanical power	48
4.24	The influence of the aspect ratio on the mechanical power	49
4.25	The influence of the spanwise refinement, (a) lift coefficient over aspect ratio, (b) drag coefficient over aspect ratio	49
4.26	The influence of the chordwise refinement over the whole blade, (a) lift coefficient over normalized blade length, (b) drag coefficient over normalized blade length	50
4.27	The influence of the chordwise refinement, (a) lift coefficient over number of nodes, (b) drag coefficient over number of nodes	51

4.28	The influence of the chordwise refinement at the airfoil at 33.275 meters, (a) pressure coefficient over normalized chord length, (b) zoomed view at the stagnation point region	52
4.29	Post plots at 33.275 meters to explain the pressure coefficient plot, (a) velocity plot, (b) pressure plot,	52
4.30	Post plots at 33.275 meters to explain the pressure coefficient plot, (a) streamlines plot, (b) surface discontinuity	53
4.31	Airfoil sketch and nomenclature [18]	54
4.32	Design targets for a HAWT blade [14]	55
4.33	Notation of the force situation at an airfoil (based on [27])	55
4.34	Sketch of the specific blade work over radius, (a) a shrouded machine with a constant H_u , (b) a non-shrouded machine with a variable H_u over the radius	56
4.35	Slip stream streamtube with static pressure and axial velocity distribution (based on [27])	57
4.36	Sketch of the velocity triangle of a wind turbine flow at a defined radius	58
4.37	Airfoils at specific radii	61
4.38	Twist angle of the WT93 blade over normalized radii	61
4.39	A comparison of the DU-93-W-210 airfoil, with the airfoil at 33.275m height	62
4.40	A comparison of the DU-93-W-210 airfoil with 2 NACA profiles the NACA 65 ₃ - 418 profile is a laminar one	63
4.41	The measured lift coefficient over the angle of attack, for DU-93-W-210	64
4.42	The measured drag coefficient over the angle of attack, for DU-93-W-210	64
4.43	Measured airfoil polar, for DU-93-W-210	65
4.44	Influence of the viscous effects for an airfoil [19]	66
4.45	Influence of the angle of attack on the skin friction coefficient for the DU-93-WT-210 (results from simulation)	66
4.46	The transition point located at the airfoil at 33.275m	67
4.47	Sketch of the flow over an airfoil, with transition and separation [12]	67
4.48	Calculated values with velocity and pressure plot at 39.275 meters	68
4.49	View at the axial velocity method in ANSYS CFX Post, 2 surfaces of revolution are presented	69
4.50	The plotted absolute velocity over the x distance at 33.275 meters height	69
4.51	In both figures, the differences between the Rav method and the 1D idealized Betz method are compared, (a) shows the axial induction factor over the normalized radius, (b) shows the angle of attack over the normalized radius	70
4.52	Created coordinate frame for an airfoil	71
4.53	In both figures, the differences between the Rav method and the 1D idealized Betz method are compared, (a) shows the lift coefficient over the number of nodes, (b) shows the drag coefficient over the number of nodes	72
4.54	Varied angle of attack, based on the Rav method, and influence on the drag coefficient	72
4.55	The lift coefficient over the angle of attack	74
4.56	The drag coefficient over angle of attack	74
4.57	(a) shows the pressure coefficient plot at an angle of attack of 6 degrees (based on [25]), (b) pressure coefficient plot at an angle of attack of 6 degrees, 3D RANS SST fully turbulent simulation	75

4.58	(a) skin friction coefficient plot at an angle of attack of 6 degrees (based on [25]), (b) skin friction coefficient plot at an angle of attack of 6 degrees, 3D RANS SST fully turbulent simulation	76
4.59	3D simulated flow over the DU-93-WT-210 airfoil at an angle of attack of 6 degrees ,(a) 2D view at the surface streamlines of the flow, (b) velocity plot	76
4.60	(a) pressure coefficient plot at an angle of attack of 10 degrees (based on [25]), (b) pressure coefficient plot at an angle of attack of 10 degrees, 3D RANS SST fully turbulent simulation	77
4.61	(a) skin friction coefficient plot at an angle of attack of 10 degrees (based on [25]), (b) skin friction coefficient plot at an angle of attack of 10 degrees, 3D RANS SST fully turbulent simulation	78
4.62	3D simulated flow over the DU-93-WT-210 airfoil at an angle of attack of 10 degrees (a) 2D view of the surface streamlines of the flow, (b) velocity plot	78
4.63	(a) pressure coefficient plot at an angle of attack of 14 degrees (based on [25]), (b) pressure coefficient plot at an angle of attack of 14 degrees, 3D RANS SST fully turbulent simulation	79
4.64	(a) skin friction coefficient plot at an angle of attack of 14 degrees (based on [25]), (b) skin friction coefficient plot at an angle of attack of 14 degrees, 3D RANS SST fully turbulent simulation	80
4.65	3D simulated flow over the DU-93-WT-210 airfoil at an angle of attack of 14 degrees, (a) 2D view of the surface streamlines of the flow, (b) velocity plot	80
4.66	(a) Y+ distribution of the evaluated simulation at 33.275 meters height, (b) velocity profile of a turbulent boundary layer on a smooth hydraulic wall (based on [27])	82
4.67	Circular ring segment for the incremental calculation of the power [27]	83
4.68	(a) Sketch of the flow in the separation area on the suction side (based on [12]), (b) 3D view of a streamline plot on the suction side	86
4.69	(a) 2D view of the surface streamline plot on the suction side, (b) 2D view of the surface streamline plot on the pressure side	86
4.70	Sectional plane at a height of 3.275 meters, (a) 2D view of the surface streamline of the flow, (b) pressure coefficient plot over the normalized chord length	87
4.71	Sectional plane at a height of 7.275 meters, (a) 2D view of the surface streamline of the flow, (b) velocity plot	87
4.72	Pressure coefficient plot over the normalized chord length at 7.275m height	88
4.73	Sectional plane at a height of 15.275 meters, (a) velocity plot, (b) pressure coefficient plot over the normalized chord length	88
4.74	Sectional plane at a height of 41.275 meters, (a) velocity plot, (b) pressure coefficient plot over the normalized chord length	89
4.75	Schematic presentation of unsteady airloads and flow physics for a 2D airfoil undergoing dynamic stall [21]	90
5.1	3D view of the 360 degrees model, with a "stationary velocity u" contour plot in the background	91
5.2	Axis orientation between the tower and the rotor	92
5.3	(a) sketch of the block structure for the stationary domain, (b) generated grid	93

5.4	Picture of the block structure in ICEM, red marks the tower and the nacelle, green the rotor domain, the blue cuboids are the blocks, stationary domain . . .	93
5.5	Velocity u in stationary frame at z = -20 meters, with a surface streamline plot showing the tower influence	94
5.6	Velocity contour plot concerning the anemometer and cooler positioning at x = 8 meters	95
5.7	(a) Velocity u in stationary frame at a xz plane with y = 0 meters, (b) surface streamline plot on a xz plane with y = 0 meters	95
5.8	Velocity u in stationary frame plot on a yz plane at x = 550 meters, shows spin flow with additional tip vortex	96
1	Convergence behavior of momentum and mass of the simulation with 150 nodes chordwise and n = 15.7 [rpm], see table 4.10 and chapter 4.3.3.2	106
2	Convergence behavior of turbulence of the simulation with 150 nodes chordwise and n = 15.7 [rpm], see table 4.10 and chapter 4.3.3.2	107
3	Convergence behavior of wall scale of the simulation with 150 nodes chordwise and n = 15.7 [rpm], see table 4.10 and chapter 4.3.3.2	108
4	Convergence behavior of the user point power in kW of the simulation with 150 nodes chordwise and n = 15.7 [rpm], see table 4.10 and chapter 4.3.3.2	109

List of Tables

2.1	Technical data sheet [1]	3
2.2	Mesh sizes of the produced -2 degrees model in TurboGrid	7
2.3	Importance, reaction and mesh weighting	10
2.4	Table of sizes of the different meshes (rotor domain)	11
2.5	Table of different meshes with their contour points	11
2.6	Table of the grid matrix (rotor domain)	13
2.7	Edge information for mesh 1 and mesh 2 with -0.8° pitch angle	16
2.8	Edge information for mesh 3 and mesh 4 with -0.8° pitch angle	17
2.9	Geometrical inlet, outlet and outer dimensions	18
2.10	The size of the mesh used for the surrounding area	18
3.1	Domain matrix of boundary conditions and interfaces	20
3.2	Operating points, (*averaged value)	20
3.3	Comparison, of the different settings, with and without the tip vortex visualization and different inlet boundary conditions	26
4.1	An excerpt of the mechanical power output from paper [4]	32
4.2	Sizes for calculating the tip efficiency (based on [12])	34
4.3	Mesh size study for operating point 3, with relative error, pitch angle $+0.8$ [deg]	37
4.4	Mesh sizes of the different surrounding domains	38
4.5	Determination of the first node spacing Δy away from blade wall, for a desired $y+$ value of 20	44
4.6	New mesh size study grids for the rotor domain with the scale size	45
4.7	Simulation matrix with the recreated meshes, the red x in the table marks the simulated meshes	45
4.8	$Y+$ and aspect ratio values for the meshes displayed in figure 4.22	47
4.9	Characteristics of the simulated Blade WT93 [1] (10.2010)	60
4.10	Different number of revolutions with the associated calculated beta infinity (with equation 4.25, the evaluated angle of attack, the Reynolds number and the mechanical power	73
4.11	Influence of the $y+$ value on the lift and drag coefficients simulated in comparison to the measurements for 7 degrees angle of attack	82
4.12	Power calculation with evaluated values of the simulation: 150 nodes chord-wise, leading and trailing edge 12 nodes, $n = 15.7$ [rpm], $\alpha = 6.843$ [deg] and operating point 3, see table 4.10	84
5.1	Table statistic mesh data	92

Bibliography

- [1] **Trattnig A., Jaber S.:** *Company AMSC Windtec*, Numerical Division, Klagenfurt, 2010.
- [2] **ANSYS Inc.:** *ANSYS TurboGrid User's Guide*, Release 12.1, November 2009.
- [3] **ANSYS Inc.:** *ANSYS CFX Reference Guide*, Release 12.1, November 2009.
- [4] **Laursen J., Enevoldsen P., Hjort S.:** *3D CFD Quantification of the Performance of a Multi Megawatt Wind Turbine*, Proceedings of the Journal of Physics (The Science of Making Torque from Wind), Conference Series 75, 2007.
- [5] **Tachos N.S., Filios A.E., Margaris D.P., Kaldellis J.K.:** *A Computational Aerodynamics Simulation of the NREL Phase II Rotor*, Proceedings of the Open Mechanical Engineering Journal, Volume 3, 2009.
- [6] **Gomez-Elvira R., Crespo A., et. al.:** *Anisotropy of turbulence in wind turbine wakes*, Journal Of Wind Engineering and Industrial Aerodynamics, 797-814, 2005.
- [7] **Pascal Jean Frey, Paul-Louis George:** *Mesh Generation, Application to Finite Elements, Second Edition*, pages 41-42, 2008.
- [8] **Tachos N.S., Filios A.E., Margaris D.P.:** *A comparative numerical study of four turbulence models for the prediction of HAWT flow*, Proceedings of the Institution of Mechanical Engineers, Volume 224 Part C: Journal of Mechanical Engineering Science, 2009.
- [9] **ANSYS Inc.:** *ANSYS CFX-Solver Modeling Guide*, Release 12.1, November 2009.
- [10] **Oertel Herbert, Laurien Eckart:** *Numerische Strömungsmechanik*, page 117, 1995.
- [11] **Wikipedia:** http://en.wikipedia.org/wiki/Blade_element_theory, October 2010.
- [12] **Gasch Robert:** *Windkraftanlagen, Grundlagen und Entwurf*, Teubner, Stuttgart, 1991.
- [13] **Lissaman P. B. S.:** *Energy Effectiveness of Arbitrary, Array of Wind Turbines*, AIAA paper 79-0114, 1979.
- [14] **Rooij R., Timmer N.:** *Design of Airfoils for Wind Turbine Blade*, Presentation, DUWIND, May 2004.
- [15] **Ziegler G.:** *Skript zur Vorlesung Hydraulische Strömungsmaschinen, Teil Windturbinen*, TU Graz, Institut für Hydraulische Strömungsmaschinen, letzte Version 1993.
- [16] **Schlichting H.:** *Grenzschicht-Theorie (Bild: Widerstandsbeiwert von Laminarprofilen und normalen Profilen)*, Braun-Verlag, Karlsruhe, 8. Auflage, 1982.

- [17] **Manwell J. F., McGowan J. G., Rogers A. L.:** *Wind Energy Explained: Theory, Design and Application*, John Wiley and Sons Ltd., 2nd Edition , 2009.
- [18] **Radespiel R.:** *Skript zur Vorlesung Strömungsmechanik II*, TU Braunschweig, Institut für Strömungsmechanik, SS 2007.
- [19] **Radespiel R.:** *Manuscript of lecture, Airfoil Aerodynamics*, TU Braunschweig, Institut für Strömungsmechanik, SS 2007.
- [20] **Hepperle M.:** *Program JavaFoil*, ©Martin Hepperle, 1996-2006.
- [21] **Leishman G. J.:** *Challenges in Modeling the Unsteady Aerodynamics of Wind Turbines*, 21st ASME Wind Energy Symposium and the 40th AIAA Aerospace Sciences Meeting, Reno, 2002.
- [22] **Hansen Mol., et. al:** *Extraction of lift, drag and angle of attack from computed 3D viscous flow around a rotating blade*, EWEC 97, 499-501, Dublin, 1997.
- [23] **Johansen J., Sorensen NN.:** *Airfoil characteristics from 3D CFD rotor computations*, Wind Energy, 7, 343-356, 2004.
- [24] **Hansen Mol., Johansen J.:** *Tip studies using CFD and computation with tip loss models*, Wind Energy, 7, 283-294, 2004.
- [25] **Bertagnolio F., Sorensen N.N., Johansen J.:** *Profile Catalogue for Airfoil Sections Based on 3D Computations*, Risø-R-1581(EN), Risø National Laboratory, Denmark, 2006.
- [26] **Sorensen N.N., Johansen J., Michelsen J. A., Schreck S.:** *Detached-Eddy Simulation of Flow Around the NREL Phase VI Blade*, Wind Energy, 5, 185-197, 2002.
- [27] **Kronschnabl F.J.:** *Numerische Strömungssimulation von Horizontalachsen Windturbinen*, Dissertation, S. 37, TU München, Lehrstuhl für Fluidmechanik, 2008.

Appendix

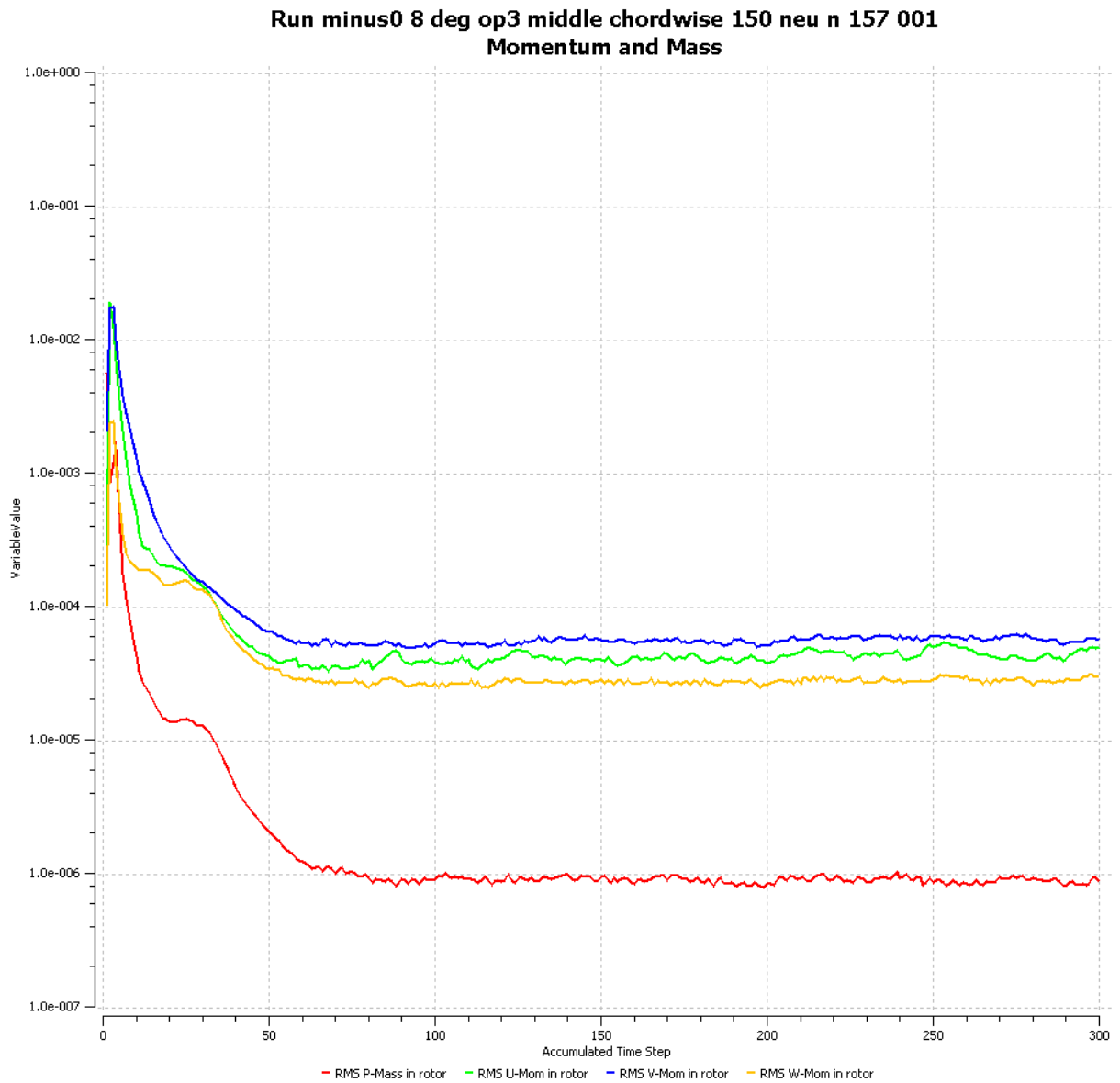


Figure 1: Convergence behavior of momentum and mass of the simulation with 150 nodes chordwise and $n = 15.7$ [rpm], see table 4.10 and chapter 4.3.3.2

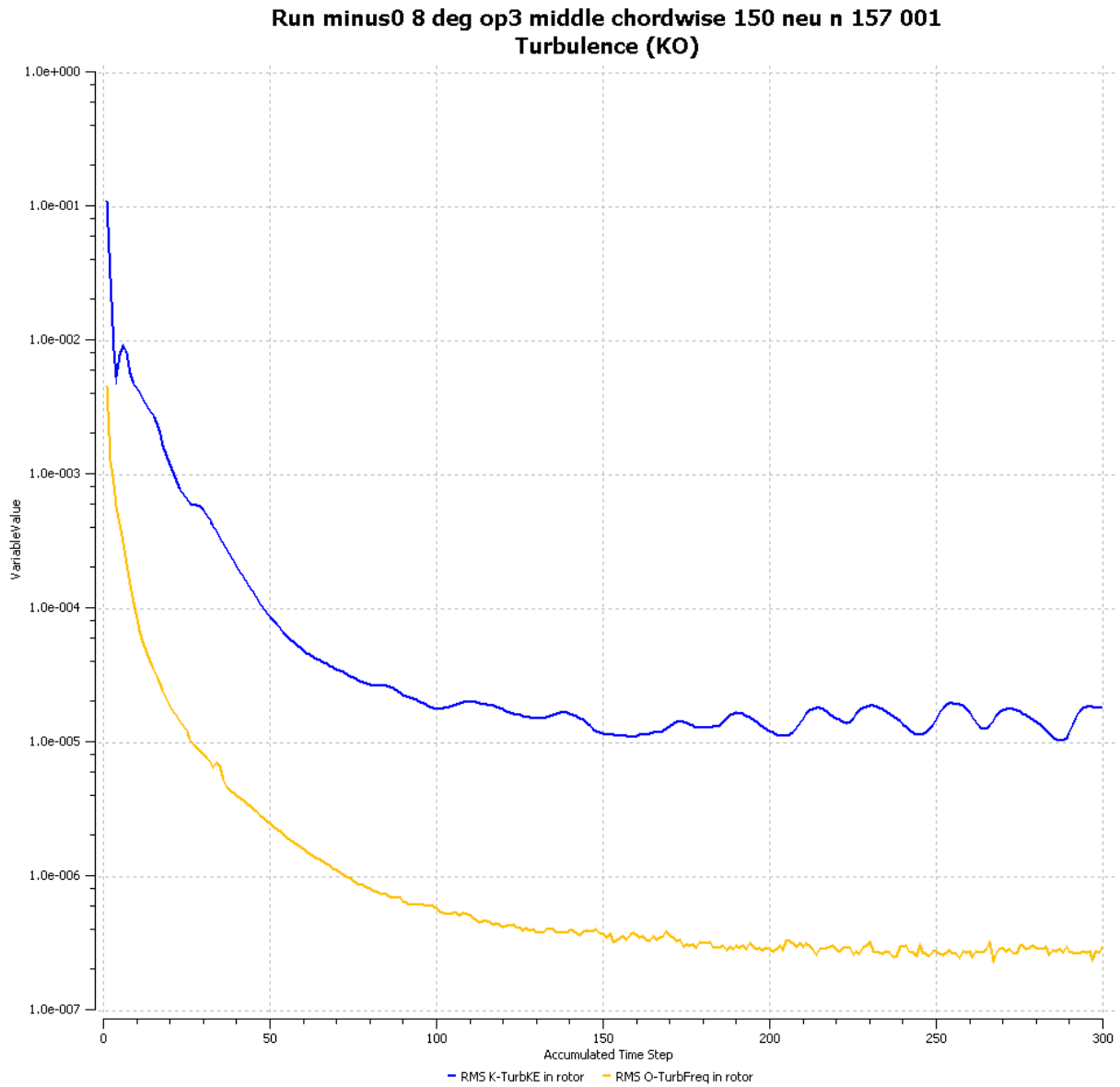


Figure 2: Convergence behavior of turbulence of the simulation with 150 nodes chordwise and $n = 15.7$ [rpm], see table 4.10 and chapter 4.3.3.2

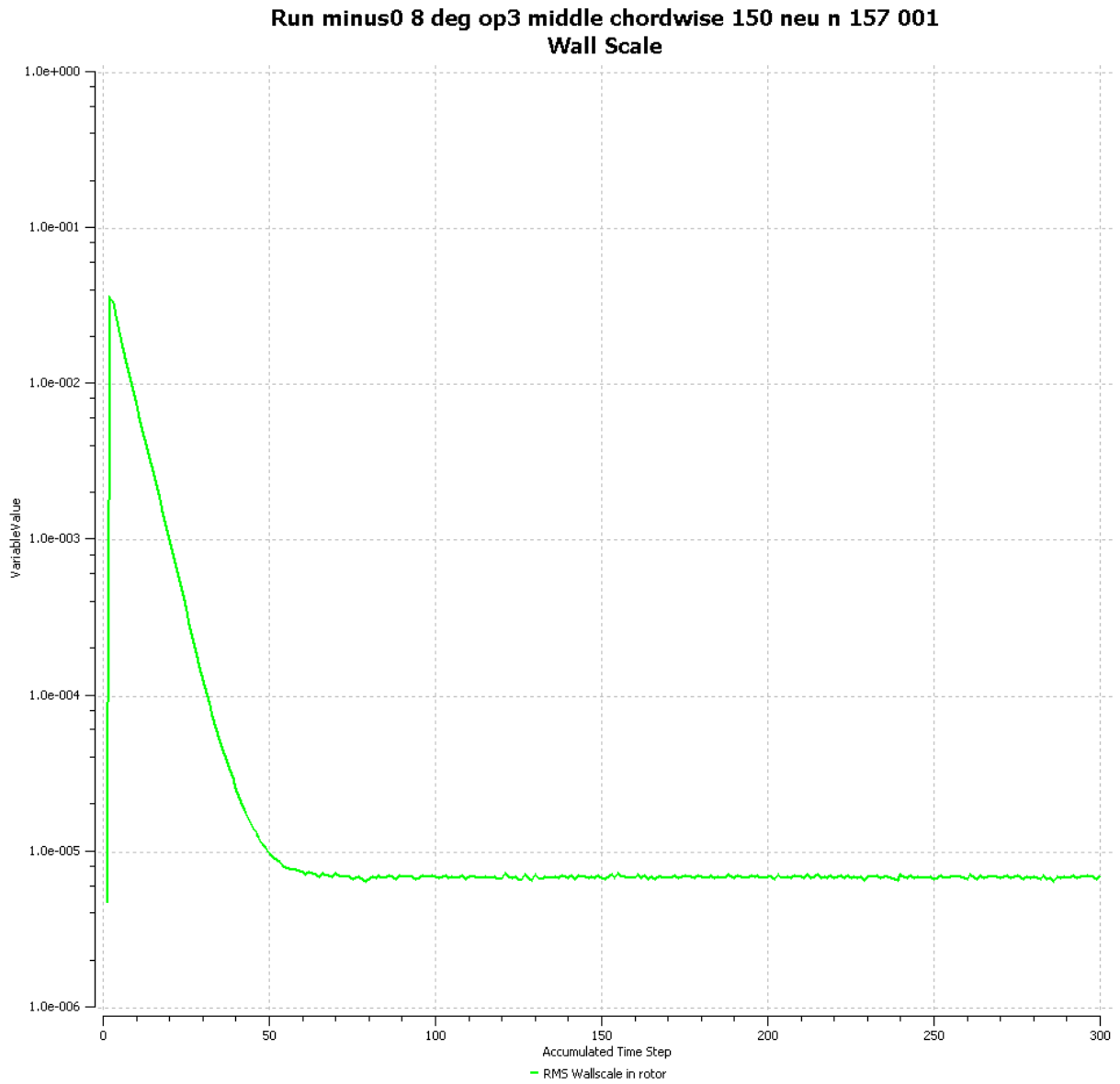


Figure 3: Convergence behavior of wall scale of the simulation with 150 nodes chordwise and $n = 15.7$ [rpm], see table 4.10 and chapter 4.3.3.2

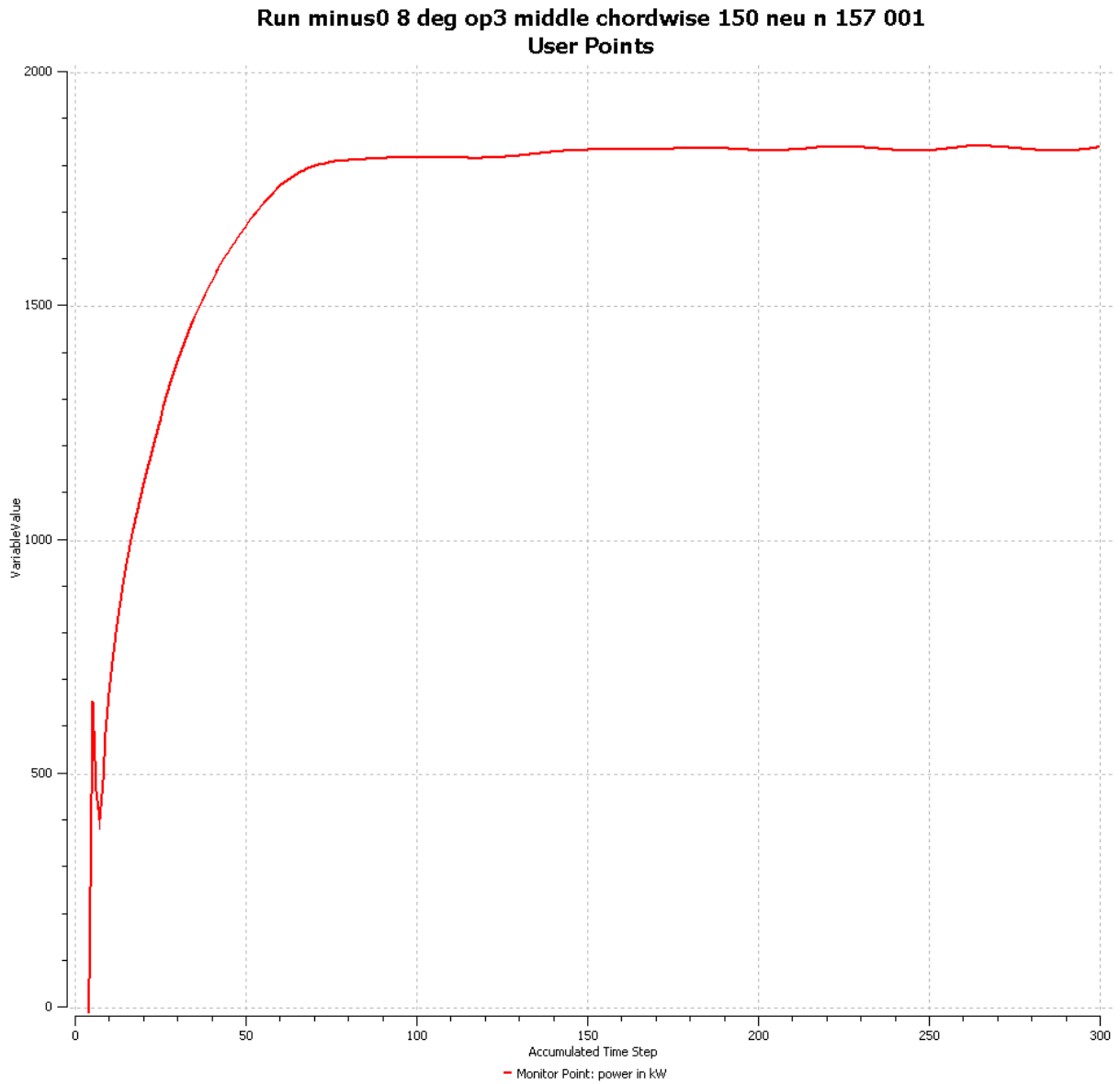


Figure 4: Convergence behavior of the user point power in kW of the simulation with 150 nodes chordwise and $n = 15.7$ [rpm], see table 4.10 and chapter 4.3.3.2